UNIVERSITAT
POLITÈCNICA
DE VALÈNCIA

Approximation of The Neutron Diffusion Equation on Hexagonal Geometries Using a h-p Finite Element Method

Author :
Ragab Fayez Moustafa

Supervisors :
Prof. Dr. Gumersindo Verdú Martín
Prof. Dr. Damián Ginestar Peiró

Valencia, April 2016

Acknowledgement

First and foremost, I would like to express my special appreciation and thanks to my supervisors, Dr. Gumersindo Verdú Martín and Dr. Damián Ginestar Peiró for the assistance, the encouragement , their time dedicated to this thesis, their technical guidance and moral support throughout my thesis, beside the opportunity of working in an interesting and useful research project.

I also wish to thank my colleagues at the department of Chemical and Nuclear Engineering and at the Institute for Multidisciplinary Mathematics in the Universitat Politécnica de Valéncia for making this constant work easier, thanks for creating a good atmosphere at the office, and for their moral support.

A special thanks to Dr. Rafael Miró Herrero and Dr. María Teresa Capilla Roma for their guidance and support during the thesis and for the time they spent for answering my questions about Parcs. Another big thanks goes to the financial support of Santiago Grisolía Scholarship.

I am grateful to my friend Antoni Vidal Ferrandiz for helping me out with the theory of my finite element formulation, for sharing his knowledge in deal.II library when I needed, for his crucial help, and of course for, his support during the three years we working side by side.

Last but not least, I would like to thank my friends and, in particular, my family for their continuous encouragement, deep trust, and love.

Ragab Fayez Moustafa
rafamou@upv.es

April 6, 2016

Summary

The neutron diffusion equation is an approximation of the neutron transport equation that describes the neutron population in a nuclear reactor core. In particular, we will consider here VVER-type reactors which use the neutron diffusion equation discretized on hexagonal meshes. Most of the simulation codes of a nuclear power reactor use the multigroup neutron diffusion equation to describe the neutron distribution inside the reactor core.To study the stationary state of a reactor, the reactor criticality is forced in artificial way leading to a generalized differential eigenvalue problem, known as the Lambda Modes equation, which is solved to obtain the dominant eigenvalues of the reactor and their corresponding eigenfunctions.

To discretize this model a finite element method with *h*-*p* adaptivity is used. This method allows to use heterogeneous meshes, and allows different refinements such as the use of *h*-adaptive meshes, reducing the size of specific cells, and *p*-refinement, increasing the polynomial degree of the basic functions used in the expansions of the solution in the different cells.

Once the solution for the steady state neutron distribution is obtained, it is used as initial condition for the time integration of the neutron diffusion equation. To simulate the behaviour of a nuclear power reactor it is necessary to be able to integrate the time-dependent neutron diffusion equation inside the reactor core. The spatial discretization of this equation is done using a finite element method that permits *h*-*p* refinements for different geometries. Transients involving the movement of the control rod banks have the problem known as the rod-cusping effect. Previous studies have usually approached the problem using a fixed mesh scheme defining averaged material properties and many techniques exist for the treatment of the rod cusping problem. The present work proposes the use of a moving mesh scheme that uses spatial meshes that change with the movement of the control rods avoiding the necessity of using equivalent material cross sections for the partially inserted cells. The performance of the moving mesh scheme is tested studying different benchmark problems.

For reactor calculations, the accuracy of a diffusion theory solution is limited for for complex fuel assemblies or fine mesh calculations. To improve these results a method that incorporates higher-order approximations for the angular dependence, as the simplified spherical harmonics (SP_N) method must be employed. In this work an *h-p* finite element method (FEM) is used to obtain the dominant Lambda mode associated with a configuration of a reactor core using the SP_N approximation. The performance of the SP_N (N= 1, 3, 5) approximations has been tested for different reactor benchmarks.

Resumen

La ecuación de la difusión neutrónica es una aproximación de la ecuación del transporte de neutrones que describe la población de neutrones en el núcleo de un reactor nuclear. En particular, consideraremos reactores de tipo VVER y para simular su comportamiento se utilizará la ecuación de la difusión neutrónica para cuya discretización se hace uso de mallas hexagonales.

La mayoría de los códigos de simulación de reactores nucleares utilizan aproximación multigrupo de energía de la ecuación de la difusión neutrónica para describir la distribución de neutrones en el interior del núcleo del reactor. Para estudiar el estado estacionario del reactor, es posible forzar la criticidad del reactor de forma artificial modificando las secciones eficaces de forma que se obtiene un problema de valores propios diferencial, conocido como el problema de los Modos Lambda, que se resuelve para obtener los valores propios dominantes del reactor y sus correspondientes funciones propias.

Para discretizar este modelo se ha hecho uso de un método de elementos finitos con adaptabilidad *h*-*p*. Este método permite el uso de mallas heterogéneas, y de diferentes refinamientos como el uso mallas *h*-adaptativas, reduciendo el tamaño de los distintos nodos, y el *p*-refinado, aumentando el grado del polinomio de las funciones básicas utilizado en los desarrollos de la solución en los diferentes nodos. Se ha desarrollado un código basado en un método de elementos finitos de alto orden para resolver el problema de los Modos Lambda en un reactor con geometría hexagonal y se han obtenido los modos dominantes para distintos problemas de referencia.

Una vez que se ha obtenido la solución para la distribución de neutrones en estado estacionario, ésta se utiliza como condición inicial para la integración de la ecuación de difusión neutrónica dependiente del tiempo. Para simular el comportamiento de un reactor nuclear para un determinado transitorio, es necesario ser capaz de integrar la ecuación de la difusión neutrónica dependiente del tiempo en el interior del núcleo del reactor. La discretización espacial de esta ecuación se hace usando un método de elementos finitos de alto orden que permite refinados de tipo *h*-*p* para distintas geometrías.

Los transitorios que implican el movimiento de los bancos de las barras de control tienen el problema conocido como el efecto ‘rod-cusping’. Estudios anteriores, por lo general, han abordado este problema utilizando una malla fija y definiendo propiedades promedio para los materiales correspondientes a las celdas donde se tiene la barra de control parcialmente insertada. En el presente trabajo se propone el uso de un esquema de malla móvil, de forma que en mallado espacial va cambiando con el movimiento de la barra de control, evitando la necesidad de utilizar secciones eficaces equivalentes para las celdas parcialmente insertadas. El funcionamiento de este esquema de malla móvil propuesto se estudia resolviendo distintos problemas tipo.

La precisión obtenida mediante de la teoría de la difusión en los cálculos de reactores es limitada cuando se tienen elementos de combustible complejos o se pretenden realizar cálculos en malla fina. Para mejorar estos resultados, es necesario disponer de un método que incorpore aproximaciones de orden superior de la ecuación del transporte de neutrones. Una posibilidad es hacer uso de las ecuaciones P_N simplificadas (SP_N). En este trabajo se utiliza un método de elementos finitos $h-p$ para obtener los modos dominantes asociados con una configuración dada del núcleo de un reactor nuclear con geometría hexagonal usando la aproximación SP_N. El funcionamiento de las aproximaciones SP_N $(N = 1, 3, 5)$ se ha estudiado para distintos problemas de referencia.

Resum

L'equació de la difusió neutrònica és una aproximació de l'equació del transport de neutrons que descriu la població de neutrons en el nucli de un reactor nuclear. En particular, considerarem reactors de tipus VVER i per a simular el seu comportament s'utilitzarà l'equació de la difusió neutrónica que es discretitza fent ús de malles hexagonals.

La majoria dels codis de simulació de reactors nuclears utilitzen l'aproximació multigrup d'energia de l'equació de la difusió neutrónica per a descriure la distribució de neutrons a l'interior del nucli del reactor. Per a estudiar l'estat estacionari del reactor, és possible forÃ§ar la seua criticitat de forma artificial modificant les seccions eficaces de manera que s'obté un problema de valors propis diferencial, conegut com el problema dels Modes Lambda, que es resol per a obtenir els valors propis dominants del reactor i les seues corresponents funcions pròpies.

Per a discretitzar aquest model s'ha fet ús d'un mètode d'elements finits amb adaptabilitat *h-p*. Aquest mètode permet l'ús de malles heterogènies, i de diferents refinaments com l'ús malles *h*-adaptatives, reduint la grandària dels diferents nodes, i el *p*-refinat, augmentant el grau del polinomi de les funcions bàsiques utilitzat en els desenvolupaments de la solució en els diferents nodes. S'ha desenvolupat un codi basat en un mètode d'elements finits d'alt ordre per a resoldre el problema dels Modes Lambda en un reactor amb geometria hexagonal i s'han obtingut els modes dominants per a diferents problemes de referència.

Una vegada que s'ha obtingut la solució per a la distribució de neutrons en estat estacionari, aquesta s'utilitza com a condició inicial per a la integració de l'equació de difusió neutrònica depenent del temps. Per a simular el comportament d'un reactor nuclear per a un determinat transitori, és necessari ser capaÃ§ d'integrar l'equació de la difusió neutrónica depenent del temps a l'interior del nucli del reactor. La discretitzación espacial d'aquesta equació es fa usant un mètode d'elements finits d'alt ordre que permet refinats de tipus *h-p* per a diferents geometries.

Els transitoris que impliquen el moviment dels bancs de les barres de control tenen el problema conegut com l'efecte 'rod-cusping'. Estudis anteriors, en general, han

abordat aquest problema utilitzant una malla fixa i definint propietats equivalents per als materials corresponents a les celÂ·les on es té la barra de control parcialment inserida. En el present treball es proposa l'ús d'un esquema de malla mòbil, de manera que en mallat espacial va canviant amb el moviment de la barra de control, evitant la necessitat d'utilitzar seccions eficaces equivalents per a les celÂ·les parcialment inserides. El funcionament de aquest esquema de malla mòbil s'estudia resolent diferents problemes tipus.

La precisió obtinguda mitjanÃ§ant de la teoria de la difusió en els càlculs de reactors és limitada quan es tenen elements de combustible complexos o es pretenen realitzar càlculs en malla fina. Per a millorar aquests resultats, és necessari disposar d'un mètode que incorpore aproximacions d'ordre superior de l'equació del transport de neutrons. Una possibilitat és fer ús de les equacions P_N simplificades (SP_N). En aquest treball s'utilitza un mètode d'elements finits $h-p$ per a obtenir els modes dominants associats amb una configuració donada del nucli de un reactor amb geometria hexagonal usant l'aproximació SP_N. El funcionament de les aproximacions SP_N $(N = 1, 3, 5)$ s'ha estudiat per a diferents problemes de referència.

Contents

List of Figures

List of Tables

Chapter 1

Introduction

The nuclear industry life cycle is not very different from other kind of industry, being some of its distinguishing characteristics, its long time horizons, its technical complexity and the necessity of excellence. The nuclear sector has evolved quickly, but this would not has been possible without high quality research and support programmes to promote knowledge generation and technically competent staff for the safely plant operation.

In nuclear reactor core physics two main objects to study can be distinguished. On one hand, the localisation and dynamics (or behaviour) of neutrons and on the other hand, the criticality of the reactor, i.e., whether it is possible to maintain the chain reaction in its interior. Among the many different methods that exist to answer these questions, the most commonly used ones are based on the neutron diffusion theory, which is an approximation to the neutron transport theory.

The behaviour of a nuclear reactor is governed by the transport of neutrons and the interactions between neutrons and matter.Therefore, the design, analysis and control of nuclear reactors requires solving numerically the neutron transport equation (or an approximation of it) in order to determine the neutron distribution in the reactor and hence, validate and verify design and safety parameters.

The rigorous treatment of this problem is completely analogous to that used in classic studies of gaseous diffusion [1]. The method of study consists of taking a control volume at some point of the reactor and deriving expressions that account for the different ways of entry and exit from this control volume of neutrons, having a given velocity vector by introducing effective cross sections, avoiding to consider specific interactions of neutrons within the control volume. The balance between the proportion of neutrons which enter and the proportion of neutrons which exit the control volume, gives rise to what is known as the Boltzmann transport equation. To simplify this equation, some hypothesis are introduced such as that all the neutrons can be grouped into energy ranges (groups) and that the distribution of the neutron velocity vectors is independent of the direction. Under these conditions, one can obtain the neutron diffusion equation as an approximation of the transport equation.

There are mainly two types of calculations associated with the neutron diffusion. A first type of static calculations involving the determination of the Lambda Modes associated with a given configuration of the reactor in a given time. This is a generalized eigenvalue problem associated with a differential operator with given boundary conditions. The determination of the fundamental mode allows us to describe the behaviour of the reactor in steady state. Another type of calculations are those made for the determination of a transient from a perturbation made on a stationary configuration of the reactor, using for that the time dependent neutron diffusion equation.

Several algorithms to integrate the neutron diffusion equation in hexagonal geometries have been developed, both for the Lambda Modes problem [2] beginning to study the problem of updating the lambda Modes for close configurations of the reactor [3]. Also, the time dependent neutron diffusion equation has been studied for this kind of reactors [4] using homogeneous meshes. Mesh adaptivity begun in the late 1970's [5] and is based on the idea that in order to achieve high accuracy, a uniformly fine mesh is not necessarily required; rather, the computational grid only needs to be fine in regions where the solution is rough and can be coarse in areas where the solution is smooth and, therefore, well resolved even on large cells. The challenge is that, in general, it is not known a priori where the solution will require the mesh to be fine. Consequently, the computation of local error or smoothness indicators from a numerical solution, previously obtained on a coarser mesh, lies at the heart of all adaptive mesh refinement algorithms and a significant number of successful approaches have been developed for this problem in the last decade [6], [7]. Using these methods, it has been shown for many problems that the computational effort needed to reach a certain accuracy can often be reduced by one or several orders of magnitude compared to uniform meshes, frequently enabling the solution of entire new classes of problems that were previously considered too expensive computationally to be solved with the required accuracy. The use of adaptive meshes for the study of nuclear reactors has been recently proposed [8], [9], beginning with the study of different error estimators for the mesh refinement for the computation of the k-effective of the reactor and the stationary power distribution.

1.1 Objective of the thesis

The main objective of the present thesis is the development and verification of a 3D neutronic code for nuclear reactors with hexagonal geometry to be able to learn about the behaviour of nuclear power reactors and to carry out safety studies in the most common transients and reactivity accidents. The objectives can be listed as :

- Implementation of an adaptive *h-p* finite element method to compute the dominant Lambda Modes associated with a configuration of a reactor core, the reactor power distribution and the subcritical modes.
- Implementation of a finite element method for the time dependent neutron diffusion equation inside the reactor core to be able to analysis a transient and simulate the behaviour of the nuclear power reactor.
- Implementation of a new technique for the treatment of the rod cusping problem in the 3D transients calculations using the open source finite elements library deal.II, developing a moving mesh strategy that move the mesh with the movement of the control rod avoiding the problem of the partially rodded nodes homogenization.
- Implementation of an adaptive *h-p* finite element method for the other approaches of the neutron transport equation solutions, taking into account different angular discretizations as SP_N equations and compare the obtained results with the diffusion results.

1.2 Thesis outline

The following sections serve as an overview of the finite element method (FEM) and introduction to the neutron transport equation and its solution approaches describing the P_N and SP_N Equations, the Lambda Modes equations, the VVER reactors and illustrating the capabilities of the deal.II finite element library, the PETSC library, the SLEPc library and Gmsh package, respectively.

In Chapter 2, an introduction to the finite element method (FEM) is given. Different solution approaches for the static solution of the neutron transport equation are briefly described. A particular focus, however, is put on the adaptive *h-p* finite element method and its numerical calculation.

In Chapter 3, a finite element method is introduced for the time dependent neutron diffusion equation inside the reactor core. A treatment of the rod cusping problem in the 3D calculations with control rods using the open source finite elements library deal.II has been presented.

Chapter 4 of this thesis is concerned with the high order finite element method for the simplified spherical harmonics equations. A particular focus, however, is put on the simplified P_N (or SP_N) transport method, which provides a basis for SP_3, SP_5 and the diffusion approaches. A numerical analysis of the performance of the SP_N transport and diffusion methods developed in the previous chapters is demonstrated with particular regard to mesh refinement analyses. Several hexagonal benchmark and test problems with different material compositions are studied.

In Chapter 5, The final chapter summarizes the whole work.

1.3 Finite element method

In the earlier days of nuclear engineering, the process of solving the neutron distribution in a nuclear reactor core was split into four sub-tasks (in a divide and conquer fashion)[10] : first, a small 2D geometrical motif of the core was solved with high fidelity, requiring the solution of the neutron transport equation; then the results of the previous stage were used to homogenize the geometry and material compositions; subsequently, the homogenized data are solved on 3D coarse meshes using the diffusion approximation of transport; finally, the coarse 3D results along with the 2D fine results are used to reconstruct the fine 3D results. This methodology is still prevalent nowadays but possesses inherent drawbacks found in its homogenization and reconstruction processes. It is commonly acknowledged [11] that overcoming these drawbacks will require solving the multi-group transport equation on the whole heterogeneous 3D geometry, with a large number of energy groups and angular directions or moments. A 3D solution will certainly not be feasible without improved algorithms such as automatic mesh adaptation, where the mesh cells are automatically and selectively refined in order to reduce the largest contributions to the total error. Even though the ultimate goal is the efficient resolution of the transport equation in 3D, there are some necessary issues which need to be resolved but can be understood and analyzed on a reduced scale. In this thesis, we investigate the behaviour of mesh refinement techniques in the case of eigenproblems consisting of systems of coupled equations (the multi-group equations).

Historically, solutions to reactor core analysis problems were first obtained using traditional finite difference methods (FDM)[12] , [13] in the 1960's. FDM requires a large number of mesh points in order to represent accurately the spatial variation of the neutron flux. It is well-known that the finite difference mesh spacing must be on the order of the smallest group-wise diffusion length for correct results. The computational cost associated with FDM motivated the development of modern transverse-integrated nodal methods [14]. These nodal methods reached maturity in the mid 1980's and are widely used for reactor physics design and on-site monitoring. Nowadays, 3D calculations for light water reactors with homogenized fuel assemblies can now be performed even in on-site fashion. However, the accuracy and the theoretical justification for the homogenization and reconstruction processes, which enabled the use of FDM and nodal methods, now hinders any further improvements to 3D solutions using these techniques. It is even believed that the success of modern nodal methods prohibited the further development of other spatial discretization techniques in reactor core analysis. However, with the emergence of new types of reactors with more intricate geometries or more severe flux transients, the motivation to pursue more accurate numerical simulations is calling for finer geometrical details, increased number of energy groups and more angles or moments in the transport equation. The finite element method (FEM) since as early as the mid 70's, [15], [16], [17] , which had been introduced in nuclear engineering and gradually obtained more attention [18], [19], is of special interest to us because it provides an efficient way to refine the mesh non-uniformly while delivering accurate solutions.

The FEM is a computational technique for obtaining approximate solutions to the partial differential equations that arise in scientific and engineering applications. Rather than approximating the partial differential equations directly as, for instance, with finite difference method, the finite element method utilizes a variational problem that involves an integral of the differential equation over the problem domain. This domain can contain complex geometries (and boundaries). FEM can easily handle such domains whereas FDM is restricted to handle only regular shapes and simple alterations of them. In FEM, the computational domain is divided into a number of sub-domains called finite elements and the solution of the partial differential equation is approximated by a polynomial function on each element. The division of the domain can be arbitrary. The polynomial orders within each element can be of any value. Hence, FEM provides two options for refining a mesh non-uniformly. However, optimally distributing these approximation parameters - the sizes h of the elements and the orders p of the polynomial shape functions- represents a significant departure from the conventional finite element techniques. Such$h$-p-refinements emerged in late 1980's and required the resolution of several formidable problems for an effective implementation [20], [21], [22] : new data structures, efficient linear solvers, effective local (a posteriori) error estimations. Note that in the recent years, h-refinement and p-refinement have been investigated for neutronics calculations [23], [24].

1.4 Neutron diffusion equation

The behaviour of a nuclear reactor is modelled by means of the neutron distribution in the reactor core as a function depending on the position, the velocity, the energy and the time. Thus, one of the main problems for the nuclear reactor theory is to predict this distribution. It can be done solving the neutron transport equation over the reactor domain. But, due to the complexity of this equation, the neutron diffusion equation is widely used as an approximation [25]. We will proceed to show the process followed to deduce the neutron diffusion equation as an approximation for the transport equation [26].

Within the transport theory the neutron is considered as a classical particle, in the sense that it can be fully determined by means of knowing its position and its velocity. The interaction between neutrons and atomic nuclei is dealt from a macroscopic point of view, avoiding the details of the interaction process inside the core. Moreover, the cross sections associated to the probability of a determined type of reaction is defined and it is supposed that this interaction is produced instantly.

The balance equation in a differential control volume is obtained taking into account that the rate of change for the density respect to the time inside the volume $dVdEd\vec{\Omega}$ of the phase space is given by the difference between the neutron rate flow into and out of that control volume. To describe the neutron population the magnitude denoted as neutron angular density, $N(\vec{r}, E, \vec{\Omega}, t)$, is used, defined as the probable (or expected) number of neutrons at position $\vec{r}$ with direction $\vec{\Omega}$ and energy E, at time t, per unit volume and per unit solid angle per unit energy. Moreover,the neutron angular flux is defined as

$$\Psi(\vec{r}, E, \vec{\Omega}, t) \equiv vN(\vec{r}, E, \vec{\Omega}, t), \tag{1.1}$$

where v is the neutron speed, and the balance equation inside the control volume which describes the *neutron transport equation* is expressed as follows [25],

$$\begin{aligned}
\frac{1}{v}\frac{\partial \Psi}{\partial t}(\vec{r}, E, \vec{\Omega}, t) = & -\vec{\Omega}.\vec{\nabla}\Psi(\vec{r}, E, \vec{\Omega}, t) - \Sigma_T(\vec{r}, E, t)\Psi(\vec{r}, E, \vec{\Omega}, t) + Q(\vec{r}, E, \vec{\Omega}, t) \\
& + (1-\beta\ )\frac{\chi_p(E)}{4\pi}\int_0^\infty dE'\nu\Sigma_f(\vec{r}, E', t)\int_{\vec{\Omega}'} d\vec{\Omega}'\ \Psi(\vec{r}, E', \vec{\Omega}', t) \\
& + \int_0^\infty dE' \int_{\vec{\Omega}'} d\vec{\Omega}'\ \Sigma_s(\vec{r}, E', \vec{\Omega}' \to E, \vec{\Omega}, t)\ \Psi(\vec{r}, E', \vec{\Omega}', t) \\
& + \sum_{k=1}^{K} \lambda_k \frac{\chi_k(E)}{4\pi}\ \mathcal{C}_k(\vec{r}, t).
\end{aligned} \tag{1.2}$$

The first term on the right hand of the equation, $\vec{\Omega}.\vec{\nabla}\Psi(\vec{r}, E, \vec{\Omega}, t)$, takes into account the neutron advection flowing out the control volume, where $\vec{\Omega}$ is the unit vector denoting the direction of the going neutrons.

The second term, $\Sigma_T(\vec{r}, E, t)\ \Psi(\vec{r}, E, \vec{\Omega}, t)$, describes the rate at which neutrons flow out the control volume by means of scattering and absorption processes. $Q(\vec{r}, E, \vec{\Omega}, t)$ denotes a possible external source of neutrons. The fourth term indicates the neutrons introduced into the volume element by fission processes, assuming isotropic fission distribution. The fifth term describes the neutrons introduced into the volume element by scattering. The *delayed neutrons* appearing in the volume from the precursor's decay is taken into account by means of the last term.

Σ_T and Σ_f denote the *total cross section* and *the fission cross section* respectively. χ_p indicates the spectrum of the neutron produced by fission and χ_k is the spectrum of neutrons produced by the precursors decay. The probability for a neutron to be scattered from a volume $dVdE'd\vec{\Omega}'$ to other $dVdEd\vec{\Omega}$, is represented by $\Sigma_s(\vec{r}, E', \vec{\Omega}' \to E, \vec{\Omega}, t)$. The fission neutron rate scattered due to the transformation of a precursor of type k is β_k , where $\beta = \sum_{k=1}^{K} \beta_k$ and K is the number of neutron precursors considered. The decay rate for which a precursor of type k decays is $\lambda_k \mathcal{C}_k$.

The concentration of delayed neutron precursors satisfies the following balance equation

$$\frac{\partial \mathcal{C}_k}{\partial t}(\vec{r}, t) = \beta_k \int_0^\infty dE \int_{\vec{\Omega}} d\vec{\Omega}\ \nu\Sigma_f(\vec{r}, E, t)\ \Psi(\vec{r}, E, \vec{\Omega}, t) - \lambda_k \mathcal{C}_k(\vec{r}, t), \tag{1.3}$$

where ν is the average number of neutrons arising in one fission, and $k = 1, ..., K$. It is assumed that the angular dependency for the neutron scattering is mainly due to the angle between the direction of the incident neutron, $\vec{\Omega}'$, and the direction of the emerging neutron, $\vec{\Omega}$. It is defined

$$\begin{aligned} \vec{\Omega} &= (\Omega_1, \Omega_2, \Omega_3) = (\sin\theta\cos\varphi, \sin\theta\sin\varphi, \cos\theta), \\ \vec{\Omega}' &= (\Omega_1', \Omega_2', \Omega_3') = (\sin\theta'\cos\varphi', \sin\theta'\sin\varphi', \cos\theta'), \\ \mu^* &= \vec{\Omega}'.\vec{\Omega} = \cos\ \theta^*, \qquad \mu = \cos\ \theta, \qquad \mu' = cos\ \theta' \end{aligned} \tag{1.4}$$

where θ and θ' are the angles of directions $\vec{\Omega}$ and $\vec{\Omega}'$, respectively, with the z axis of the chosen reference system (see Figure 1.1).

The spherical harmonics method to approximate the neutron transport equation consists of expanding the angular neutron flux, $\Psi(\vec{r}, E, \vec{\Omega}, t)$, and the external neutron source, $Q(\vec{r}, E, \vec{\Omega}, t)$, as follows

$$\Psi(\vec{r}, E, \vec{\Omega}, t) = \sum_{t=0}^{\infty} \sum_{m=-1}^{+1} \Phi_l^m(\vec{r}, E, t) Y_l^m(\vec{\Omega}), \tag{1.5}$$

$$Q(\vec{r}, E, \vec{\Omega}, t) = \sum_{t=0}^{\infty} \sum_{m=-1}^{+1} Q_l^m(\vec{r}, E, t) Y_l^m(\vec{\Omega}), \tag{1.6}$$

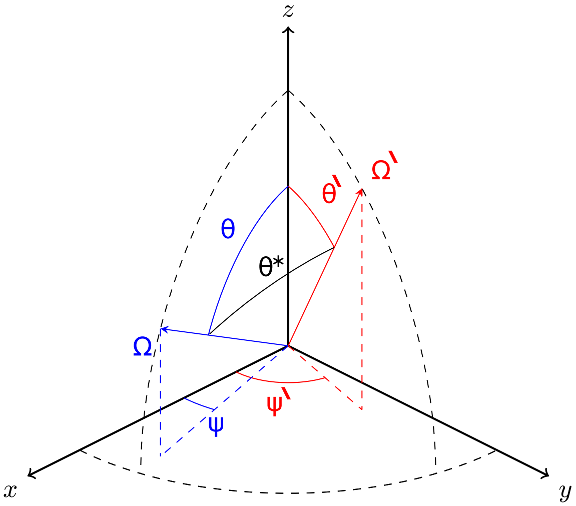

Figure 1.1: Magnitudes for the Addition theorem for the Legendre polynomials.

where $Y_l^m(\vec{\Omega})$ are the (normalized) spherical harmonics defined as

$$Y_l^m(\theta,\varphi) \equiv H_l^m P_l^m(\cos\theta) e^{im\varphi}, \tag{1.7}$$

where

$$H_l^m = \sqrt{\frac{2l+1}{4\pi}\frac{(l-m)!}{(l+m)!}}. \tag{1.8}$$

It is assumed that scattering only depends on the relative angle, $\mu* = \vec{\Omega}.\vec{\Omega'}$, and that the scattering cross section can be expanded as the following Legendre polynomials series:

$$\Sigma_s(\vec{r}, E', \vec{\Omega'} \rightarrow E, \vec{\Omega}, t) = \sum_{t=0}^{\infty} \frac{2l+1}{4\pi} \Sigma_{sl}(\vec{r}, E' \rightarrow E, t) P_l(\mu*), \tag{1.9}$$

$$P_l(\mu*) = P_l(\mu)P_l(\mu') + 2\sum_{m=1}^{l} \frac{(l-m)!}{(l+m)!} P_l^m P_l^{m'} \cos m(\varphi - \varphi') \tag{1.10}$$

where P_l are the Legendre polynomials. Making use of the addition theorem for the Legendre polynomials (equation 1.10), it can be written

$$\begin{aligned}
&\sum_{t=0}^{\infty} \frac{2l+1}{4\pi}\ \Sigma_{sl}(\vec{r}, E' \rightarrow E, t) P_l(\mu *) = \sum_{t=0}^{\infty} \frac{2l+1}{4\pi}\ \Sigma_{sl}(\vec{r}, E' \rightarrow E, t) \Bigg(P_l(\mu) P_l(\mu') \\
&+ 2\sum_{m=1}^{l} \frac{(l-m)!}{(l+m)!} P_l^m(\mu) P_l^m(\mu') \cos m(\varphi - \varphi') \Bigg) = \sum_{t=0}^{\infty} \frac{2l+1}{4\pi}\ \Sigma_{sl}(\vec{r}, E' \rightarrow E, t) \\
&\times \left(P_l(\mu) P_l(\mu') + 2\sum_{m=1}^{l} \frac{(l-m)!}{(l+m)!} P_l^m(\mu) P_l^m(\mu') \left(\frac{e^{im\varphi} e^{-im\varphi'} + e^{-im\varphi} e^{+im\varphi'}}{2} \right) \right) \\
&= \sum_{t=0}^{\infty} \frac{2l+1}{4\pi} \Sigma_{sl}(\vec{r}, E' \rightarrow E, t) \left(\frac{4\pi}{2l+1} Y_l^0(\vec{\Omega}) Y_l^0(\vec{\Omega}') \right. \\
&+ \sum_{m=1}^{l} \frac{(l-m)!}{(l+m)!} P_l^m(\mu) P_l^m(\mu') e^{im\varphi} e^{-im\varphi'} \\
&\left. + \sum_{m=1}^{l} \frac{(l-m)!}{(l+m)!} \frac{(l+m)!}{(l-m)!} \frac{(l+m)!}{(l-m)!} P_l^{-m}(\mu) P_l^{-m}(\mu') e^{-im\varphi} e^{+im\varphi'} \right) \\
&\sum_{t=0}^{\infty} \sum_{m=-l}^{+l} \Sigma_{sl}(\vec{r}, E' \rightarrow E, t) Y_l^m(\vec{\Omega}) Y_l^{m*}(\vec{\Omega}'), \qquad (1.11)
\end{aligned}$$

finally obtaining the equality,

$$\Sigma_s(\vec{r}, E', \vec{\Omega}' \rightarrow E, \vec{\Omega}, t) = \sum_{t=0}^{\infty} \sum_{m=-l}^{+l} \Sigma_{sl}(\vec{r}, E' \rightarrow E, t) Y_l^m(\vec{\Omega}) Y_l^{m*}(\vec{\Omega}'). \qquad (1.12)$$

It will be assumed the external neutron source to be isotropic, i.e., Q_e^m but for Q_0^0. Due to this assumption equation (1.6) becomes.

$$Q(\vec{r}, E, \vec{\Omega}, t) = Q_0^0(\vec{r}, E, t) Y_0^0(\vec{\Omega}), \qquad (1.13)$$

For the P_L approximation, previous series are truncated for a given value $l = L$, taking into account that when $L \rightarrow \infty$ we recover the exact solution.

Now the identities (1.5),(1.12) and (1.13) are substituted into equation (1.2), obtaining

$$
\begin{aligned}
&\sum_{l=0}^{L}\sum_{m=-l}^{+l} Y_l^m(\vec{\Omega})\bigg(\frac{1}{\upsilon}\frac{\partial \Phi_l^m}{\partial t}(\vec{r},E,t) + \vec{\Omega}.\vec{\nabla}\Phi_l^m(\vec{r},E,t) + \Sigma_T(\vec{r},E,t)\Phi_l^m(\vec{r},E,t) \\
&-\int_0^{\infty} \Sigma_{sl}(\vec{r},E' \rightarrow E,t)\sum_{\alpha=0}^{\infty}\sum_{\gamma=-\alpha}^{+\alpha}\int_{\vec{\Omega}'} Y_\alpha^\gamma(\vec{\Omega}')Y_l^{m*}(\vec{\Omega}')d\Omega'\Phi_\alpha^\gamma(\vec{r},E',t)dE'\bigg) \\
&-(1-\beta\ )\frac{\chi_p(E)}{4\pi}\int_0^{\infty}\nu\Sigma_f(\vec{r},E,t)\sum_{l=0}^{L}\sum_{m=-l}^{+l}\Phi_l^m(\vec{r},E,t)\int_{\vec{\Omega}'} Y_l^m(\vec{\Omega}')d\Omega' dE' \\
&-Q_0^0(\vec{r},E,t)Y_0^0(\vec{\Omega}) - \sum_{k=1}^{K}\lambda_k\frac{\chi_k(E)}{4\pi}\mathcal{C}_k(\vec{r},t) = 0.
\end{aligned}
\tag{1.14}
$$

Then integrals with respect to $\vec{\Omega}'$ are solved using the orthogonality properties of the spherical harmonics

$$
\int_{\varphi=o}^{2\pi}\int_{\theta=o}^{\pi} Y_{l_1}^{m_1*}(\theta,\varphi)Y_{l_2}^{m_2}(\theta,\varphi)\sin\theta\ d\theta\ d\varphi = \delta_{l_1}^{l_2}\ \delta_{m_1}^{m_2}. \tag{1.15}
$$

Obtaining

$$
\begin{aligned}
&\sum_{\alpha=0}^{\infty}\sum_{\gamma=\alpha}^{+\alpha}\left(\int_{\Omega'} Y_\alpha^\gamma(\vec{\Omega}')Y_l^{m*}(\vec{\Omega}')d\Omega'\right)\Phi_\alpha^\gamma(\vec{r},E',t) \\
&\sum_{\alpha=0}^{\infty}\sum_{\gamma=\alpha}^{+\alpha}\delta_\gamma^m\delta_\alpha^l\Phi_\alpha^\gamma(\vec{r},E',t) = \Phi_l^m(\vec{r},E',t),
\end{aligned}
\tag{1.16}
$$

$$
\sum_{l=0}^{\infty}\sum_{m=-l}^{+l}\int_{\Omega'} Y_l^m(\vec{\Omega}')d\Omega'\Phi_l^m(\vec{r},E',t) = \frac{\Phi_0^0(\vec{r},E',t)}{H_0^0}, \tag{1.17}
$$

where H_l^m is defined at equation (1.8), and substituting equation (1.16) and (1.17) into the equation (1.14), it is obtained

$$\sum_{l=0}^{L}\sum_{m=-l}^{+l} Y_l^m(\vec{\Omega})\Big(\frac{1}{\upsilon}\frac{\partial \Phi_l^m}{\partial t}(\vec{r},E,t)+\vec{\Omega}.\vec{\nabla}\Phi_l^m(\vec{r},E,t)$$
$$+\Sigma_T(\vec{r},E,t)\Phi_l^m(\vec{r},E,t)-\int_0^\infty dE'\Sigma_{sl}(\vec{r},E'\to E,t)\Phi_l^m(\vec{r},E',t)\Big)$$
$$-(1-\beta\,)\frac{\chi_p(E)}{4\pi}\int_0^\infty dE'\nu\Sigma_f(\vec{r},E',t)\frac{\Phi_0^0(\vec{r},E',t)}{H_0^0}$$
$$-Q_0^0(\vec{r},E,t)Y_0^0(\vec{\Omega})-\sum_{k=1}^{K}\lambda_k\frac{\chi_k(E)}{4\pi}\,\mathcal{C}_k(\vec{r},t)=0. \tag{1.18}$$

Now the objective is to decouple the equation (1.18) into a system of partial differential equations, weighted by a set of spherical harmonics. First, the operator $\vec{\Omega}.\vec{\nabla}$ is rewritten by means of the expression

$$\begin{aligned}Y_l^m(\vec{\Omega})(\vec{\Omega}.\vec{\nabla}) =& \left(A_1^{l,m}\;Y_{l+1}^{m+1}\;(\vec{\Omega})-A_2^{l,m}\;Y_{l-1}^{m+1}\;(\vec{\Omega})\right)\left(\frac{\partial}{\partial x}-i\frac{\partial}{\partial y}\right)\\ &+\left(-A_3^{l,m}\;Y_{l+1}^{m-1}\;(\vec{\Omega})+A_4^{l,m}\;Y_{l-1}^{m-1}\;(\vec{\Omega})\right)\left(\frac{\partial}{\partial x}+i\frac{\partial}{\partial y}\right)\\ &+\left(-A_5^{l,m}\;Y_{l-1}^{m}\;(\vec{\Omega})+A_6^{l,m}\;Y_{l+1}^{m}\;(\vec{\Omega})\right)\frac{\partial}{\partial z}\;\cdot\,,\end{aligned} \tag{1.19}$$

Thus, equations will be decoupled substituting at (1.18), multiplying by $Y_\alpha^{\gamma *}(\vec{\Omega})$ and integrating for all direction, making use of the orthogonality property for the spherical harmonics (equation 1.15), it is obtained

$$\begin{aligned}\frac{1}{\upsilon}\frac{\partial \Phi_\alpha^\gamma}{\partial t}(\vec{r},E,t)&+\left(\frac{\partial}{\partial x}-i\frac{\partial}{\partial y}\right)\left(A_1^{\alpha-1,\gamma-1}\;\Phi_{\alpha-1}^{\gamma-1}(\vec{r},E,t)-A_2^{\alpha+1,\gamma-1}\;\Phi_{\alpha+1}^{\gamma-1}(\vec{r},E,t)\right)\\ &+\left(\frac{\partial}{\partial x}-i\frac{\partial}{\partial y}\right)\left(A_3^{\alpha-1,\gamma+1}\;\Phi_{\alpha-1}^{\gamma+1}(\vec{r},E,t)+A_4^{\alpha+1,\gamma+1}\;\Phi_{\alpha+1}^{\gamma+1}(\vec{r},E,t)\right)\\ &+\frac{\partial}{\partial z}\left(A_5^{\alpha+1,\gamma}\;\Phi_{\alpha+1}^{\gamma}(\vec{r},E,t)+A_6^{\alpha-1,\gamma}\;\Phi_{\alpha-1}^{\gamma}(\vec{r},E,t)\right)\\ &-\Sigma_T(\vec{r},E,t)\;\Phi_\alpha^\gamma(\vec{r},E,t)-\int_0^\infty dE'\;\Sigma_{sl}(\vec{r},E'\to E,t)\;\Phi_\alpha^\gamma(\vec{r},E',t)\\ &-(1-\beta\,)\frac{\chi_p(E)}{4\pi}\int_0^\infty dE'\;\nu\Sigma_f(\vec{r},E',t)\;\frac{\Phi_0^0(\vec{r},E',t)}{H_0^0}\;H_0^0\;\delta_0^\alpha\;\delta_0^\gamma\\ &-\frac{Q_0^0(\vec{r},E,t)}{H_0^0}H_0^0\;\delta_0^\alpha\;\delta_0^\gamma-\sum_{k=1}^{K}\lambda_k\frac{\chi_k(E)}{4\pi}\mathcal{C}_k(\vec{r},t)\;H_0^0\;\delta_0^\alpha\;\delta_0^\gamma=0,\\ &\alpha=0,1,....,L,\qquad \gamma=-\alpha,....,\alpha.\;,\end{aligned} \tag{1.20}$$

where constants $A_n^{l,m}$, $n = 1, ..., 6$ are defined as

$$\begin{aligned}
A_1^{l,m} &= \frac{1}{2}\left(\frac{(l+m+2)(l+m+1)}{(2l+3)(2l+1)}\right)^{\frac{1}{2}}, \\
A_2^{l,m} &= \frac{1}{2}\left(\frac{(l-m)(l-m-1)}{(2l+1)(2l-1)}\right)^{\frac{1}{2}}, \\
A_3^{l,m} &= \frac{1}{2}\left(\frac{(l-m+2)(l-m-1)}{(2l+3)(2l+1)}\right)^{\frac{1}{2}}, \\
A_4^{l,m} &= \frac{1}{2}\left(\frac{(l+m)(l+m-1)}{(2l+1)(2l-1)}\right)^{\frac{1}{2}}, \\
A_5^{l,m} &= \left(\frac{(l+m)(l-m)}{(2l+1)(2l-1)}\right)^{\frac{1}{2}}, \\
A_6^{l,m} &= \left(\frac{(l+m+1)(l-m+1)}{(2l+3)(2l+1)}\right)^{\frac{1}{2}} . \qquad (1.21)
\end{aligned}$$

The terms with invalid values for α and γ will be assumed to be 0.

To obtain the $P1$ approximation, $L = 1$ is taken in the previous system (1.11), and in the series expansion for the angular flux the remaining terms are Φ_0^0,Φ_1^1 ,Φ_1^0 and Φ_1^1 , and all the coefficients of higher order are considered equal to zero. The following notation is introduced

$$\begin{aligned}
\frac{Q_0^0(\vec{r}, E, t)}{H_0^0} &= \tilde{Q}(\vec{r}, E, t) \\
\frac{\Phi_0^0(\vec{r}, E, t)}{H_0^0} &= \Phi(\vec{r}, E, t) \qquad (1.22)
\end{aligned}$$

where $\tilde{Q}$ means neutron source, and Φ is the scalar neutron flux. Imposing the following conditions.

$$\frac{\partial \Phi_1^{-1}}{\partial t}(\vec{r}, E, t) = \frac{\partial \Phi_1^0}{\partial t}(\vec{r}, E, t) = \frac{\partial \Phi_1^1}{\partial t}(\vec{r}, E, t) = 0, \qquad (1.23)$$

the following system of equations is obtained

$$\begin{aligned}
-\frac{1}{v}\frac{\partial\Phi}{\partial t}(\vec{r},E,t) = &-\sqrt{\frac{1}{6}}\left(\frac{\partial}{\partial x}-i\frac{\partial}{\partial y}\right)\frac{\Phi_1^{-1}(\vec{r},E,t)}{H_0^0} \\
&-\sqrt{\frac{1}{6}}\left(\frac{\partial}{\partial x}+i\frac{\partial}{\partial y}\right)\frac{\Phi_1^{1}(\vec{r},E,t)}{H_0^0} \\
&-\sqrt{\frac{1}{3}}\left(\frac{\partial}{\partial z}\right)\frac{\Phi_1^{0}(\vec{r},E,t)}{H_0^0}+\Sigma_T(\vec{r},E,t)\Phi(\vec{r},E,t) \\
&-\int_0^\infty dE'\Sigma_{s0}(\vec{r},E'\rightarrow E,t)\Phi(\vec{r},E',t) \\
&-(1-\beta\ )\frac{\chi_p(E)}{4\pi}\int_0^\infty dE'\nu\Sigma_f(\vec{r},E',t)\Phi(\vec{r},E',t) \\
&-\tilde{Q}(\vec{r},E,t)-\sum_{k=1}^{K}\lambda_k\frac{\chi_k(E)}{4\pi}\mathcal{C}_k(\vec{r},t)\ ,
\end{aligned}\tag{1.24}$$

$$\begin{aligned}
\sqrt{\frac{1}{6}}\left(\frac{\partial}{\partial x}+i\frac{\partial}{\partial y}\right)\Phi_0^0(\vec{r},E,t) = &\ \Sigma_T(\vec{r},E,t)\Phi_1^{-1}(\vec{r},E,t) \\
&-\int_0^\infty dE'\Sigma_{s1}(\vec{r},E'\rightarrow E,t)\Phi_1^{-1}(\vec{r},E',t),
\end{aligned}\tag{1.25}$$

$$\begin{aligned}
\sqrt{\frac{1}{3}}\left(\frac{\partial}{\partial z}\right)\Phi_0^0(\vec{r},E,t) = &\ \Sigma_T(\vec{r},E,t)\Phi_1^{0}(\vec{r},E,t) \\
&-\int_0^\infty dE'\Sigma_{s1}(\vec{r},E'\rightarrow E,t)\Phi_1^{0}(\vec{r},E',t),
\end{aligned}\tag{1.26}$$

$$\begin{aligned}
\sqrt{\frac{1}{6}}\left(\frac{\partial}{\partial x}-i\frac{\partial}{\partial y}\right)\Phi_0^0(\vec{r},E,t) = &\ \Sigma_T(\vec{r},E,t)\Phi_1^{1}(\vec{r},E,t) \\
&-\int_0^\infty dE'\Sigma_{s1}(\vec{r},E'\rightarrow E,t)\Phi_1^{1}(\vec{r},E',t),
\end{aligned}\tag{1.27}$$

Moreover, it is supposed that the inelastic neutron scattering is isotropic, which implies that Σ_{s1} only describes the elastic scattering. It is considered that the anisotropic elastic scattering is done without change in the neutron's energy, and then it can be written

$$\Sigma_{s1}(\vec{r},E'\rightarrow E)J(\vec{r},E')dE' = \Sigma_{s1}(\vec{r},E\rightarrow E')J(\vec{r},E)dE',$$

where the right-hand side can also be rewritten as

$$\Sigma_{s1}(\vec{r},E)J(\vec{r},E),$$

with

$$\Sigma_{s1}(\vec{r},E) = \int_0^\infty \Sigma_{s1}(\vec{r},E \to E')dE' \ .$$

The transport cross section is defined as

$$\Sigma_{tr}(\vec{r},E,t) = \Sigma_T(\vec{r},E,t) - \bar{\Sigma}_{s1}(\vec{r},E),t),$$

and the diffusion coefficient

$$D(\vec{r},E,t) = \frac{1}{3\Sigma_{tr}(\vec{r},E,t)}.$$

Now it will be used the newly defined terms to write equations (1.25),(1.26)and (1.27) as follows

$$\begin{aligned}
\Phi_1^{-1}(\vec{r},E,t) &= \sqrt{\frac{3}{2}}D(\vec{r},E,t)\left(\frac{\partial}{\partial x} + i\frac{\partial}{\partial y}\right)\Phi_0^0(\vec{r},E,t),\\
\Phi_1^0(\vec{r},E,t) &= -\sqrt{3}D(\vec{r},E,t)\left(\frac{\partial}{\partial z}\right)\Phi_0^0(\vec{r},E,t),\\
\Phi_1^1(\vec{r},E,t) &= -\sqrt{\frac{3}{2}}D(\vec{r},E,t)\left(\frac{\partial}{\partial x} - i\frac{\partial}{\partial y}\right)\Phi_0^0(\vec{r},E,t). \qquad (1.28)
\end{aligned}$$

Substituting equations (1.28) in the equation (1.24) to obtain a formulation depending only on Φ_0^0 , and then using the definition (1.22) of Φ, it is obtained

$$\begin{aligned}
-\frac{1}{v}\frac{\partial\Phi}{\partial t}(\vec{r},E,t) = &-\frac{\partial}{\partial x}D(\vec{r},E,t)\frac{\partial}{\partial y}\Phi(\vec{r},E,t)\\
&-\frac{\partial}{\partial y}D(\vec{r},E,t)\frac{\partial}{\partial y}\Phi(\vec{r},E,t)\\
&-\frac{\partial}{\partial z}D(\vec{r},E,t)\frac{\partial}{\partial z}\Phi(\vec{r},E,t) + \Sigma_T(\vec{r},E,t)\Phi(\vec{r},E,t)\\
&-\int_0^\infty dE'\Sigma_{s0}(\vec{r},E' \to E,t)\Phi(\vec{r},E',t)\\
&-(1-\beta\ )\frac{\chi_p(E)}{4\pi}\int_0^\infty dE'\nu\Sigma_f(\vec{r},E',t)\Phi(\vec{r},E',t)\\
&-\tilde{Q}(\vec{r},E,t) - \sum_{k=1}^{K}\lambda_k\frac{\chi_k(E)}{4\pi}\mathcal{C}_k(\vec{r},t)\ . \qquad (1.29)
\end{aligned}$$

This is,

$$
\begin{aligned}
-\frac{1}{v}\frac{\partial\Phi}{\partial t}(\vec{r},E,t) = &-\vec{\nabla}.\left(D(\vec{r},E,t)\vec{\nabla}\Phi(\vec{r},E,t)\right) + \Sigma_T(\vec{r},E,t)\Phi(\vec{r},E,t) \\
&-\int_0^\infty dE'\Sigma_{s0}(\vec{r},E'\to E,t)\Phi(\vec{r},E',t) \\
&-(1-\beta\ )\frac{\chi_p(E)}{4\pi}\int_0^\infty dE'\nu\Sigma_f(\vec{r},E',t)\Phi(\vec{r},E',t) \\
&-\tilde{Q}(\vec{r},E,t) - \sum_{k=1}^{K}\lambda_k\frac{\chi_k(E)}{4\pi}\mathcal{C}_k(\vec{r},t)\ . \qquad (1.30)
\end{aligned}
$$

Moreover, taking into account that the neutron current, $\vec{J}$, is defined as

$$
\vec{J}(\vec{r},E,t) \equiv \int_{\vec{\Omega}} d\vec{\Omega}\vec{\Omega}\Phi(\vec{r},E,\vec{\Omega},t)\ ,
$$

from where

$$
\begin{aligned}
\vec{J}(\vec{r},E,t) = &\frac{\Phi_1^1(\vec{r},E,t)-\Phi_1^{-1}(\vec{r},E,t)}{2H_1^1}\ \vec{i} \\
&-\frac{i\Big(\Phi_1^1(\vec{r},E,t)+\Phi_1^{-1}(\vec{r},E,t)\Big)}{2H_1^1}\ \vec{j} + \frac{\Phi_1^0(\vec{r},E,t)}{H_1^0}\ \vec{k}. \qquad (1.31)
\end{aligned}
$$

Substituting equations (1.28) in equation (1.31) it is obtained

$$
\vec{J}(\vec{r},E,t) = -D(\vec{r},E,t)\vec{\nabla}\Phi(\vec{r},E,t),
$$

which is known as the Fick's first law.

The cross sections, generally, are functions depending on the neutrons energy, and to simplify the neutron diffusion equation it is used a multi-group approximation. Such an approximation consists of obtaining an equation for the neutrons whose energy belongs to the interval $[E_g\ ,E_{g+1}]$, $g=1,....,G-1$, where G is the number of groups to be considered.

The magnitudes associated with group g are defined as follows,

$$\begin{aligned}
\Phi_g(\vec{r},t) &= \int_{E_g}^{E_{g+1}} dE\ \Phi(\vec{r},E,t)\ , \\
\frac{1}{v_g} &= \int_{E_g}^{E_{g+1}} dE\ \frac{1}{v}\frac{\Phi(\vec{r},E,t)}{\Phi_g(\vec{r},t)}\ , \\
\Sigma_{Tg}(\vec{r},t) &= \int_{E_g}^{E_{g+1}} dE\ \Sigma_T(\vec{r},E,t)\frac{\Phi(\vec{r},E,t)}{\Phi_g(\vec{r},t)}\ , \\
\nu\Sigma_{fg}(\vec{r},t) &= \int_{E_g}^{E_{g+1}} dE\ \nu\Sigma_f(\vec{r},E,t)\frac{\Phi(\vec{r},E,t)}{\Phi_g(\vec{r},t)}\ , \\
\tilde{Q}_g(\vec{r},t) &= \int_{E_g}^{E_{g+1}} dE\ \tilde{Q}(\vec{r},E,t)\ , \\
\chi_{pg} &= \int_{E_g}^{E_{g+1}} dE\ \chi_p(E)\ , \\
\chi_{kg} &= \int_{E_g}^{E_{g+1}} dE\ \chi_k(E)\ , \\
\Sigma_{sg'\to g}(\vec{r},t) &= \int_{E'_g}^{E_{g'+1}} dE' \int_{E'_g}^{E_{g'+1}} dE\ \Sigma_{s0}(\vec{r},E'\to E,t)\frac{\Phi(\vec{r},E,t)}{\Phi'_g(\vec{r},t)}\ ,
\end{aligned} \tag{1.32}$$

and for each spatial direction, j , the diffusion coefficient for the group g is defined as the function $D_g(\vec{r},t)$ satisfying the following equation,

$$D_g(\vec{r},t) = \int_{E_g}^{E_{g+1}} dE D(\vec{r},E,t)\frac{\partial_j\Phi(\vec{r},E,t)}{\partial_j\Phi_g(\vec{r},t)}\ .$$

The total cross section is written as the sum of an absorption term and scattering terms of the form

$$\Sigma_{Tg}(\vec{r},t) = \Sigma_{ag}(\vec{r},t) + \sum_{g'=1}^{G}\Sigma_{sg'g}(\vec{r},t)\ ,$$

and the scattering cross section for the group g is introduced as

$$\Sigma_{sg}(\vec{r},t) = \sum_{g'\neq g}^{G}\Sigma_{sg'g}(\vec{r},t)\ .$$

Integrating the equation (1.30) from E_g to E_{g+1} , and making use of the previous definitions, the diffusion equation for the group g is obtained as

$$\begin{aligned}-\frac{1}{v}\,\frac{\partial \Phi_g}{\partial t}(\vec{r},t) &= \vec{\nabla}.\left(D_g(\vec{r},t)\vec{\nabla}\Phi_g(\vec{r},t)\right) - \left(\Sigma_{ag}(\vec{r},t)+\Sigma_{sg}(\vec{r},t)\right)\Phi_g(\vec{r},t)\\ &+\sum_{g'\neq g}^{G}\Sigma_{sg'g}(\vec{r},t)\Phi_{g'}(\vec{r},t)+(1-\beta\ )\chi_{pg}\sum_{g'=1}^{G}\Sigma_{fg'}(\vec{r},t)\Phi_{g'}(\vec{r},t)\\ &+\sum_{k=1}^{K}\lambda_k\chi_{kg}\mathcal{C}_k(\vec{r},t)+\tilde{Q}(\vec{r},t). \qquad (1.33)\end{aligned}$$

With these approximations, the equation (1.3) for the concentration of neutron precursors is written in the form

$$\frac{d\mathcal{C}_k(\vec{r},t)}{dt}=\beta_k\sum_{g'=1}^{G}\nu\Sigma_{fg}(\vec{r},t)\Phi_g(\vec{r},t)-\lambda_k\mathcal{C}_k(\vec{r},t). \qquad (1.34)$$

It is worth to note that, when approximating equations (1.2) and (1.3) by means of equations (1.33) and (1.34), the space where the fields are defined has been reduced from the space characterized by the variables $(\vec{r},E,\Omega,t)$ to the coordinate space $(\vec{r},t)$, with the consequent simplification of the problem.

From now on, the two energy groups neutron diffusion equation is considered, i.e., the energy spectrum is divided into a fast group E_1 , corresponding to the neutrons whose energy is higher to certain value, and a thermal group E_2 , corresponding to the neutrons whose energy is smaller than the previous quantity. Moreover, it is assumed than there are not scattering processes from the thermal to the fast group, i.e.,$\Sigma_{21}(\vec{r},t)=0$, and there is not neutron production in the thermal group, i.e., $\chi_{p2}=0$ and $\chi_{k2}=0$. Finally, it is supposed that there is no neutron external source, and $\chi_{p1}=1$ and $\chi_{k1}=1$. Making use of these considerations, a system of partial differential equations for the fast and the thermal group is obtained with the following form

$$[v^{-1}]\frac{\partial \Phi}{\partial t}+\mathcal{L}\Phi=(1-\beta\ )\mathcal{M}\Phi+\sum_{k=1}^{K}\lambda_k\chi\mathcal{C}_k \quad , \qquad (1.35)$$

$$\frac{\partial \mathcal{C}_k}{\partial t}=\dot{\mathcal{C}}_k=\beta_k[\nu\Sigma_{f1}\ \nu\Sigma_{f2}]\Phi-\lambda_k\mathcal{C}_k \quad , \quad k=1,\ldots,K \quad , \qquad (1.36)$$

where, K is the number of delayed neutron precursors groups considered and the matrices are defined as

$$\mathcal{L} = \begin{pmatrix} -\vec{\nabla}\cdot(D_1\vec{\nabla}) + \Sigma_{a1} + \Sigma_{12} & 0 \\ -\Sigma_{12} & -\vec{\nabla}\cdot(D_2\vec{\nabla}) + \Sigma_{a2} \end{pmatrix}, \quad [v^{-1}] = \begin{pmatrix} \frac{1}{v_1} & 0 \\ 0 & \frac{1}{v_2} \end{pmatrix},$$

$$\mathcal{M} = \begin{pmatrix} \nu\Sigma_{f1} & \nu\Sigma_{f2} \\ 0 & 0 \end{pmatrix}, \quad \Phi = \begin{pmatrix} \phi_1 \\ \phi_2 \end{pmatrix}, \quad \chi = \begin{pmatrix} 1 \\ 0 \end{pmatrix},$$

where ϕ_1 and ϕ_2 are the fast and the thermal neutron fluxes, respectively. The diffusion constants and cross-sections, D_g, Σ_{12}, Σ_{ag}, $\nu\Sigma_{fg}$, $g = 1,\ 2$, appearing in the equations depend on the reactor materials, that is, they are position and time dependent functions. β_k is the yield of delayed neutrons in the k precursors group and λ_k is the corresponding decay constant. Both coefficient are related to the delayed neutron precursor decay.

1.5 Lambda Modes equation

A reactor is said to be critical when the material configuration inside the reactor is set in a way that the neutron production is equal to the neutron loss. Under these conditions the reactor is in steady state. To study the steady state of a given reactor using the neutron diffusion equation, its criticality can be forced artificially [40], dividing the fission cross sections by a number λ. In such a way, it is expected that there exists a number λ satisfying the equations

$$\mathcal{L}\Phi = \frac{1}{\lambda}(1-\beta\ )\ \mathcal{M}\Phi\ + \sum_{k=1}^{K}\lambda_k\mathcal{C}_k\chi, \tag{1.37}$$

$$0 = \frac{1}{\lambda}\beta_k\,[\nu\Sigma_{f1}\nu\Sigma_{f2}]\,\Phi\ - \lambda_k\mathcal{C}_k. \tag{1.38}$$

Substituting (1.37) in (1.38), and taking into account that $\sum_{k=1}^{K}\beta_k\ = \beta\ $, it is obtained

$$\mathcal{L}\Phi = \frac{1}{\lambda}\mathcal{M}\Phi \tag{1.39}$$

which is known as the Lambda Modes equation for the reactor, and is a generalized differential eigenvalue problem associated with the operators $\mathcal{L}$ and $\mathcal{M}$, where $\mathcal{L}$ is the neutron loss operator and $\mathcal{M}$ is the neutron production operator. We will consider the approximation of two groups of energy, that the neutrons are born in the fast group, and that there is not up-scattering from the thermal to the fast group. Taking into account these assumptions, the looses operator is

$$\mathcal{L} = \begin{pmatrix} -\vec{\nabla}\cdot(D_1\vec{\nabla}) + \Sigma_{a1} + \Sigma_{12} & 0 \\ -\Sigma_{12} & -\vec{\nabla}\cdot(D_2\vec{\nabla}) + \Sigma_{a2} \end{pmatrix} ,$$
$$\mathcal{M} = \begin{pmatrix} \nu\Sigma_{f1} & \nu\Sigma_{f2} \\ 0 & 0 \end{pmatrix} , \quad \Phi = \begin{pmatrix} \phi_1 \\ \phi_2 \end{pmatrix} .$$

In order to study the steady state neutron flux distribution inside a nuclear reactor and the sub-critical modes responsible for example for the regional instabilities that can take place in its core, it is necessary to obtain the dominant modes and their corresponding eigenfunctions. The computation of modes can also be important in transient analysis, in which the problem must be solved each certain time step. In this last case, it is critical to be able to compute the modes solution as fast as possible [41].

For a numerical treatment, this equation must be discretised in space. Nodal methods are extensively used in this case. These methods are based on approximations of the solution in each node in terms of an appropriate basis of functions such as Legendre polynomials [42]. In this work the spatial discretization selected will be a hight order finite element method that will be described later. It is assumed that nuclear properties are constant in every cell. This process allows the transformation of the original system of partial differential equations into an algebraic large sparse generalised eigenvalue problem

$$L\tilde{\phi} = \frac{1}{\lambda} M\tilde{\phi} , \tag{1.40}$$

where L and M are matrices of order $2N$ with the following block structure

$$\begin{pmatrix} L_{11} & 0 \\ -L_{21} & L_{22} \end{pmatrix} \begin{pmatrix} \tilde{\boldsymbol{\phi}}_{\mathbf{1}} \\ \tilde{\boldsymbol{\phi}}_{\mathbf{2}} \end{pmatrix} = \frac{1}{\lambda} \begin{pmatrix} M_{11} & M_{12} \\ 0 & 0 \end{pmatrix} \begin{pmatrix} \tilde{\boldsymbol{\phi}}_{\mathbf{1}} \\ \tilde{\boldsymbol{\phi}}_{\mathbf{2}} \end{pmatrix} , , \tag{1.41}$$

By eliminating $\tilde{\phi}_2$, we obtain the following N-dimensional non-symmetric standard algebraic eigenproblem

$$L_{11}^{-1}\left(M_{11} + M_{12}L_{22}^{-1}L_{21}\right)\tilde{\boldsymbol{\phi}}_{\mathbf{1}} = \lambda\tilde{\boldsymbol{\phi}}_{\mathbf{1}} . \tag{1.42}$$

The eigenvalues λ associated with the equation 1.42) are interpreted as cross sections factors. Then, they must be necessarily real numbers, and thus the eigenfunctions $\tilde{\phi}_1$ will also be real functions.

It is usually supposed that the Lambda Modes form a complete set of functions for the development of modal methods for the integration of the time dependent neutron diffusion equation [43]. Thus, the problem of determining the Lambda

Modes of a given reactor can be considered as a previous problem for the study of the characteristics of the time dependent neutron diffusion equation.

1.6 VVER reactors

The Lambda Modes problem for reactor cores with geometries based on quadrilateral prisms, has been widely studied [10, 11, 4, 5, 6]. The developed methods are used to analyze reactors of type PWR and BWR, which are the most used occidental reactors. To analyze VVER reactors it is necessary to modify the methodologies applied when discretizing the equations, due to the geometry composed by hexagonal prisms (See Figure 1.2). Due to this fact it is interesting to study different methods for these reactors. VVER is the acronym of the Russian name Voda Voda Energo Reactor. VVER reactors are the Russian version of the PWR, and they have been developed along three different generations [12].

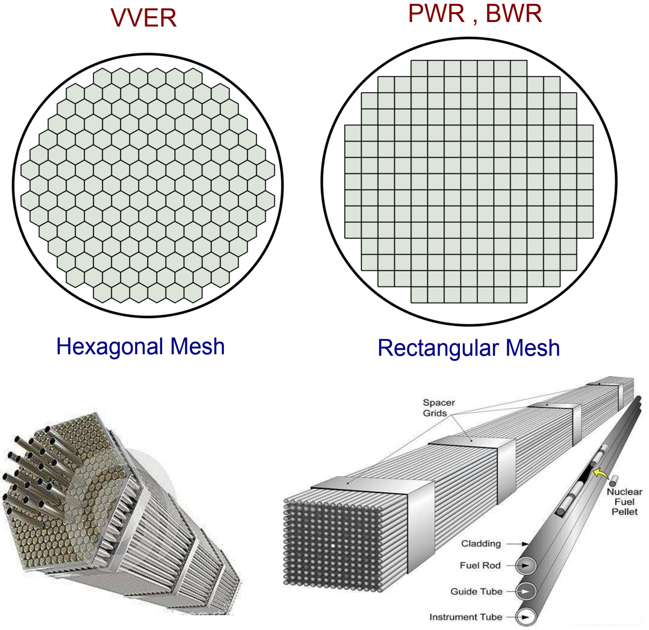

Figure 1.2: Core mesh for the VVER and PWR reactor.

The first generation (VVER-440 Model 230) was developed in the 60's. Their principal strengths are [26]

- Six primary coolant loops, each with a horizontal steam generator, which together provide a large volume of coolant.
- Isolation valves that allow plant operators to take one or more of the six coolant loops out of service for repair while continuing to operate the plant.
- Ability to sustain a simultaneous loss of coolant and off-site power, due to coolant pumps and two internal power generators that "coast down" after a shutdown.
- Plant worker radiation levels reportedly lower than many western plants, due to selection of materials, high-capacity primary coolant purification system, and water chemistry control.
- Ability to produce significant amounts of power despite design and instrumentation and control deficiencies.

Meanwhile the principal deficiencies are:

- Accident Localization System (which serves as a reactor confinement) designed to handle only one four-inch pipe rupture. If larger coolant pipes rupture occurs, this system vents directly to the atmosphere through nine large vent valves. Western nuclear plants have containments designed for rupture of the largest pipes. In addition, the confinement has very small volume, very poor leak-tightness and poor hydrogen mitigation.
- No emergency core cooling systems or auxiliary feed-water systems similar to those required in western nuclear plants.
- Major concern about embrittlement (gradual weakening) of the reactor pressure vessel surrounding nuclear fuel, due to lack of internal stainless-steel cladding and use of low-alloy steel with high levels of impurities.
- Plant instrumentation and controls, safety systems, fire protection systems, and protection for control room operators are below western standards.
- Quality of materials, construction, operating procedures and personnel training are below western standards.

The second generation (VVER-440 Model 213) was designed between 1950 and 1980. Their principal strengths are:

- Upgraded Accident Localization System vastly improved over the earlier VVER-440 Model V230 design, comparable to several western plants, and using a vapour-suppression confinement structure called a "bubbler-condenser" tower.

- Addition of emergency core cooling and auxiliary feedwater systems.
- Reactor pressure vessel with stainless-steel internal lining to alleviate much concern about the vessel embrittlement associated with the earlier VVER-440 Model V230 design.
- Improved coolant pump, and continued use of six coolant loops (providing multiple paths for cooling the reactor) and horizontal steam generators (for better heat transfer) with large coolant volume.
- Standardization of plant components, providing extensive operating experience for many parts and making possible incremental improvements and backfits of components.

Meanwhile the principal deficiencies are:

- Plant instrumentation and controls for example, reactor protection systems and diagnostics behind western standards. Significant variations exist among countries with VVER-440 Model V213 plants.
- Separation of plant safety systems (to help assure that an event in one system will not interfere with the operation of others), fire protection, and protection for control room operators improved over Model V230 plants, but generally below western standards.
- Poor leak-tightness of confinement.
- Unknown quality of plant equipment and construction, due to lack of documentation on design, manufacturing and construction, and reported instances of poor-quality materials being re-worked at plant sites.
- Major variations in operating and emergency procedures, operator training, and operational safety (for example, use of control-room simulators) among plants. These aspects of plant operations depend primarily on the organization or country operating Model V213 plants rather than on the plant supplier. Some countries have added safety features to their Model V213 plants.

These two kind of reactors has six loops and produce 444 Mw of power.

The third generation (VVER-1000) was developed between 1975 and 1985. These reactors have four loops and produce 1000 MW of power. They have a new design, to incorporate the new safety standards, where the principals strengths of these reactors are:

- Steel-lined, pre-stressed, large-volume concrete containment structure, similar in function to western nuclear plants.
- "Evolutionary" design incorporating safety improvements over VVER-440 Model V213 plants. The Soviet approach to standardization was based on continued use of components that had performed well in earlier plants.
- Use of four coolant loops and horizontal steam generators-both considered improvements by Soviet designers.
- Redesigned fuel assemblies that allow better flow of coolant, and improved control rods.
- Plant worker radiation levels reportedly lower than in many western plants, apparently due to selection of materials, high-capacity system for purifying primary coolant, and water chemistry control.

The most important deficiencies of this type of reactors are:

- Substandard plant instrumentation and controls. Wiring of emergency electrical system and reactor protection system does not meet western standards for separation-control and safety functions are interconnected in ways that may allow failure of a control system to prevent operation of a safety system.
- Fire protection systems that do not appear to differ substantially from earlier VVER models, which do not meet western standards.
- Quality control, design and construction significantly deficient by U.S. standards.
- Protection measures for control-room operators essentially unchanged from earlier VVER-440 Model V213 design, which does not meet U.S. standards. Unlike all U.S. nuclear plants, and most in western countries, VVER-1000s have no on-site "technical support center" to serve as a command post for stabilizing the plant in an emergency. Technical support centers were incorporated in U.S. and many western nuclear plants following the accident at Three Mile Island Unit 2 in 1979.
- Operating and emergency procedures that fall far short of western standards and vary greatly among operators of VVER-1000 plants.
- Higher power densities and the smaller volume of primary and secondary systems result in a somewhat less forgiving and stable reactor.

Nowadays, new designs are being studied, such as the new VVER-1200 [44] (which supposes a substantial improvement of the VVER-1000), VVER-1500 and VVER-1600 [45], which are not operative yet.

The main difference between the VVER and the western PWR is the fuel assemblies design and the core geometry. The VVER have fuel assemblies with the shape of hexagonal prisms, instead of the fuel assemblies with the shape of paralepipedal prisms for the western PWR (See Figure 1.2).

The VVER-440 reactor core has 312 fuel assemblies and 37 control rods. 30 of these fuel rods are always outside, (as it is shown in Figure 1.3). The different colors indicate different materials composing the fuel.

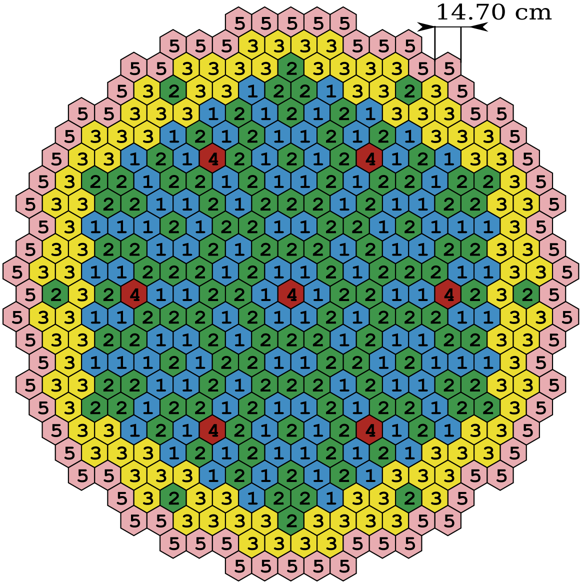

Figure 1.3: Layout of the VVER-440 core reactor.

Another example of the hexagonal reactors is the VVER-1000 reactor core which has 167 fuel assembles as shown in Figure 1.4.

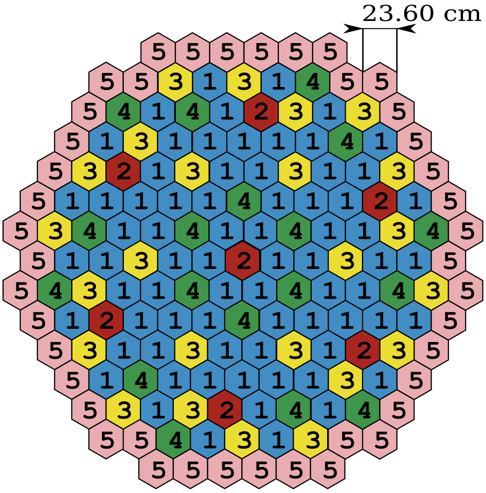

Figure 1.4: Layout of the VVER-1000 core reactor.

1.7 The deal.II finite element library

The spatial discretization selected for the neutron diffusion equation is a high order finite element method,which has been implemented making use of deal.II [46],[8].

deal.II is an object-oriented class library providing all tools needed for simulations with the finite element method, targeted at the computational solution of partial differential equations using adaptive finite elements. Using the structuring means of C++, the different objects used in such a simulation program are well separated, allowing for a wide variation of applications without sacrificing program structure or increasing susceptibility to programming errors. In particular, the strict separation of meshes, finite element spaces and linear algebra classes allows for a very modular approach in programming applications built on deal.II, and to combine the provided functionality in many different ways, suiting the particular needs of an application. It uses state-of-the-art programming techniques to offer a modern interface to the complex data structures and the algorithms required.

The library uses advanced object-oriented and data encapsulation techniques to break finite element implementations into smaller blocks that can be arranged to fit users requirements. Through this approach, deal.II supports a large number of different applications covering a wide range of scientific areas, programming methodologies, and application-specific algorithms, without imposing a rigid framework into which they have to fit. A judicious use of programming techniques allows to avoid the computational costs frequently associated with abstract object-oriented class libraries.

The main aim of deal.II is to enable rapid development of modern finite element codes, using among other aspects adaptive meshes and a wide array of tools classes often used in finite element program.

The development of deal.II (and its predecessor DEAL) was initiated by the need for a software tool for research in novel adaptive and high-performance finite element schemes of a number of areas. Most available software tools would either be tuned to performance, but be specialized to one class of applications, while others offer flexibility and generality at a significant waste of memory and computing power. In addition, very few packages were publicly available at the time. Therefore, DEAL filled a gap when its design began in 1992 and was the software basis of the development of goal oriented error estimation and adaptive methods for partial differential equations [47],[48],[49]. However, by 1997, it became clear that some concepts of DEAL had become too cumbersome, and that important improvements could be made by building on the then recent developments in the C++ programming language [50] and compilers for it, in particular mature support for templates and the standard template library [51] , [52]. Therefore, a fresh start was made with the new implementation of deal.II.

deal.II is widely used in many academic and commercial projects. For its creation, its principal authors have received the 2007 J. H. Wilkinson Prize for Numerical Software. It is also part of the industry standard (SPEC CPU 2006) benchmark suite used to determine the speed of computers and compilers, and comes preinstalled on the machines offered by the commercial Sun Grid programs.

Among other features, deal.II offers:

- Support for one, two, and three space dimensions, using a unified interface that allows to write programs almost dimension independent.
- Handling of locally refined quadrangular grids, including different adaptive refinement strategies based on local error indicators and error estimators. Both *h,p* , and *h-p* refinement is fully supported for continuous and discontinuous elements.
- Support for a variety of finite elements: Lagrange elements of any order, continuous and discontinuous; Nedelec and Raviart-Thomas elements of any order; elements composed of other elements.
- Parallelization on single machine through the Threading Build Blocks and across nodes via MPI. deal.II has been shown to scale to at least 16k processors.

- Modern software techniques that make access to the complex data structures and algorithms as transparent as possible. The use of object oriented programming allows for program structures similar to the structures in mathematical analysis.

- A complete stand-alone linear algebra library including sparse matrices, vectors, Krylov subspace solvers, support for blocked systems, and interface to other packages such as Trilinos [53], PETSc [54] and METIS [55], [56].

- Support for several output formats, including many common formats for visualization of scientific data.

- Portable support for a variety of computer platforms and compilers.

1.7.1 Interfaces to other software

In addition to the functionality deal.II provides itself, it also has interfaces to numerous additional programs and libraries for pre- and post-processing as well as linear algebra. A list of areas in which deal.II uses external programs is the following one :

- *Grid generators.* The grid handling of deal.II always assumes that there is a coarse mesh approximating the geometry of the domain of computation. While the mesh refinement process is able to follow curved boundaries, the coarse mesh has to be provided either internally using functions for a simple hypercube, or externally through mesh generators. deal.II has the capability to read several different mesh formats, among which are UCD [57], Gmsh, and NetCDF [58].

- *Linear algebra.* While deal.II provides an extensive suite of linear algebra classes for the iterative solution of linear systems, it does not offer direct or sparse direct solvers for large matrices. However, interfaces to the sparse direct solvers in the UMFPACK [59] and HSL [60] packages are provided; a copy of UMFPACK is actually part of deal.II distributions, courtesy of the author. In addition, basic support for LAPACK [61] eigenvalue solvers exists. Interfaces exist for linear algebra libraries such as PETSC, SLEPC and ARPACK [62].

- *Parallelization.* deal.II includes genuine support for shared memory parallelization by multi-threading, a significant advantage at a time when multiprocessor and multicore machines become more common. For parallelization by message passing, an interface to PETSc [63] is provided. Since PETSc relies on MPI, it is portable to a large number of parallel systems. Interfaces to METIS [56] can be also used to partition meshes efficiently.

- *Visualization.* The library has output drivers for a significant number of different visualization tools as well as its own Postscript output. Generation of output data is implemented as a two-step process, where the first generates an intermediate format from simulation data independent of the actual output format, and the second step them converts this, rather simple, intermediate data into one of the supported graphical formats. It is therefore quite simple to write a new driver for a missing file format. At present, the following formats are supported: VTK [64] , OpenDX in both text and binary format, UCD format for AVS Express , binary and text files for Tecplot [65], Gnuplot [66], encapsulated postscript, and GMV [67].

1.8 The PETSc library

The Portable, Extensible Toolkit for Scientific Computation [63] (PETSc, pronounced PET-see; the S is silent), is a suite of data structures and routines developed by Argonne National Laboratory for the scalable (parallel) solution of scientific applications modeled by partial differential equations. It employs the Message Passing Interface (MPI) standard for all message-passing communication.

PETSc is the world's most widely used parallel numerical software library for partial differential equations and sparse matrix computations. It provides support for problems arising from discretization by means of regular meshes as well as unstructured meshes. Its approach is to encapsulate mathematical algorithms using object-oriented programming techniques in order to be able to manage the complexity of efficient numerical message-passing codes [41].

PETSc is intended for use in large-scale application projects, many ongoing computational science projects are built around the PETSc libraries. Its careful design allows advanced users to have detailed control over the solution process. PETSc includes a large suite of parallel linear and nonlinear equation solvers that are easily used in application codes written in C, C++, Fortran and now Python.

PETSc is built around a variety of data structures and algorithmic objects. The application programmer works directly with these objects rather than concentrating on the underlying data structures. The three basic abstract data objects are index sets (IS), vectors (Vec) and matrices (Mat). Built on top of this foundation are various classes of solver objects, including linear, nonlinear and time-stepping solvers [41]. In addition, PETSc includes support for parallel distributed arrays useful for finite difference methods.

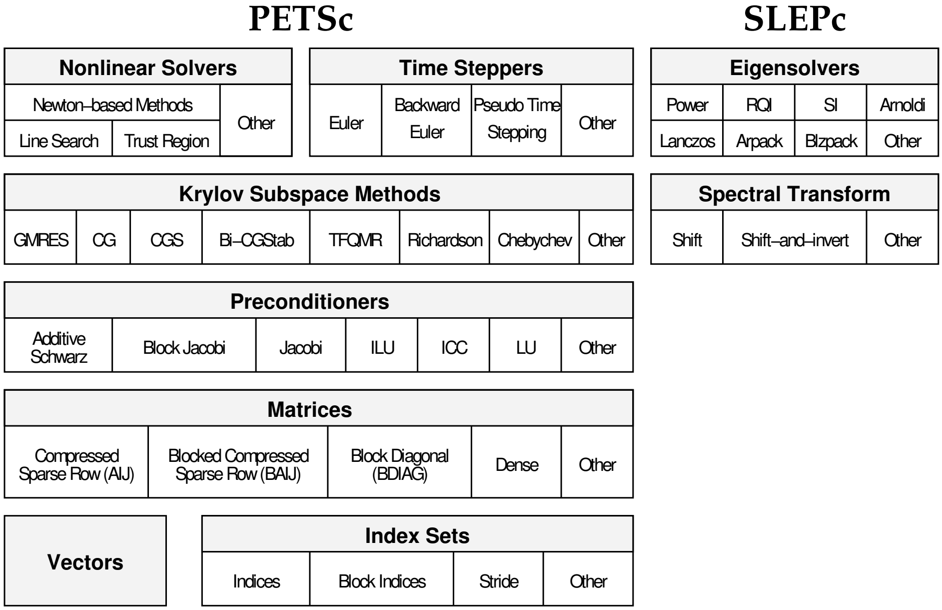

Figure 1.5: Structure of PETSc (on the left) and SLEPc (on the right).

1.9 The SLEPc library

Eigenvalue problems are a very important class of linear algebra problems. The need for the numerical solution of these problems, associated with stability and vibrational analysis, arises in a wide range of situations in science and engineering. They are usually formulated as large sparse eigenproblems. SLEPc is one of the most complete and widely used libraries that deals with the solution of sparse eigenvalue problems.

SLEPc, the Scalable Library for Eigenvalue Problem Computations SLEPc [54], is a software library for the solution of large sparse eigenproblems on parallel computers. It can be used for the solution of problems formulated in either standard or generalized form, as well as other related problems such as the singular value decomposition or the quadratic eigenvalue problem.

The emphasis of the software is on methods and techniques appropriate for problems in which the associated matrices are sparse, for example, those arising after the discretization of partial differential equations. Therefore, most of the methods offered by the library are projection methods or other methods with similar properties. Examples of these methods are Krylov-Schur, Jacobi-Davidson, and Subspace Iteration, to name a few. SLEPc provides implementations of these methods. It also provides built-in support for spectral transformations such as the shift-and-invert technique. SLEPc is a general library in the sense that it covers standard and generalized eigenvalue problems, both Hermitian and non-Hermitian, with either real or complex arithmetic.

SLEPc is based on the PETSc data structures and extends its functionality in order to solve eigenproblems arising in real applications by using well-known techniques such as shift-and-invert and state-of-the-art methods, in addition employs the MPI standard for message-passing communication. It is being developed by researchers from Universitat Politécnica de Valéncia (Spain).

1.10 Gmsh

Gmsh [68] is a three dimensional finite element grid generator with a build-in CAD (Computer-Aided Design) engine and post-processor capabilities including advanced means for manipulation and visualization of the data. Its design goal is to provide a fast, light and user-friendly meshing tool with parametric input and advanced visualization capabilities.

Gmsh is built around four modules: geometry, mesh, solver and post-processing. All geometrical, mesh, solver and post-processing instructions are prescribed either interactively using the graphical user interface (GUI) or in text files using Gmsh's own scripting language. Interactive actions generate language bits in the input files, and vice versa. This makes possible to automate all treatments, using loops, conditionals and external system calls. To describe geometries this mesh generator uses a boundary representation ("b-rep" is a method for representing shapes using the limits)[69].

As a general procedure for mesh generators (and also for Gmsh), first we have to generate geometrical entities by successively defining points, oriented lines (line segments, circles, ellipses, splines), oriented surfaces (plane surfaces, ruled surfaces, triangulated surfaces) and volumes; in this order), each one has assigned an identifier (a number) at the moment they are created. In Gmsh there are also physical groups, that are simply and basically a group of geometrical entities (points, lines, surfaces or volumes) and they have also an identifier. Nevertheless, they cannot be modified by geometry commands.

Once the geometry is defined, we have to specify (as far as possible) how the FEM elements have to be generated by elementary geometrical elements of various shapes (lines, triangles, quadrangles, tetrahedra, prisms,hexahedra and pyramids). And finally, we order to mesh them (i.e., generation of the FE nodes and elements).

The mesh generation is performed in the same bottom-up flow as the geometry creation: lines are discretized first; the mesh of the lines is then used to mesh the surfaces; then the mesh of the surfaces is used to mesh the volumes.

The generation of meshes is done on parametric surface patches like non-uniform rational B-Splines (NURBS). A speciality of Gmsh is the integrated adaption of the mesh element sizes to features. It supports a variety of 2D meshing strategies in addition to Delaunay triangulation and natively Delaunay Tetrahedalization and Advancing Front schemes for 3D volume meshing. It has both a convenient language and graphical user interface (GUI) for description and manipulation of the geometry.

Additionally, Gmsh can provide quality-optimal tetrahedral elements in volume meshes. Another advantageous feature of this software package is its capability to visualize and manipulate geometrical entities, mesh elements and the results of calculations.

It is well known that the most laborious and error prone tasks in performing numerical simulation is the input of the initial data that describe the geometry of the device as well as its subsequent modification. This problem can be solved using the functionality of Gmsh as geometrical modeller and CAD program. FEM models can be generated graphically (through the GUI of Gmsh), or by use of scripts (a file containing the instructions for the mesh generation).

Gmsh scripts have the extension'.geo'. In these scripts, we can define all the instructions than can also be input graphically. The use of these scripts has many advantages:

- We can re-use it for other models.
- We can parameterize the model, in order to be able to change dimensions or properties without the need to start from zero.
- Portability is better.The script file occupies some kbytes, while a model can be quite large to back it up.The only disadvantage is that it has to be re-run to get the model.

The reactor core consist of several fuel elements across the diameter with hexagonal shape, namely cells as shown in Figure 1.6. The number and the pitch size of this fuel elements depend to the core type geometry. As the deal.II library doesn't support the Hexadric cells, the geometry is transformed to quadrilateral cell with Gmsh as shown in Figure 1.6.

As beginning to generate the mesh we made a script containing the instructions for the mesh generation. Each point is specified by three Cartesian coordinates (X,Y,Z). Thus, for each line, the points along it are specified. To each point a

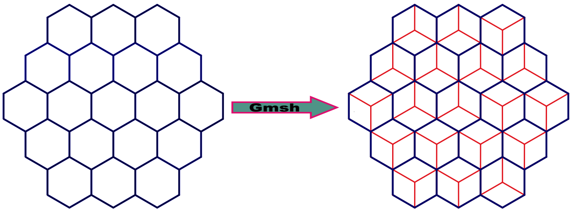

Figure 1.6: Hexadric cells transformed into quadrilaterals with Gmsh.

fourth parameter, namely the characteristic length lc is associated, which controls the sizes of the finite elements. Then from points we compose lines and from lines we compose the hexagonal. The hexagonal are used to describe closed loops that bound surfaces. Three-dimensional volumes are created either by rotation or by extrusion of surfaces. They can also be specified defining a sequence of surfaces (plane or ruled) that encompass the closed space.

It can easily be manipulated and/or modified using the GUI of the code or editing the ASCII file (∗.geo file) that contains the description of the geometrical data. Each of the elementary entities, as well as all the complex elements are identified by unique names and numbers that are used for their description and also for attachment of appropriate boundary conditions to them. Additionally, the GUI allows one to specify the visibility individually to any element or to a combination of elementary entities and in such a way to visualize selectively different parts of the geometry.

The final step here is to export the mesh. To this just push the Save button and a .msh format mesh file will be produced. This will then need to be copied to the deal.II directory.

Chapter 2

Hexagonal Reactors : Static Calculation

Most of the simulation codes of a nuclear power reactor use the multigroup neutron diffusion equation to describe the neutron distribution inside the reactor core. The neutron diffusion equation is an approximation of the neutron transport equation that states that the neutron current is proportional to the gradient of the neutron flux by means of a diffusion coefficient. This approximation is analogous to the Fick's law in species diffusion and to the Fourier law in heat transfer.

As it has been explained in Chapter 1, for a given configuration of a nuclear reactor core it is always possible to force its criticality dividing the neutron production rate due to fission by a positive number, λ, obtaining a generalized differential eigenvalue problem, known as the Lambda Modes equation (equation (1.37)), which is solved to obtain the dominant eigenvalues of the reactor and their corresponding eigenfunctions.

Therefore this turns the formulation into a differential generalized eigenvalue problem. The fundamental eigenvalue (the one with the largest magnitude which is known as the $\mathrm{k_{eff}}$ of the reactor core) shows the criticality of the reactor core and its corresponding eigenfunction describes the steady state neutron distribution in the core. Next sub-critical eigenvalues and their corresponding eigenfunctions are interesting because they have been successfully used to develop modal methods to integrate the time dependent neutron diffusion equation [70]. Also the sub-critical modes have been used to classify BWR instabilities [71], [72].

The Lambda Modes problem has been studied for reactors with rectangular geometry as the PWR and BWR [10, 11, 2, 6]. To discretize the problem for reactors with a hexagonal geometry, as for example the VVER reactors, a different strategy is necessary because the design of these reactors define a natural mesh with hexagonal cells instead of rectangular cells.

Different methods have been proposed to solve the neutron diffusion equation on hexagonal geometry as, for example, the Fourier transform method [73], the conformal mapping method [74], the polynomial expansion nodal method [75], etc. All these methods compute the k_{eff} and the stationary neutron flux in the reactor core by means of a system of non linear equations, which is solved iteratively. To obtain a set of dominant modes it is necessary to approximate the initial differential eigenvalue problem (equation (1.37)), by a generalized algebraic eigenvalue problem. This can be done, for example, by using a finite element method [76] or finite difference method [77]. On the other hand, for nuclear reactors the spatial mesh is naturally defined by the different materials defining the core, and for this reason, it is interesting to use a method that can use this kind of coarse meshes.

Finite elements methods have been used in rectangular geometry to analyze the PWR and BWR [78], and in hexagonal geometries [2]. Adaptivity is one of main advantages in the use of the finite element method. h-adaptable meshes have been proposed to obtain the static configuration of a nuclear reactor core with the use of triangular finite elements [79] and rectangular elements [8]. Also unstructured grid schemes have been developed to solve the problem in non standard geometries [80].

In this chapter, an h-p finite element method is used to obtain the dominant Lambda Modes associated with a configuration of a reactor core. The first step to discretize a multidimensional reactor with hexagonal geometry, for dimensions $\mathrm{d} = 2, 3$, is to divide each hexagonal prism or hexagonal element into three rectangular prisms or rectangular elements. The rectangular prisms or rectangular elements of the discretization will be denoted by Ω_e and will be referred as elements, independently of the dimension for the problem, $\mathrm{d} = 2, 3$. In order to increase the accuracy of the solution of the finite element method it is necessary to refine the mesh used. Two main different refinement techniques exist such as h-refinement and p-refinement. In h-refinement, the finite elements are spatially subdivided into smaller ones, keeping the original element boundaries intact. p-refinement increases the polynomial degree of the basic functions used in the expansions increasing the exactitude of the solution. Most of the literature [81] advise to use h-refinement in regions where the solution is not rough or possesses singularities. Otherwise, the p-refinement is advised in regions where the solution is smooth. Sometimes, it is possible to combine efficiently the h- and p-refinements and call it the h-p refinement. In this procedure both the size of elements h and their degree of polynomial p are altered. To select which cells are refined an error estimator is used. Thus, all the process is automatic leading to Automatic Mesh Refinement. Also, with the h-refinement is possible to solve the neutron diffusion equation with cross sections assembly averaged for the majority of fuel assemblies and pin-cell averaged for a particular fuel assembly of interest.

2.1 *h-p* finite element method

The usual finite element analysis would proceed from the selection of a mesh and basis to the generation of a solution to an accuracy appraisal and analysis. Experience is the traditional method of determining whether or not the mesh and basis will be optimal or even adequate for the analysis at hand. Accuracy appraisals typically require the generation of a second solution on a finer mesh or with a different method and an comparison of the two solutions. At least with a posteriori error estimation, accuracy appraisals can accompany solution generation at a lower cost than the generation of a second solution.

The theory of a posteriori error estimations [6], [5] has matured and allows the measure, control and minimization of approximation errors. In this theory, the computed solution itself is used to provide inexpensively point-wise error estimations. In the framework of finite element methods, there are several factors on which one can play to reduce the error in a cell chosen for refinement: (1) the cell can be subdivided in smaller cells, h-method, or (2) the polynomial order representation for the numerical solution of that cell can be increased, p-method. While both of these options perform better than uniform mesh refinement, neither is independently optimal.

- While h-refinement is indicated for regions where the solution is not smooth, such as domain corners or zones with significant material property discontinuities, it does not deliver the best convergence rate for regions where the solution is smooth.
- On the other hand, p-refinement is ideal for zones with a smooth solution but it should not be applied in regions where the solution is irregular, as near boundaries or material interfaces.

However, it is possible to combine the advantages of both methods into what is commonly termed the h-p-refinement technique where the choice between a mesh subdivision and an increase in the polynomial order is based on a competitive minimization of local errors. Adaptive h-p-FEM encompasses both h-FEM and p-FEM but importantly, it also performs h-p refinements where an element is subdivided and many possible combinations of polynomial degrees on the subelements are probed. The main idea of the multimesh discretization is that each physical component is discretized on an individual mesh that, moreover, is being adapted in such a way that the overall error is reduced most efficiently.

The h-p finite element method was proposed more than two decades ago by Babuska and Guo [5], [46] as an alternative to either (i) mesh refinement (i.e. decreasing the mesh parameter h in a finite element computation) or (ii) increasing the polynomial degree p used for shape functions. It is based on the observation that increasing the polynomial degree of the shape functions reduces the approximation error if the solution is sufficiently smooth. On the other hand, it is well known that even for the generally well-behaved class of elliptic problems, higher degrees of regularity can not be guaranteed in the vicinity of boundaries, corners, or where coefficients are discontinuous [82], [83]; consequently, the approximation can not be improved in these areas by increasing the polynomial degree p but only by refining the mesh, i.e. by reducing the mesh size h. These differing means to reduce the error have led to the notion of h-p finite elements, where the approximating finite element spaces are adapted to have a high polynomial degree p wherever the solution is sufficiently smooth, while the mesh width h is reduced at places wherever the solution lacks regularity. It was already realized in the first papers on this method that h-p finite elements can be a powerful tool that can guarantee that the error is reduced not only with some negative power of the number of degrees of freedom, but in fact exponentially.

2.2 Discretization of the problem

The Lambda Modes equation in the approximation of two groups of energy without up-scattering is considered. This equation can be expressed as [40],

$$\begin{pmatrix} -\vec{\nabla}(D_1\vec{\nabla}) + \Sigma_{a1} + \Sigma_{12} & 0 \\ -\Sigma_{12} & -\vec{\nabla}(D_2\vec{\nabla}) + \Sigma_{a2} \end{pmatrix} \begin{pmatrix} \phi_1 \\ \phi_2 \end{pmatrix} = \frac{1}{\lambda} \begin{pmatrix} \nu\Sigma_{f1} & \nu\Sigma_{f2} \\ 0 & 0 \end{pmatrix} \begin{pmatrix} \phi_1 \\ \phi_2 \end{pmatrix} , \tag{2.1}$$

where D_g, $g = 1, 2$ are the diffusion coefficients, Σ_{ag}, Σ_{fg} and Σ_{12} are the macroscopic cross sections of absorption, fission and scattering, respectively. ϕ_1 and ϕ_2 are the fast and thermal neutron fluxes, respectively. The weak formulation of this equation is obtained by pre-multiplying by a test function $\left(\varphi^T = \begin{pmatrix} \varphi_1, & \varphi_2 \end{pmatrix}\right)$ and integrating over the domain Ω, defining the reactor core [84],

$$\begin{aligned} \int\limits_{\Omega} \begin{pmatrix} \varphi_1 & \varphi_2 \end{pmatrix} \begin{pmatrix} -\vec{\nabla}(D_1\vec{\nabla}) + \Sigma_{a1} + \Sigma_{12} & 0 \\ -\Sigma_{12} & -\vec{\nabla}(D_2\vec{\nabla}) + \Sigma_{a1} + \Sigma_{12} \end{pmatrix} \begin{pmatrix} \phi_1 \\ \phi_2 \end{pmatrix} \mathrm{d}V \\ = \frac{1}{\lambda} \int\limits_{\Omega} \begin{pmatrix} \varphi_1 & \varphi_2 \end{pmatrix} \begin{pmatrix} \nu\Sigma_{f1} & \nu\Sigma_{f2} \\ 0 & 0 \end{pmatrix} \begin{pmatrix} \phi_1 \\ \phi_2 \end{pmatrix} \mathrm{d}V \ . \end{aligned} \tag{2.2}$$

The vectorial identity, $\vec{\nabla} \cdot \left(u\vec{\nabla}v\right) = \left(\vec{\nabla}u\right) \cdot \left(\vec{\nabla}v\right) + u\left(\vec{\nabla} \cdot \vec{\nabla}v\right)$, is applied and expression (2.2) is rewritten as

$$\begin{aligned}
&\int_{\Omega} \vec{\nabla}\varphi_1 D_1 \vec{\nabla}\phi_1 \mathrm{d}V - \int_{\Omega} \vec{\nabla} \cdot \left(\varphi_1 D_1 \vec{\nabla}\phi_1\right) \mathrm{d}V + \int_{\Omega} \varphi_1 \left(\Sigma_{a1} + \Sigma_{12}\right) \phi_1 \mathrm{d}V + \\
&+ \int_{\Omega} \vec{\nabla}\varphi_2 D_2 \vec{\nabla}\phi_2 \mathrm{d}V - \int_{\Omega} \vec{\nabla} \cdot \left(\varphi_2 D_2 \vec{\nabla}\phi_2\right) \mathrm{d}V + \int_{\Omega} \varphi_2 \Sigma_{a2} \phi_2 \mathrm{d}V + \\
&- \int_{\Omega} \varphi_2 \Sigma_{12} \phi_1 \mathrm{d}V = \frac{1}{\lambda} \left(\int_{\Omega} \varphi_1 \nu \Sigma_{f1} \phi_1 \mathrm{d}V + \int_{\Omega} \varphi_1 \nu \Sigma_{f2} \phi_2 \mathrm{d}V \right) . \qquad (2.3)
\end{aligned}$$

Using Gauss Divergence theorem $\left(\int_{\Omega} \vec{\nabla} \cdot \vec{F} \mathrm{d}V = \int_{\Gamma} \vec{F} \mathrm{d}\vec{S}\right)$ to eliminate second order derivatives,

$$\begin{aligned}
&\int_{\Omega} \vec{\nabla}\varphi_1 D_1 \vec{\nabla}\phi_1 \mathrm{d}V - \int_{\Gamma} \varphi_1 D_1 \vec{\nabla}\phi_1 \mathrm{d}\vec{S} + \int_{\Omega} \varphi_1 \left(\Sigma_{a1} + \Sigma_{12}\right) \phi_1 \mathrm{d}V + \\
&+ \int_{\Omega} \vec{\nabla}\varphi_2 D_2 \vec{\nabla}\phi_2 \mathrm{d}V - \int_{\Gamma} \varphi_2 D_2 \vec{\nabla}\phi_2 \mathrm{d}\vec{S} + \int_{\Omega} \varphi_2 \Sigma_{a2} \phi_2 \mathrm{d}V + \\
&- \int_{\Omega} \varphi_2 \Sigma_{12} \phi_1 \mathrm{d}V = \frac{1}{\lambda} \left(\int_{\Omega} \varphi_1 \nu \Sigma_{f1} \phi_1 \mathrm{d}V + \int_{\Omega} \varphi_1 \nu \Sigma_{f2} \phi_2 \mathrm{d}V \right) , \qquad (2.4)
\end{aligned}$$

is obtained, where Γ is the boundary of the domain defining the reactor core.

Finally, the reactor domain Ω is divided into cell subdomains Ω_e $(e = 1, ..., N_t)$ where it is assumed that the nuclear cross sections remain constant. Γ_e is also defined as the corresponding subdomain surface which is part of the reactor frontier Γ. Equation (2.4) is rewritten as

$$\begin{aligned}
&\sum_{e=1}^{N_t} \left(D_1 \int_{\Omega_e} \vec{\nabla}\varphi_1 \vec{\nabla}\phi_1 \mathrm{d}V - D_1 \int_{\Gamma_e} \varphi_1 \vec{\nabla}\phi_1 \mathrm{d}\vec{S} + \left(\Sigma_{a1} + \Sigma_{12}\right) \int_{\Omega_e} \varphi_1 \phi_1 \mathrm{d}V \; + \right. \\
&\quad + D_2 \int_{\Omega_e} \vec{\nabla}\varphi_2 \vec{\nabla}\phi_2 \mathrm{d}V - D_2 \int_{\Gamma_e} \varphi_2 \vec{\nabla}\phi_2 \mathrm{d}\vec{S} + \Sigma_{a2} \int_{\Omega_e} \varphi_2 \phi_2 \mathrm{d}V + \\
&\quad \left. - \Sigma_{12} \int_{\Omega_e} \varphi_2 \phi_1 \mathrm{d}V \right) = \frac{1}{\lambda} \sum_{e=1}^{N_t} \left(\nu \Sigma_{f1} \int_{\Omega_e} \varphi_1 \phi_1 \mathrm{d}V + \nu \Sigma_{f2} \int_{\Omega_e} \varphi_1 \phi_2 \mathrm{d}V \right) . \qquad (2.5)
\end{aligned}$$

It has to be noted that there are several surface integrals over the boundary of the subdomains (Γ_e) that rely on the boundary conditions and that will be studied below (Section 2.2.1). The solution ϕ_g is approximated through the usual trial solution as sum of shape functions u_j multiplied by their corresponding nodal values $\tilde{\phi}_{gj}$.

$$\phi_g \approx \sum_{j=0}^{p} u_j \tilde{\phi}_{gj} \; . \qquad (2.6)$$

In the same way, a Galerkin method [17] is used assuming that the test function are a finite set of shape functions [46]. Introducing these expressions in (2.5) and eliminating redundant coefficients to obtain continuous solutions (see, for example, [2] for more details) in terms of global coefficients, the procedure leads to an algebraic eigenvalue problem of the form

$$\begin{pmatrix} L_{11} & 0 \\ -L_{21} & L_{22} \end{pmatrix} \begin{pmatrix} \tilde{\phi}_1 \\ \tilde{\phi}_2 \end{pmatrix} = \frac{1}{\lambda} \begin{pmatrix} M_{11} & M_{12} \\ 0 & 0 \end{pmatrix} \begin{pmatrix} \tilde{\phi}_1 \\ \tilde{\phi}_2 \end{pmatrix} \ , \tag{2.7}$$

where $\tilde{\phi}_1$ and $\tilde{\phi}_2$ are the vectors of coefficients associated with the fast and thermal neutron fluxes, correspondingly.

The reactor domain, Ω, is divided into non-overlapping subdomains, Ω_e ($e = 1, ..., N_t$), or cells. In the same way, Γ_e is the corresponding element surface which is part of the reactor exterior boundary. The matrices elements of the different blocks appering in the Equation (4.45) are given by

$$\begin{aligned}(L_{11})_{ij} = \sum_{e=1}^{N_t} \Bigg(D_1 \int_{\Omega_e} \vec{\nabla} u_i \vec{\nabla} u_j \, \mathrm{d}V - D_1 \int_{\Gamma_e} u_i \vec{\nabla} u_j \, \mathrm{d}\vec{S} \\ + (\Sigma_{a1} + \Sigma_{12}) \int_{\Omega_e} u_i u_j \, \mathrm{d}V \Bigg) \ ,\end{aligned} \tag{2.8a}$$

$$(L_{21})_{ij} = \sum_{e=1}^{N_t} \Sigma_{12} \int_{\Omega_e} u_i u_j \, \mathrm{d}V \ , \tag{2.8b}$$

$$\begin{aligned}(L_{22})_{ij} = \sum_{e=1}^{N_t} \Bigg(D_2 \int_{\Omega_e} \vec{\nabla} u_i \vec{\nabla} u_j \, \mathrm{d}V \\ -D_2 \int_{\Gamma_e} u_i \vec{\nabla} u_j \, \mathrm{d}\vec{S} + \Sigma_{a2} \int_{\Omega_e} u_i u_j \, \mathrm{d}V \Bigg) \ ,\end{aligned} \tag{2.8c}$$

$$(M_{11})_{ij} = \sum_{e=1}^{N_t} \nu \Sigma_{f1} \int_{\Omega_e} u_i u_j \, \mathrm{d}V \ , \tag{2.8d}$$

$$(M_{12})_{ij} = \sum_{e=1}^{N_t} \nu \Sigma_{f2} \int_{\Omega_e} u_i u_j \, \mathrm{d}V. \ , \tag{2.8e}$$

These integrals have a local character, that is, only they are non zero for contiguous nodes, therefore highly sparse global matrices are obtained.

2.2.1 Boundary conditions

Implemented boundary conditions are zero-flux at the frontier, zero-current boundary condition and Albedo boundary conditions. These last conditions are mixed boundary conditions of the form

$$\vec{n}\vec{\nabla}\phi_g(\vec{x}) + \frac{1}{D_g}\frac{1-\beta}{2(1+\beta\ )}\phi_g(\vec{x}) = 0\ , \qquad \vec{x}\in\Gamma\ , \tag{2.9}$$

where $\vec{n}$ is the normal vector to the corresponding surface pointing outwards. If there are zero-flux boundary conditions, the shape functions of the corresponding nodes are fixed to zero. Thus, the number of degrees of freedom (DoF) of the problem is reduced because the nodes have their flux restricted. On the other hand, if the boundary conditions are zero-current conditions, the integral surface terms are equal to zero and the finite element formulation takes care of these conditions without restrictions in the nodes. Albedo boundary conditions are treated pre-multiplying the condition by the test function and integrating over the surface of the domain,

$$\int_\Gamma \varphi_g \left(D_g\vec{\nabla}\phi_g + \frac{1}{2}\Big(\frac{1-\beta}{1+\beta}\Big)\phi_g \right) \mathrm{d}\vec{S}\ . \tag{2.10}$$

That is ,

$$-D_g\int_\Gamma \varphi_g\vec{\nabla}\phi_g\mathrm{d}\vec{S} = \frac{1}{2}\Big(\frac{1-\beta}{1+\beta}\Big)\int_\Gamma \varphi_g\phi_g\mathrm{d}\vec{S}\ . \tag{2.11}$$

Hence, the surface terms that appear in Equation (2.8) are substituted by,

$$\sum_{e=1}^{N_t} -D_g\int_{\Gamma_e} N_{gi}\vec{\nabla}N_{gj}\mathrm{d}\vec{S} = \sum_{e=1}^{N_t}\frac{1}{2}\frac{1-\beta}{1+\beta}\int_{\Gamma_e} N_{gi}N_g\mathrm{d}\vec{S}\ . \tag{2.12}$$

2.2.2 Reference element

As it has been already mentioned, the whole reactor domain is discretized into cells. In order to define these subdomains always over the same reference cell an affine mapping is used to map each physical element to the reference element. An example for a bidimensional cell is shown in Figure 2.1.

This change of variables relates physical coordinates (x, y), with the coordinates of the reference domain (ξ, η) and it is given by

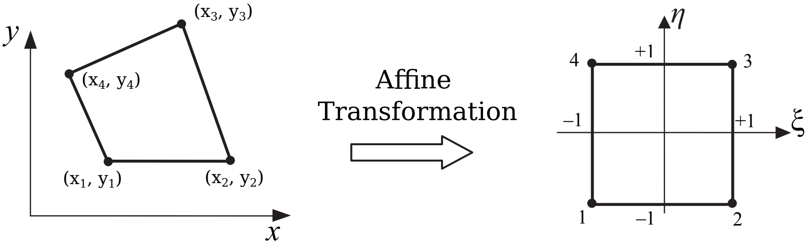

Figure 2.1: Affine transformation used.

$$x(\xi,\eta) = \frac{1}{4}(1-\xi)(1-\eta)x_1 + (1-\xi)(1+\eta)x_2 + (1+\xi)(1-\eta)x_3 + (1-\xi)(1+\eta)x_4 \tag{2.13}$$

$$y(\xi,\eta) = \frac{1}{4}(1-\xi)(1-\eta)y_1 + (1-\xi)(1+\eta)y_2 + (1+\xi)(1-\eta)y_3 + (1-\xi)(1+\eta)y_4 \tag{2.14}$$

This affine mapping helps to compute the integrals defining the matrix elements taking into account the Jacobian of the transformation $|\mathbf{J^e}|$,

$$\mathrm{d}V = \mathrm{d}x\mathrm{d}y = \begin{vmatrix} \frac{\partial x}{\partial \xi} & \frac{\partial y}{\partial \xi} \\ \frac{\partial x}{\partial \eta} & \frac{\partial y}{\partial \eta} \end{vmatrix} \mathrm{d}\xi\mathrm{d}\eta = |\mathbf{J^e}|\mathrm{d}\xi\mathrm{d}\eta \ . \tag{2.15}$$

2.2.3 Lagrange finite elements

For simplicity, Lagrange finite elements [17] are used. These elements have their nodes distributed forming a regular mesh over the cell. Their shape functions are defined with *Lagrange polynomials* for every dimension. These polynomials have a value of unity at the corresponding nodal point and zero at the other nodes and they satisfy all inter-element continuity conditions.

Lagrange polynomials are defined as,

$$l_I^p(\xi) = \frac{(\xi-\xi_1)\dots(\xi-\xi_{I-1})(\xi-\xi_{I+1})\dots(\xi-\xi_{p+1})}{(\xi_I-\xi_1)\dots(\xi_I-\xi_{I-1})(\xi_I-\xi_{I+1})\dots(\xi_I-x_{p+1})} = \prod_{\substack{k=1\\k\neq I}}^{p+1} \frac{\xi-\xi_k}{\xi_I-\xi_k} \ , \tag{2.16}$$

where p is the polynomial degree of the expansion which characterizes the polynomial degree of the finite element method, and ξ_i is the position of every node in the element. Multidimensional versions of these elements are obtained by tensor product of their elements. Thus, in two coordinates, if the node is labelled by its row and column I, J.

$$N_{I,J}(\xi,\eta) = l_I^p(\xi) l_J^p(\eta) \ . \tag{2.17}$$

Figure 2.2 shows the shape functions of some one-dimensional Lagrange elements and an example of these shape functions in a bidimensional element is displayed in Figure 2.3.

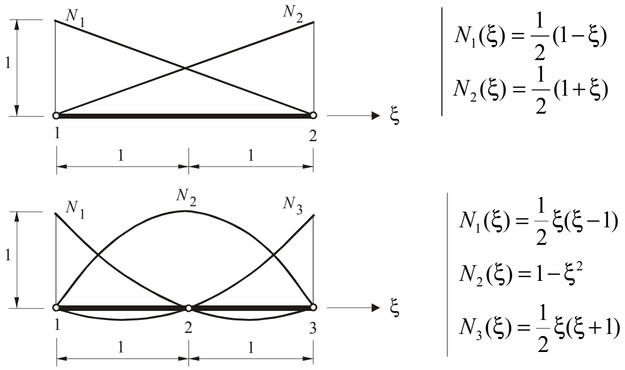

Figure 2.2: Example of unidimensional shape functions used, linear and quadratic.

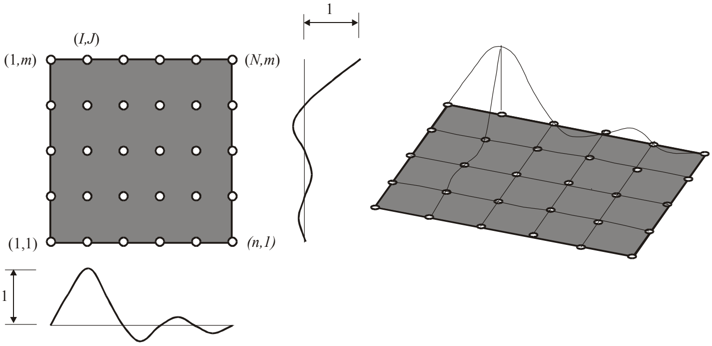

Figure 2.3: A typical shape function for a 2D Lagrangian element, (I=2, J=5, p=4).

The number of nodes in each cell, which is function of the finite element degree p, is the number of degrees of freedom in each cell. The total number of degrees of freedom of the problem is calculated multiplying the number of nodes per cell by the number of cells and removing the repeated nodes in the interface between cells. Finally, it should be noted that for the integration of the weak formulation in each cell a Gauss quadrature is used. The degree of the quadrature is selected ensuring an exact integration inside the approximation of polynomial shape functions.

2.2.4 Eigenvalue solver and postprocess

With the finite element method exposed above the Lambda Modes problem is approximated by a generalized algebraic eigenvalue problem. Normally the same quadrature points are used to compute the integrals and to define the lagrange finite elements with the following block structure

$$\begin{pmatrix} L_{11} & 0 \\ -L_{21} & L_{22} \end{pmatrix} \begin{pmatrix} \tilde{\boldsymbol{\phi}}_{\mathbf{1}} \\ \tilde{\boldsymbol{\phi}}_{\mathbf{2}} \end{pmatrix} = \frac{1}{\lambda} \begin{pmatrix} M_{11} & M_{12} \\ 0 & 0 \end{pmatrix} \begin{pmatrix} \tilde{\boldsymbol{\phi}}_{\mathbf{1}} \\ \tilde{\boldsymbol{\phi}}_{\mathbf{2}} \end{pmatrix} . \tag{2.18}$$

To solve this problem a Krylov-Schur method [85] is used from the library SLEPc [54]. First, the generalized problem is reduced to an ordinary eigenvalue problem,

$$L_{11}^{-1} \left(M_{11} + M_{12} L_{22}^{-1} L_{21} \right) \tilde{\boldsymbol{\phi}}_{\mathbf{1}} = \lambda \tilde{\boldsymbol{\phi}}_{\mathbf{1}} \ , \tag{2.19}$$

which is solved for n dominant eigenvalues and their corresponding eigenvectors. In this way, for each matrix-vector product it is necessary to solve two linear systems associated with the L_{11} and L_{22}, to avoid the calculation of their inverse matrices. These systems are solved by means of an iterative scheme as the preconditioned GMRES method [86]. Particularly, a Cuthill-McKee reordering [87] performed to reduce the bandwidth of the matrices, together with an incomplete LU factorization of the matrices is used for the preconditioning.

Once the fluxes are solved, other practical magnitudes are computed as the neutronic power that is defined as a weighted sum of the neutron fluxes,

$$P = \Sigma_{f1} |\phi_1| + \Sigma_{f2} |\phi_2| \ . \tag{2.20}$$

The eigenvectors should be normalized through some criteria. The most usual one is to fix the mean power productions to 1.

$$\bar{P} = \frac{1}{V_t} \int\limits_{\Omega} \left(\Sigma_{f1} |\phi_1| + \Sigma_{f2} |\phi_2| \right) \mathrm{d}V = 1, \tag{2.21}$$

where V_t is the total volume of the reactor.

It is needed to introduce the absolute value of the fluxes because this definition is extended to the subcritical eigenfunctions.

2.2.5 Refinement and error estimator

Once the problem is solved, it is convenient to estimate if the obtained solution has enough accuracy and, if not, refine the mesh accordingly. In this way, two types of refinements are considered, a global refinement, where all the cells are refined, and an adaptive refinement, where half of the cells are refined. To choose which cells are refined a modified version of the error estimator proposed by Kelly et al.[88] generalized for a non-constant diffusion coefficients [8] is used,

$$\eta_e^2 = \frac{h}{24}\Sigma_{f1}\int\limits_{\Gamma_e}\left(D_1\vec{\nabla}\phi_1\right)\mathrm{d}\vec{S} + \Sigma_{f2}\int\limits_{\Gamma_e}\left(D_2\vec{\nabla}\phi_2\right)\mathrm{d}\vec{S}\ , \tag{2.22}$$

where Γ_e is all interior boundaries of the element e and h is the adimensional cell size. In other words, we are using the jump in net current multiplied by the fission cross sections as an error estimator. Even though, this is an error estimator for the Poisson equation (for example $\nabla^2\varphi = f$), this indicator is widely used as a heuristic refinement indicator and it is considered a good choice in the absence of actual estimators for a particular equation [89].

2.3 Numerical results

To study the performance of the *h-p* finite element method exposed above to determine the Lambda Modes of a nuclear reactor, different benchmark problems have been considered. Firstly, we consider a homogeneous one energy group eigenvalue problem in one-dimension, which has analytical solution. For this problem, we compare the results obtained using the *h-p* finite element method, with the results obtained by the spectral element method (SEM) taked from the reference [26]. Then, six two-dimensional problems have been studied, the 2D homogeneous problem, the IAEA with and without reflector, the VVER-1000, the VVER-440 and the HWR.

Also, the three-dimensional VVER-440 problem has been studied. We study all these problems because different behaviour of the numerical methods can be shown at different benchmark problems, and then an exhaustive test has been done. The references for the $\mathrm{k_{eff}}$ results and for the power distribution is computed using the finite differences code DIF3D [74], where for the HWR problem a mesh of 384 triangles per hexagon was used, and for the rest of the problems a mesh of 864 triangles per hexagon was used.

Table 2.1: Different errors used for the spatial discretization.

Relative error	$\varepsilon_e = \lvert Pw_e - Pw_e^* \rvert / \lvert Pw_i \rvert$
Mean relative error	$\bar{\varepsilon} = \frac{1}{V_t} \sum_{e} \varepsilon_e V_e$
Maximum relative error	$\varepsilon_{\max} = \max_{e} \lvert \varepsilon_e \rvert$
Eigenvalue error (*pcm*)	$\Delta \mathrm{k}_{\mathrm{eff}} = 10^5 \; \lvert \mathrm{k}_{\mathrm{eff}} - \mathrm{k}_{\mathrm{eff}}^* \rvert$

To compare the performance of the finite element method using different types of meshes, refinement sizes and strategies for the spatial discretization, and to set the adequate spatial discretization parameters, different errors have been employed, which are shown in Table 2.1. In this Table, Pw_e and Pw_e^* are, respectively, the reference power and the computed power in the e-th cell [90] (cell averages), V_e is the volume of the e-th cell and V_t is the total volume of the reactor. $\mathrm{k}_{\mathrm{eff}}$ is the reference dominant eigenvalue of the reactor and $\mathrm{k}_{\mathrm{eff}}^*$ is the computed eigenvalue. Similar errors are defined for the neutron fluxes.

For all the problems we will show tables with the different values of the $\mathrm{k}_{\mathrm{eff}}$ obtained. Also the difference between the obtained result and the reference value are presented. This difference is denoted as $\Delta \mathrm{k}_{\mathrm{eff}}$ in *pcm* (percent-milli, i.e.,10^5). We also present results of the subcritical eigenvalues and the symmetry patterns of the power distribution associated with the modes of the reactor problems. The code has been written in C++ and executed in a computer with an Intel®i3-3220 @ 3.30GHz processor with 4 Gb of RAM running Ubuntu GNU/Linux 12.10. The number of eigenvalues requested has been set to 4 with a relative tolerance of 10^{-7} in all the examples.

2.3.1 1D Homogeneous eigenvalue problem

We consider a homogeneous slab of length $2cm$ [43], in the approximation of one group of energy and vacuum boundary conditions (see Figure 2.4). The nuclear cross sections for this problem are: $\Sigma_t = 1$, $\Sigma_s = 0.9$, and $\nu\Sigma_f = 0.25$.

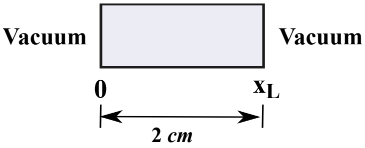

Figure 2.4: Homogeneous slab with vacuum boundary conditions.

First, we present the analytical solution for this problem [91], defining the parameter

$$\tau = \frac{1}{D}\big(\frac{1}{\lambda}\nu\Sigma_f - \Sigma_a\big) \tag{2.23}$$

we have the following differential eigenvalue problem,

$$\begin{aligned} &\frac{d^2\Phi_1}{dx^2}(x) + \tau\ \Phi(x) = 0, \qquad x \in [0, x_L], \\ &\Phi(0) - 2D\ \frac{d\Phi}{dx}(0) = 0, \\ &\Phi(x_L) + 2D\ \frac{d\Phi}{dx}(x_L) = 0\ . \end{aligned} \tag{2.24}$$

There exist non trivial solutions for the eigenvalue problem if, and only if, $\tau > 0$. Thus, the eigenvectors of problem (Equation (2.24)) are

$$\Phi(x) = c\ \big(\sin\big(t\frac{x}{x_L}\big) + \frac{2t}{3\Sigma_t x_L}\cos\ \big(t\frac{x}{x_L}\big)\big). \tag{2.25}$$

where $t = x_L\sqrt{\tau} > 0$ is a positive solution of the nonlinear equation

$$f(t) = \big(1 - \frac{4}{9(\Sigma_t x_L)^2}\ t^2\big)\sin(t) + \frac{4}{3\Sigma_t x_L} t\cos(t) = 0 \tag{2.26}$$

and the constant c is fixed once a normalization for the eigenvectors is chosen. Once we obtain, t, the zeros of $f(t)$, the eigenvalues of Equation (2.24) are

$$\lambda = \frac{x_L\nu\Sigma_f}{x_L\Sigma_a + \frac{t^2}{3\Sigma_t x_L}}. \tag{2.27}$$

Table 2.2: Eigenvalue results for the homogeneous reactor using uniform meshes.

FE Degree	***h*-*p*-FEM**		**SEM**	
p	λ_1	λ_2	λ_1	λ_2
1	0.586917	0.148273	0.587489	0.148478
2	0.587489	0.149134	0.587489	0.149134
3	0.587489	0.149135	0.587489	0.149134
4	0.587489	0.149135	0.587489	0.149135

The first 2 dominant eigenvalues obtained from the analytical solution (equation (2.27)) are $\lambda_1 = 0.587489$ and $\lambda_2 = 0.149135$. In Table 2.2, we show the results obtained for these first 2 dominant eigenvalues using the *h*-*p* finite element method compared to the results obtained by the spectral element method(SEM)[26].

Table 2.3 shows the results obtained for the first four subcritical eigenvalues computed with the FEM using different values of the polynomial degree (p) of the finite element approximation compared with the obtained by analytical solution. We observe that for this problem the method presents a good convergence rate for the eigenvalues.

Table 2.3: First 3 subcritical eigenvalues for the 1D homogeneous reactor using uniform meshes.

FE Degree	λ_1	λ_2	λ_3	λ_4
1	0.586917	0.148273	0.0574547	0.0286639
2	0.587489	0.149134	0.0583772	0.0295962
3	0.587489	0.149135	0.0583796	0.0296016
4	0.587489	0.149135	0.0583796	0.0296016
Analytical Solution	0.587489	0.149135	0.058380	0.029602

2.3.2 Homogeneous Reactor

The simplest theoretical bidimensional reactor is one consisting of a $2D$ rectangular homogeneous material. Even though this problem is completely theoretical, it is relevant because it can be solved analytically for all its eigenvalues. The Lambda Modes problem for a rectangle is defined as

$$
\begin{aligned}
-\vec{\nabla} D_1 \vec{\nabla}\phi_1(x,y) + \left(\Sigma_{a1}+\Sigma_{12}\right)\phi_1(x,y) &= \frac{1}{\lambda}\left(\nu\Sigma_{f1}\phi_1(x,y)+\nu\Sigma_{f2}\phi_2(x,y)\right) \ , \\
-\Sigma_{12}\phi_1(x,y) - \vec{\nabla} D_2 \vec{\nabla}\phi_2(x,y) + \Sigma_{a2}\phi_2(x,y) = 0 \ , &\qquad (x,y)\in[0,L_1]\times[0,L_2]=\Omega \ ,
\end{aligned}
\tag{2.28}
$$

with homogeneous boundary conditions

$$
\phi_g(0,y)=\phi_g(L_1,y)=0 \ , \qquad \phi_g(x,0)=\phi_g(x,L_2)=0 \ , \qquad g=1,2 \ . \tag{2.29}
$$

Using the variables separation method,

$$
\phi_g(x,y) = X_g(x)Y_g(y), \tag{2.30}
$$

where X_g and Y_g are solutions of

$$
\frac{\mathrm{d}^2 X_g}{\mathrm{d}x^2}(x) = \mu_x X_g(x), \qquad \frac{\mathrm{d}^2 Y_g}{\mathrm{d}y^2}(y) = \mu_y Y_g(y), \tag{2.31}
$$

satisfying,

$$
X_g(0)=X_g(L_1)=Y_g(0)=Y_g(L_2)=0 \ . \tag{2.32}
$$

Thus, these functions have the general form,

$$
\begin{aligned}
X_g &= A_{g,x}\cos\left(\mu_x x\right) + B_{g,x}\sin\left(\mu_x x\right) \ , \\
Y_g &= A_{g,y}\cos(\mu_y y) + B_{g,y}\sin(\mu_y y) \ .
\end{aligned}
\tag{2.33}
$$

Using the boundary conditions (2.29)

$$
X(x) = B_{g,x}\sin\left(\frac{n\pi}{L_1}\right) \ , \qquad \mu_x = \frac{n\pi}{L_1} \ , \tag{2.34}
$$

$$
Y(y) = B_{g,y}\sin\left(\frac{m\pi}{L_2}\right) \ , \qquad \mu_x = \frac{m\pi}{L_2} \ , \tag{2.35}
$$

and

$$
\mu^2 = \mu_x^2 + \mu_y^2 \ , \tag{2.36}
$$

with $n, m \in \mathbb{N}$. Different values of n, m correspond to the different eigenvalues and eigenfunctions of the reactor. The equations are joined as Equation (2.30),

$$\phi_g(x,y) = k_g \sin\left(\mu_x\right) \sin(\mu_y) \ . \tag{2.37}$$

The Equation (2.28) implies

$$\phi_1(x,y) = \frac{D_2\mu^2 + \Sigma_{a2}}{\Sigma_{12}} \phi_2(x,y) \ . \tag{2.38}$$

Solving for the eigenvalue from the Equation (2.28), it is obtained

$$\lambda = \frac{\nu\Sigma_{f1}\left(D_2\mu^2 + \Sigma_{a2}\right) + \nu\Sigma_{f2}\Sigma_{12}}{\left(D_2\mu^2 + \Sigma_{a2}\right)\left(\Sigma_{a1} + \Sigma_{12} + D_1\mu^2\right)} \ , \tag{2.39}$$

with the eigenfunctions

$$\phi_1(x,y) = k\left(\frac{D_2\mu^2 + \Sigma_{a2}}{\Sigma_{12}}\right) \sin\left(\mu_x x\right) \sin(\mu_y y) \ , \tag{2.40}$$

$$\phi_2(x,y) = k \sin\left(\mu_x x\right) \sin(\mu_y y) \ . \tag{2.41}$$

As the fluxes are defined up to a multiplicative constant k, these should be normalized with the criterion exposed in Equation (2.21),

$$\begin{aligned} 1 &= \frac{1}{V_t}\int_\Omega \left(\Sigma_{f1}|\phi_1| + \Sigma_{f2}|\phi_2|\right) \mathrm{d}V \\ &= \frac{1}{L_1 L_2}\left(\Sigma_{f1}\frac{D_2\mu^2 + \Sigma_{a2}}{\Sigma_{12}} + \Sigma_{f2}\right) \int_0^{L_1} \mathrm{d}x \int_0^{L_2} \mathrm{d}y \ |\phi_2| \ . \end{aligned} \tag{2.42}$$

Hence, the normalized magnitudes obtained are

$$\phi_1(x,y) = \left(\frac{D_2\mu^2 + \nu\Sigma_{a2}}{\nu\Sigma_{f1}D_2\mu^2 + \nu\Sigma_{f1}\Sigma_{a2} + \nu\Sigma_{f2}\Sigma_{12}}\right)\left(\frac{\pi^2}{4}\right) \sin\left(\frac{n\pi}{L_1}x\right) \sin\left(\frac{m\pi}{L_2}y\right) \ , \tag{2.43}$$

$$\phi_2(x,y) = \left(\frac{\Sigma_{12}}{\nu\Sigma_{f1}D_2\mu^2 + \nu\Sigma_{f1}\Sigma_{a2} + \nu\Sigma_{f2}\Sigma_{12}}\right)\left(\frac{\pi^2}{4}\right) \sin\left(\frac{n\pi}{L_1}x\right) \sin\left(\frac{m\pi}{L_2}y\right) \ , \tag{2.44}$$

$$P = \left(\Sigma_{f1}\phi_1 + \Sigma_{f2}\phi_2\right) = \frac{\pi^2}{4} \sin\left(\frac{n\pi}{L_1}x\right) \sin\left(\frac{m\pi}{L_2}y\right) \ . \tag{2.45}$$

This proves that the normalized neutron distribution in a homogeneous reactor does not depend on the nuclear properties of the material.

The material cross sections for the $(L_1 \times L_2)$ rectangular reactor are shown in Table 2.4. Table 2.5 shows the eigenvalue results using different number of cells and different finite element degrees.

Table 2.4: Geometry and cross section values for the homogeneous bidimensional reactor.

$\mathbf{L_1}$ cm	$\mathbf{L_2}$ cm	$\mathbf{D_1}$ $(\ cm)$	$\mathbf{D_2}$ $(\ cm)$	$\mathbf{\Sigma_{a1}}$ $(1/\ cm)$	$\mathbf{\Sigma_{a2}}$ $(1/\ cm)$	$\mathbf{\Sigma_{12}}$ $(1/\ cm)$	$\mathbf{\Sigma_{f1}}$ $(1/\ cm)$	$\mathbf{\Sigma_{f2}}$ $(1/\ cm)$	$\boldsymbol{\nu\Sigma_{f1}}$ $(1/\ cm)$	$\boldsymbol{\nu\Sigma_{f2}}$ $(1/\ cm)$
40	40	1.32	0.2772	0.0026562	0.071596	0.023106	0.0074527	0.13236	0.0074527	0.13236

The power distribution for the dominant eigenvalue and zero-flux boundary conditions using a very coarse mesh (16 cells, $p = 1$) is shown in Figure 2.5a and the relative power error distribution, ε_i, is shown in Figure 2.5b. It should be noted that the maximum difference with the analytical solution is up to 11% but the averaged relative error $(\bar{\varepsilon})$ is only about 3.04% .

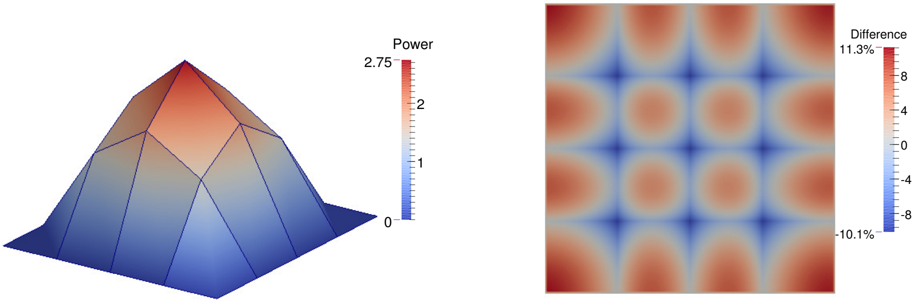

(a) Power distribution.

(b) Error distribution.

Figure 2.5: Fundamental mode power distribution and its error distribution for homogeneous reactor with zero-flux boundary conditions.

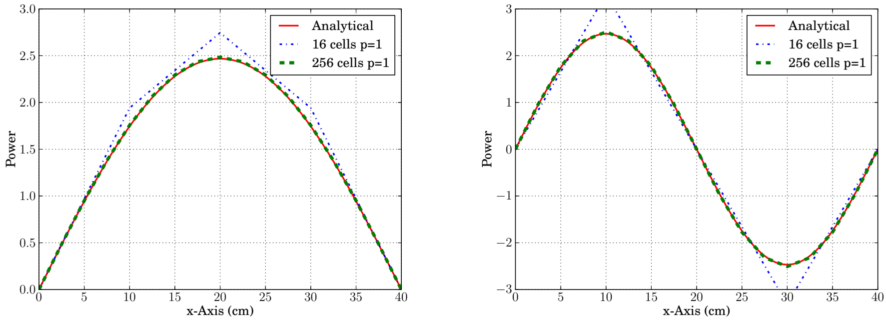

(a) 1st Mode.

(b) 2nd Mode.

Figure 2.6: Power distribution along the line $y = 20\ \ cm$ for the homogeneous bidimensional reactor.

Table 2.5: Eigenvalue results for the homogeneous bidimensional reactor using uniform meshes.

Number of cells	**FE Degree** p	**Number of DoF**	**1st Mode** λ_1	ϵ_{eig} $(\ pcm)$	**2nd Mode** λ_2	ϵ_{eig} $(\ pcm)$
16	1	25	1.12178	2186	0.60700	11536
256	1	289	1.14528	137	0.68092	764
4096	1	4225	1.14675	8.7	0.68587	42
16	2	81	1.14660	22	0.68322	429
256	2	1089	1.14685	0.3	0.68615	1.7
16	3	169	1.14685	0.2	0.68610	7.7
Analytical			1.14685		0.68616	

2.3.3 Two-dimensional IAEA problem without reflector

This problem is a modification of the PWR benchmark problem IAEA for rectangular elements. The core has 13 fuel elements across its diameter, as it is shown in Figure 2.7. There are 13 rodded assemblies, and it has a 1/12 reflective symmetry but, as the subcritical modes do not maintain this symmetry, all the computations are performed for the problem considering the whole reactor. The fuel assembly pitch is 20.0 cm.

The reflector is not included in the core, and we will consider vacuum boundary conditions, i.e., albedo boundary conditions with $\beta = 0$. The nuclear cross sections for this problem are shown in Table 2.6. The different results obtained for the

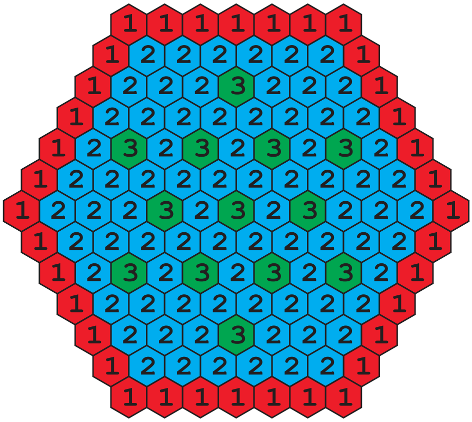

Figure 2.7: Geometry of the IAEA problem without reflector.

dominant eigenvalue k_{eff} of this reactor core together with the dimension of the blocks L_{11} and L_{22} , (DoF), and the nonzero elements of these matrices, (NNZ) are presented in Table 2.7.

Table 2.6: Nuclear cross sections definition for the IAEA problem without reflector.

Material	**Group**	$\mathbf{D_g}$ (cm)	$\boldsymbol{\Sigma_{ag}}$ (1/ cm)	$\boldsymbol{\Sigma_{12}}$ (1/ cm)	$\boldsymbol{\nu\Sigma_{fg}}$ (1/ cm)	$\boldsymbol{\Sigma_{fg}}$ (1/ cm)
1	1	1.5	0.01	0.02	0.0	0.0
	2	0.4	0.08		0.0135	0.056
2	1	1.5	0.01	0.02	0.0	0.0
	2	0.4	0.085		0.135	0.056
3	1	1.5	0.01	0.02	0.0	0.0
	2	0.4	0.13		0.135	0.056

Figure 2.8 shows the neutronic power distribution for each hexagon computed with the finite element method (FEM) using a polynomial degree $p = 6$ in the finite element expansion, together with the reference result [74] and the percentage of the relative error on each hexagon.

In Table 2.8, the results obtained for the first three subcritical eigenvalues computed with the FEM using different values of the polynomial degree p of the finite element approximation, are presented. The reference solution was extrapolated from DIF3D-FD runs with 864 hexagon subdivisions. Also the results obtained for the k_{eff} using PARCS [92] code has been included.

Table 2.7: Eigenvalue results and power distribution errors for the IAEA reactor without reflector.

Degree of FE	($\mathbf{k_{eff}}$)	$\mathbf{\Delta k_{eff}}$ (**pcm**)	$\varepsilon_{\max}$(%)	$\bar{\varepsilon}$ (%)	**DoF**	**NNZ**
1	0.972045	617	10	3.8	421	14188
2	0.977574	52	0.85	0.39	1603	98788
3	0.977990	9	0.40	0.09	3547	345244
4	0.978067	1	0.40	0.03	6253	881572
5	0.978074	0.3	0.39	0.029	9721	1872364
6	0.978076	0.1	0.39	0.029	13951	3518788
PARCS	0.978097	2	0.59	0.31		
Reference	0.9780770					

Table 2.8: First 3 subcritical eigenvalues for the IAEA reactor without reflector.

Degree of FE	λ_2	λ_3	λ_4
1	0.957759	0.957699	0.933083
2	0.962754	0.962753	0.938086
3	0.963111	0.963111	0.963111
4	0.963171	0.963171	0.938430
5	0.963178	0.963178	0.938437
6	0.963180	0.963180	0.938438

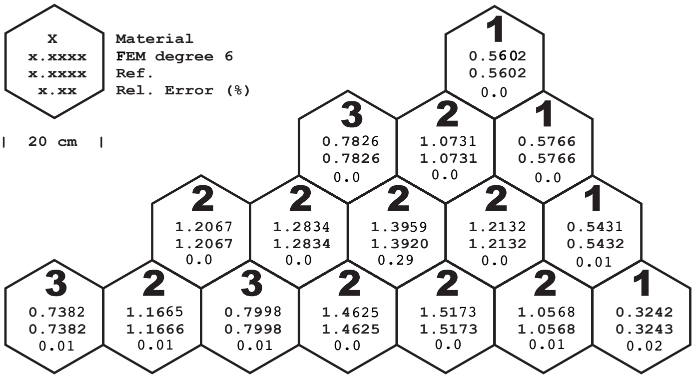

Figure 2.8: Power distribution for the IAEA problem without reflector with finite element degree $p = 6$.

2.3.4 Two-dimensional IAEA problem with reflector

This problem is the same as the previous one, except that in this problem an additional layer of water reflector surrounding the core is included, as shown in Figure.2.9. Also, vacuum boundary conditions are considered. The nuclear cross sections are presented in Table 2.9 and the different results obtained for the critical eigenvalue k_{eff} of this reactor core are shown in Table 2.10.

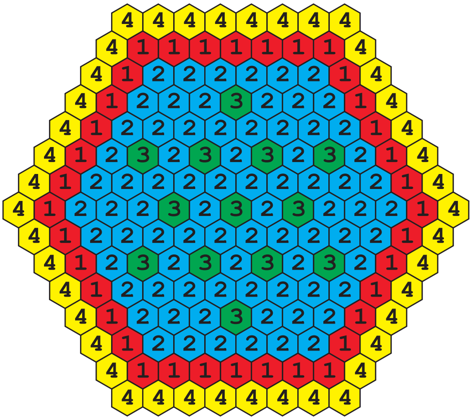

Figure 2.9: Geometry of the IAEA with reflector problem.

Table 2.9: Nuclear cross sections definition for the IAEA problem with reflector.

Material	Group	D_g (cm)	Σ_{ag} (1/ cm)	Σ_{12} (1/ cm)	$\nu\Sigma_{fg}$ (1/ cm)	Σ_{fg} (1/ cm)
1	1	1.5	0.01	0.02	0.0	0.0
	2	0.4	0.08		0.0135	0.056
2	1	1.5	0.01	0.02	0.0	0.0
	2	0.4	0.085		0.135	0.056
3	1	1.5	0.01	0.02	0.0	0.0
	2	0.4	0.13		0.135	0.056
4	1	1.5	0.0	0.04	0.0	0.0
	2	0.4	0.01		0.0	0.0

In Table 2.11, the results obtained for the first three subcritical eigenvalues computed with the FEM method using different values of the polynomial degree (p) of the finite element approximation, are presented.

Figure.2.10 shows the neutronic power distribution for each hexagon computed with the FE method using a polynomial degree $p = 6$ in the finite element polynomial expansion, together with the reference result [74] and the percentage of the relative error on each hexagon.

Table 2.10: Eigenvalue results and power distribution errors for the IAEA reactor with reflector.

Degree of FE	($\mathbf{k_{eff}}$)	$\mathbf{\Delta k_{eff}}$ (**pcm**)	$\varepsilon_{\max}$(%)	$\bar{\varepsilon}$ (%)	**DoF**	**NNZ**
1	1.01231	676	21.7	12.1	553	18796
2	1.00646	94.8	3.30	1.6	2119	131236
3	1.00557	6.3	0.36	0.18	4699	459004
4	1.00551	0.3	0.04	0.02	8293	1172452
5	1.00551	0.3	0.02	0.007	12901	2490604
6	1.00551	0.3	0.01	0.006	18523	4681156
PARCS	1.005657	15	0.34	0.019		
Reference	1.0055070					

Table 2.11: First 3 subcritical eigenvalues for the IAEA reactor with reflector.

Degree of FE	λ_2	λ_3	λ_4
1	1.004590	1.004290	0.986518
2	0.997652	0.997639	0.978167
3	0.996574	0.996573	0.976901
4	0.996497	0.996497	0.976799
5	0.996490	0.996490	0.976791
6	0.996490	0.996490	0.976791

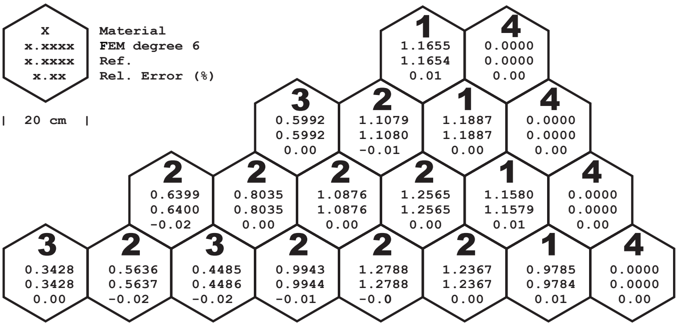

Figure 2.10: Power distribution for the IAEA problem with reflector with finite element degree p= 6.

2.3.5 Two-dimensional VVER-1000 reactor

The reactor core is VVER-1000 type, with 15 fuel elements along its diameter, with 25 control rods inserted. The geometry of this problem is shown in Figure 2.11. The core is composed of 163 assemblies of pitch equal to 23.60 *cm*. The reflector is not explicitly modeled, and vacuum boundary conditions are assumed. The nuclear cross sections of this problem are defined in Table 2.12.

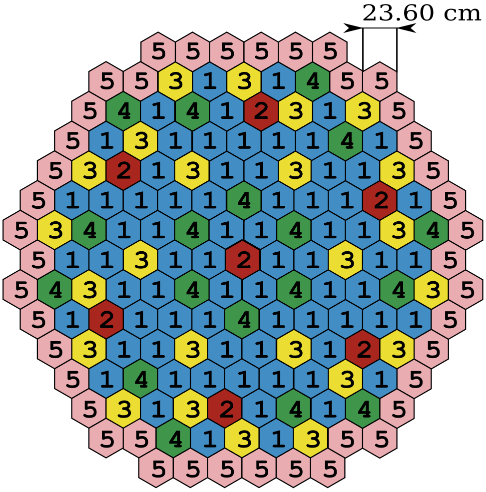

Figure 2.11: Geometry of the VVER-1000 reactor.

The results obtained for the fundamental eigenvalue k_{eff} using different polynomial degrees for the finite element method are shown in Table 2.13. In this Table also the degree of freedom (DoF) for the reduced ordinary eigenvalue problem and the non-zero elements (NNZ) of the block matrices are shown.

In Table 2.14 the results obtained for the first three subcritical eigenvalues are presented using different polynomial degree.

Figure 2.12 shows the neutronic power distribution for each hexagon computed with a polynomial degree equal to 6 in the finite element expansion, together with the reference result [74] and the percentage of the relative error on each hexagon. Some cuts of the thermal flux distrbution for the first two modes of the 2D VVER-1000 reactor are shown in Figure 2.13.

Table 2.12: Nuclear cross sections definition for the VVER-1000 reactor.

Material	Group	$\mathbf{D_g}$ (*cm*)	$\boldsymbol{\Sigma_{ag}}$ (1/ *cm*)	$\boldsymbol{\Sigma_{12}}$ (1/ *cm*)	$\boldsymbol{\nu\Sigma_{fg}}$ (1/ *cm*)	$\boldsymbol{\Sigma_{fg}}$ (1/ *cm*)
1	1	1.383200	8.38590E-3	1.64977E-2	4.81619E-3	1.86139E-3
	2	0.386277	6.73049E-2		8.46154E-2	3.48111E-2
2	1	1.382990	1.15490E-2	1.47315E-2	4.66953E-3	1.81560E-3
	2	0.389403	8.10328E-2		8.52264E-2	3.50622E-2
3	1	1.395220	8.94410E-3	1.56219E-2	6.04889E-3	2.36371E-3
	2	0.386225	8.44801E-2		1.19428E-2	4.91322E-2
4	1	1.394460	1.19932E-2	1.40185E-2	5.91507E-3	2.31026E-3
	2	0.387723	9.89670E-2		1.20497E-2	4.95721E-2
5	1	1.395060	9.11600E-3	1.54981E-2	6.40256E-3	2.50773E-3
	2	0.384492	8.93878E-2		1.29281E-2	5.31856E-2

Table 2.13: Eigenvalue results and power distribution errors for the VVER-1000 reactor.

Degree of FE	($\mathbf{k_{eff}}$)	$\boldsymbol{\Delta}\mathbf{k_{eff}}$ (pcm)	$\varepsilon_{\max}$(%)	$\bar{\varepsilon}$ (%)	DoF	NNZ
1	1.00443	204	17.7	4.53	535	18148
2	1.00643	5.5	1.47	0.35	2047	126628
3	1.00645	3.48	0.37	0.08	4537	442804
4	1.00645	3.48	0.11	0.036	8005	1130980
PARCS	1.006341	14.3	0.66	0.25		
Reference	1.006485					

Table 2.14: First 3 subcritical eigenvalues for the VVER-1000 reactor.

Degree of FE	λ_2	λ_3	λ_4
1	0.992242	0.992242	0.969948
2	0.994776	0.994776	0.973690
3	0.994810	0.994810	0.973763
4	0.994807	0.994807	0.973765
5	0.994809	0.994809	0.973769
6	0.994809	0.994809	0.973770

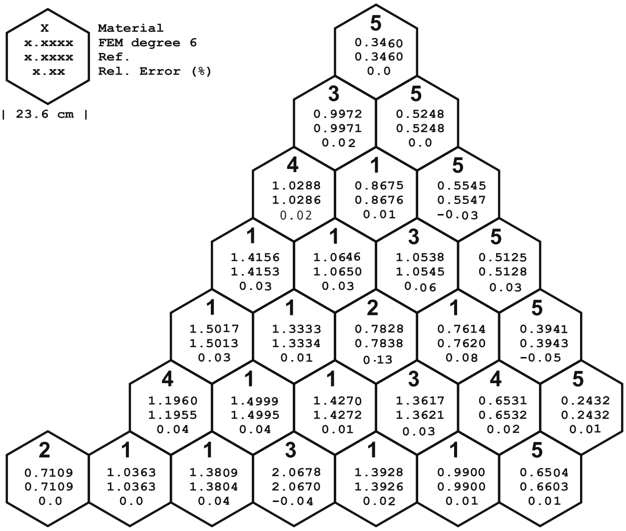

Figure 2.12: Power distribution for the VVER-1000 reactor with finite element degree $p = 6$.

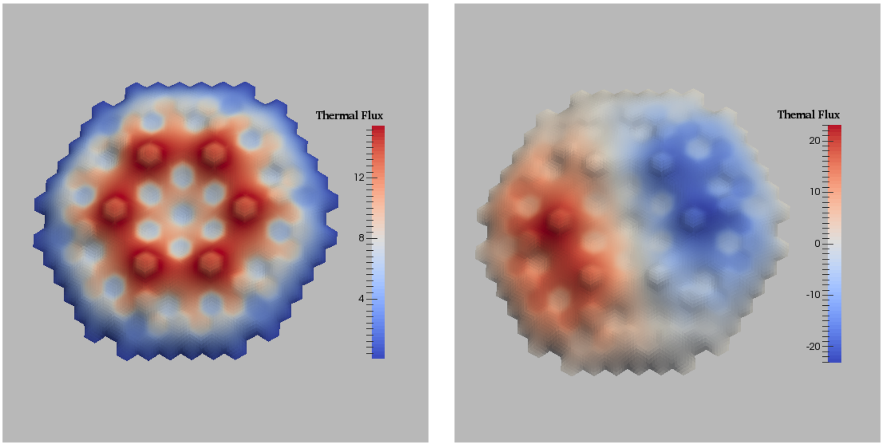

(a) Fundamental Mode **(b)** 1st Subcritcal Mode

Figure 2.13: Thermal Flux for the first modes.

2.3.6 Two-dimensional VVER-440 reactor

For this problem, the core is a VVER-440 core type, with 25 fuel elements across the diameter, as is shown in Figure 2.14. The core has 7 control rods inserted and a layer of reflector at the boundary of the core. The assembly pitch is 14.7 *cm*. Vacuum boundary conditions are considered at the external boundary of the reflector. Nuclear cross sections for this geometry are shown in Table 2.15 and the different results obtained for the critical eigenvalue k_{eff} of this reactor core are presented in Table 2.16.

Figure 2.15 shows the neutronic power distribution for each hexagon computed using a degree of polynomial $p = 6$ in the finite element expansion, together with the reference result [74] and the percentage of the relative error on each hexagon.

In Tables 2.16 and 2.17 the results obtained for the dominant and the first three subcritical eigenvalues, computed using different values of the polynomial degree (p) of the finite element approximation, are presented where we have just considered the decimal precision obtained from the reference result [74]. These Tables show that for $p = 5$ we already have a very accurate solution.

.

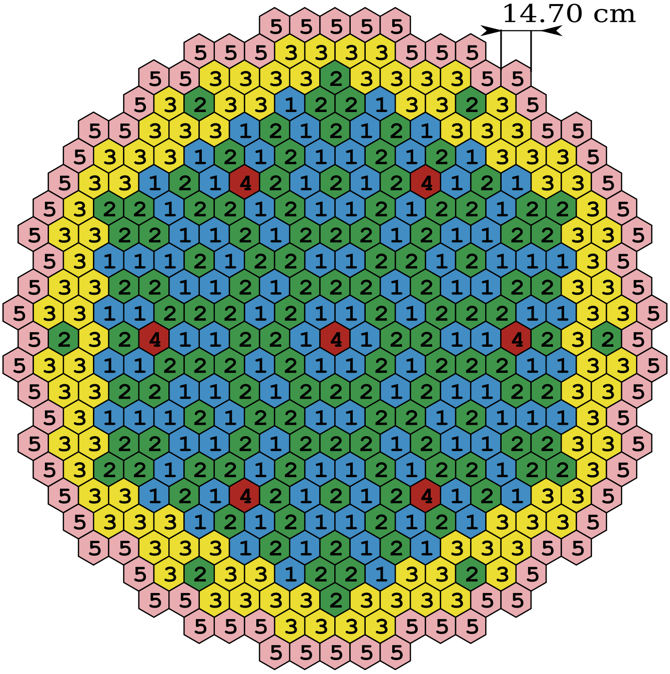

Figure 2.14: Geometry of the VVER-440 reactor.

Table 2.15: Nuclear cross sections definition for the the VVER-440 problem.

Fuel	**Group**	$\mathbf{D_g}$ (cm)	Σ_{ag} (1/ cm)	Σ_{12} (1/ cm)	$\nu\Sigma_{fg}$ (1/ cm)	Σ_{fg} (1/ cm)
1	1	1.34660	8.3620E-3	1.6893E-2	4.4488E-3	2.21676E-3
	2	0.37169	6.4277E-2		7.3753E-2	3.94368E-2
2	1	1.33770	8.7970E-3	1.5912E-2	5.5337E-3	2.792120E-3
	2	0.36918	7.9361E-2		1.0581E-1	5.657200E-2
3	1	1.33220	9.46200E-3	1.4888E-2	7.0391E-3	3.590680E-3
	2	0.36502	1.00100E-1		1.4964E-1	8.000000E-2
4	1	1.19530	1.33720E-2	2.2264E-2	0.0	0.0
	2	0.19313	1.34980E-1		0.0	0.0
5	1	1.44850	9.2200E-4	3.2262E-2	0.0	0.0
	2	0.25176	3.2839E-2		0.0	0.0

Table 2.16: Critical eigenvalue results and power distribution errors for the VVER-440 problem.

Degree of FE	($\mathbf{k_{eff}}$)	$\mathbf{\Delta k_{eff}}$ (**pcm**)	$\varepsilon_{\max}$(%)	$\bar{\varepsilon}$ (%)	**DoF**	**NNZ**
1	1.01222	249	11.48	6	1339	46372
2	1.01021	50.5	1.68	0.9	5203	325732
3	1.00975	4.95	0.217	0.08	11593	1141204
4	1.00971	0.99	0.22	0.08	20509	2917156
5	1.00971	0.99	0.22	0.08	45919	6199204
PARCS	1.009703	-0.28	0.31	0.14		
Reference	1.00970					

Table 2.17: First 3 subcritical eigenvalues for the VVER-440 reactor.

Degree of FE	λ_2	λ_3	λ_4
1	1.00585	1.00576	0.992453
2	1.00327	1.00327	0.989582
3	1.00271	1.00271	0.988961
4	1.00266	1.00266	0.988899
5	1.00265	1.00265	0.988896

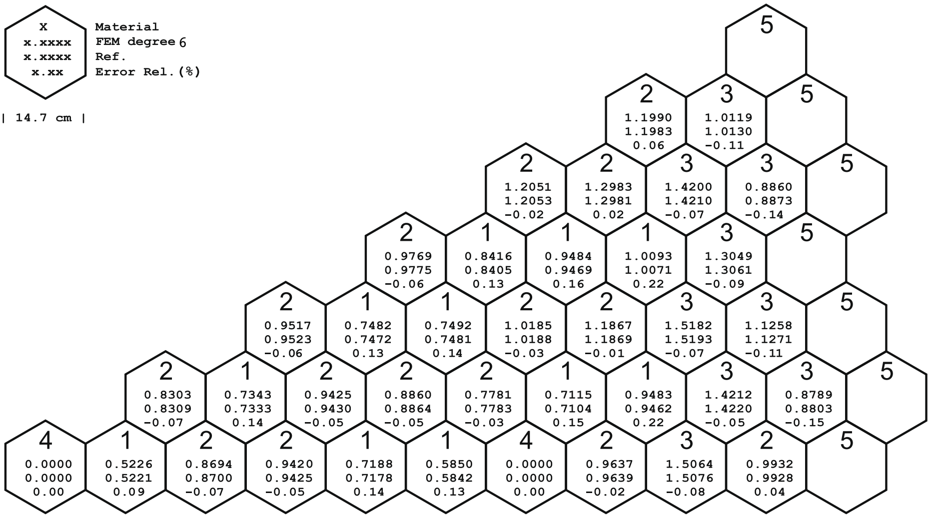

Figure 2.15: Power distribution for the VVER-440 Reactor with finite element degree $p = 6$.

2.3.7 Two-dimensional HWR reactor

This core is a very large HWR core of 35 assemblies across the core diameter, as it is shown in Figure 2.16.The fuel assemblies are surrounded by a tritium-generating target zone outside of which is the reflector zone. There are many rodded assemblies an some vacancy assemblies. The assembly pitch is 17.78 *cm*. The boundary conditions considered for this core are zero flux at the outside boundary of the reflector. Table 2.18 shows the nuclear cross sections data for the HWR core.

Table 2.19 shows the different results obtained for the the critical eigenvalue k_{eff} of this reactor core, we can note that the results obtained for polynomial degree $p = 3$ or polynomial degree $p = 4$ are already quite accurate.

Figure 2.17 shows the neutronic power distribution for each hexagon computed using a polynomial degree $p = 5$ in the finite element expansion, together with the reference result [74] and the percentage of relative error on each hexagon.

In Table 2.20 the results obtained for the first three subcritical eigenvalues, computed using different values of the polynomial degree (p) of the finite element approximation, are presented.

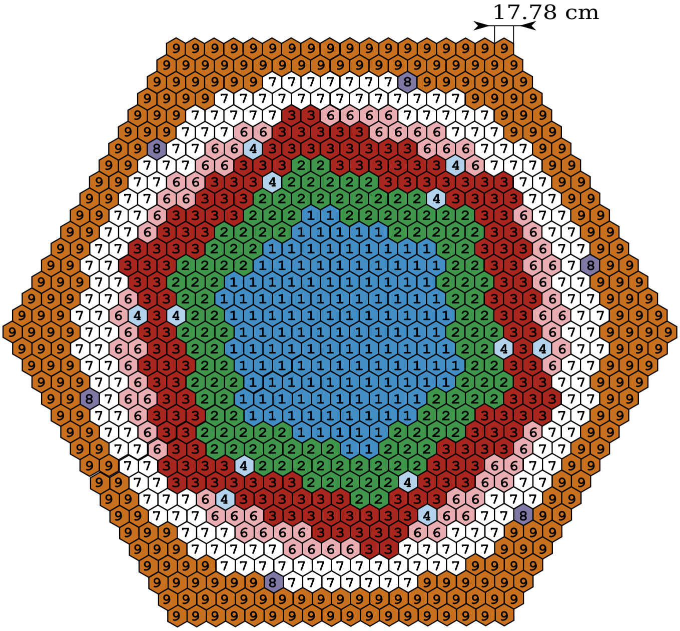

Figure 2.16: Geometry of the HWR reactor.

Table 2.18: Nuclear cross sections definition for the the HWR problem.

Material	**Group**	$\mathbf{D_g}$ (*cm*)	$\boldsymbol{\Sigma_{ag}}$ (1/ *cm*)	$\boldsymbol{\Sigma_{12}}$ (1/ *cm*)	$\boldsymbol{\nu\Sigma_{fg}}$ (1/ *cm*)	$\boldsymbol{\Sigma_{fg}}$ (1/ *cm*)
1	1	1.38250058	2.9412350E-3	8.16457E-3	2.26216E-3	9.30113E-4
	2	0.89752185	2.2306487E-2		2.30623E-2	9.51810E-3
2	1	1.38255219	2.9508050E-3	8.22378E-3	2.22750E-3	9.15899E-4
	2	0.89749043	2.2387609E-2		2.26849E-2	9.36233E-3
3	1	1.37441741	2.5322079E-3	8.08816E-3	2.14281E-3	8.80841E-4
	2	0.88836771	1.6946527E-2		2.04887E-2	8.45594E-3
4	1	1.31197955	3.7645300E-4	1.23115E-2	0.0	0.0
	2	0.87991376	5.2900925E-4		0.0	0.0
6	1	1.38138909	2.7974400E-3	7.76568E-3	2.39469E-3	9.84814E-4
	2	0.90367052	2.1902980E-2		2.66211E-2	1.09869E-2
7	1	1.30599110	6.3382099E-4	1.10975E-2	0.0	0.0
	2	0.83725587	4.3330365E-3		0.0	0.0
8	1	1.29192957	3.5711600E-4	1.15582E-2	0.0	0.0
	2	0.81934103	3.0056488E-4		0.0	0.0
9	1	1.06509884	2.1482210E-3	2.61980E-2	0.0	0.0
	2	0.32282849	3.3348874E-2		0.0	0.0

Table 2.19: Eigenvalue results and power distribution errors for the HWR problem.

Degree of FE	($\mathbf{k_{eff}}$)	$\mathbf{\Delta k_{eff}}$ (**pcm**)	$\varepsilon_{\max}(\%)$	$\bar{\varepsilon}$ (%)	**DoF**	**NNZ**
1	0.992094	13	5.16	0.89	2863	100516
2	0.991976	1.1	0.6	0.32	11239	709156
3	0.99196	0.5	0.52	0.31	25129	2487604
4	0.99196	0.5	0.52	0.30	44533	6362212
5	0.99194	2.5	0.52	0.31	69451	13524004
PARCS	0.991989	2.4				
Reference	0.991965					

Table 2.20: First 3 subcritical eigenvalues for the HWR reactor.

Degree of FE	λ_2	λ_3	λ_4
1	0.983730	0.983698	0.964245
2	0.983610	0.983610	0.964258
3	0.983591	0.983591	0.964236
4	0.983591	0.983591	0.964235
5	0.983591	0.983591	0.964236

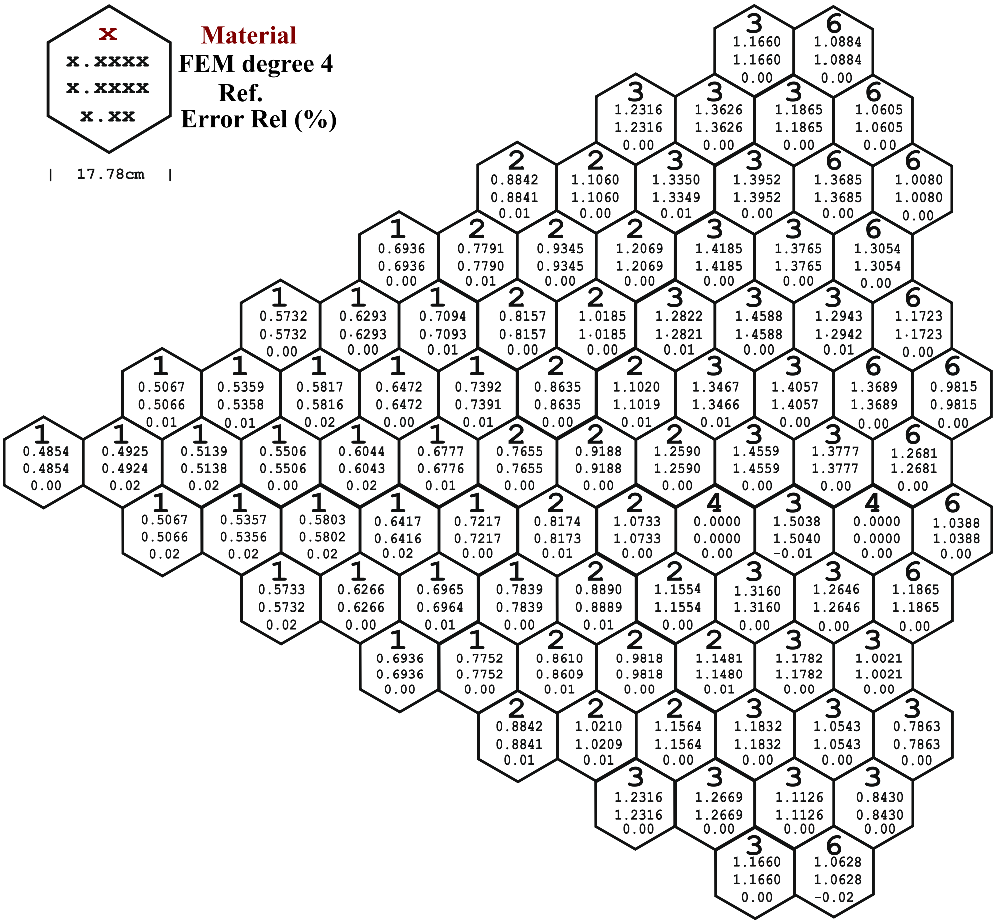

Figure 2.17: Power distribution for the HWR Reactor with finite element degree $p = 5$.

2.3.8 Three-dimensional VVER-440 reactor

The 3D VVER-440 problem with reflector is a 3D reactor of 250 *cm* height, with two reflector layers of 25.0 *cm* each added, one to the top and the other one to the bottom of the core. This problem is based on the same core for problem presented in subsection (2.3.6). The original two-dimensional core is extended to a three-dimensional core. The core is a VVER-440 type with 25 fuel elements along the diameter, with 7 control rods half-way inserted from the top, and another reflector layer added to the radial boundary of the core, as it is shown in Figure 2.18.

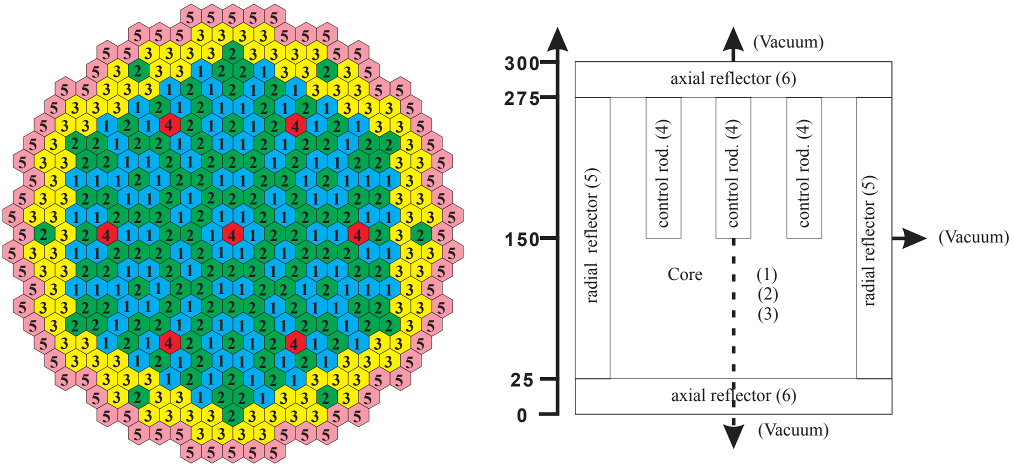

Figure 2.18: Geometry of the 3D VVER-440 problem with reflector.

This core has a radial symmetry by reflection of 1/12 and the pitch is 14.7 *cm*. Nevertheless, the calculations have been performed taking into account the whole core since the subcritical modes do not maintain the radial symmetry. Vacuum boundary conditions have been considered. Table 2.21 assigns the material types to assembly types and lists the cross sections in two energy groups. Materials 1, 2, 3 are fuel, material 4 is control rod. The control rod followers are of material 2. Materials 5, 6 are reflectors.

Table 2.22 shows the different results obtained for the fundamental eigenvalue k_{eff} of this reactor core. The reference results are reported in [93]. Table 2.24 summarizes the local results for the normalized power distribution for the best approximation, i.e., the one obtained with polynomial degree $p = 4$.

Figure 2.19 shows numbers identifying the position of the cells of the 3D VVER-440 reactor for the local power distribution.

Table 2.21: Nuclear cross sections definition for the the VVER-440 problem.

Material	Group	$\mathbf{D_g}$ (cm)	$\boldsymbol{\Sigma_{ag}}$ (1/ cm)	$\boldsymbol{\Sigma_{12}}$ (1/ cm)	$\boldsymbol{\nu\Sigma_{fg}}$ (1/ cm)	$\boldsymbol{\Sigma_{fg}}$ (1/ cm)
1	1	1.34660	8.3620E-3	1.6893E-2	4.4488E-3	2.21676E-3
	2	0.37169	6.4277E-2		7.3753E-2	3.94368E-2
2	1	1.33770	8.7970E-3	1.5912E-2	5.5337E-3	2.792120E-3
	2	0.36918	7.9361E-2		1.0581E-1	5.657200E-2
3	1	1.33220	9.46200E-3	1.4888E-2	7.0391E-3	3.590680E-3
	2	0.36502	1.00100E-1		1.4964E-1	8.000000E-2
4	1	1.19530	1.33720E-2	2.2264E-2	0.0	0.0
	2	0.19313	1.34980E-1		0.0	0.0
5	1	1.44850	9.2200E-4	3.2262E-2	0.0	0.0
	2	0.25176	3.2839E-2		0.0	0.0
6	1	1.34130	2.1530E-3	2.7148E-2	0.0	0.0
	2	0.24871	6.4655E-2		0.0	0.0

Table 2.22: Fundamental eigenvalue results and power distribution errors for the 3D VVER-440 problem.

Degree of FE	($\mathbf{k_{eff}}$)	$\mathbf{\Delta k_{eff}}$ (**pcm**)	$\varepsilon_{\max}$(%)	$\bar{\varepsilon}$ (%)	**DoF**
1	1.01372	236	11	5	17407
2	1.01177	44	1.5	0.8	130075
3	1.01138	5.4	0.17	0.06	428941
4	1.0113209	0.09	0.22	0.09	1004941
PARCS	1.0113630	3.75	1.44	0.98	
Reference	1.0113250				

Figure 2.20 shows the axial averaged neutronic power distribution computed with a polynomial expansion degree equal of 4, together with the reference result [74] and the percentage of the relative error on each hexagon. Some cuts of the thermal flux distrbution for the three first modes of 3D VVER-440 reactor are shown in Figure 2.21.

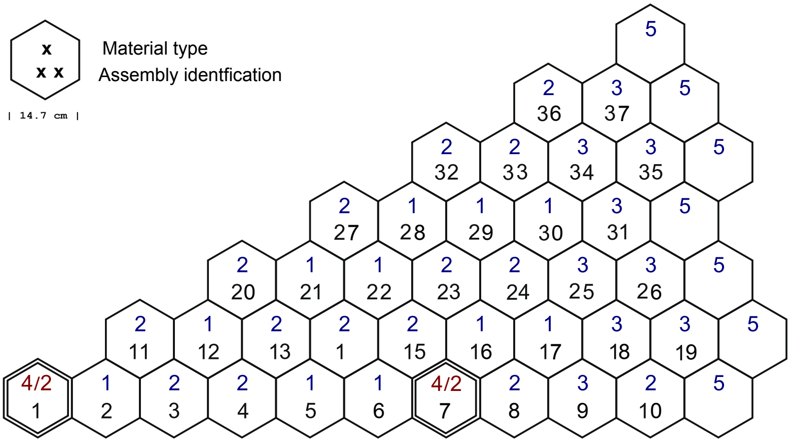

Figure 2.19: VVER-440 type three-dimensional core configuration.

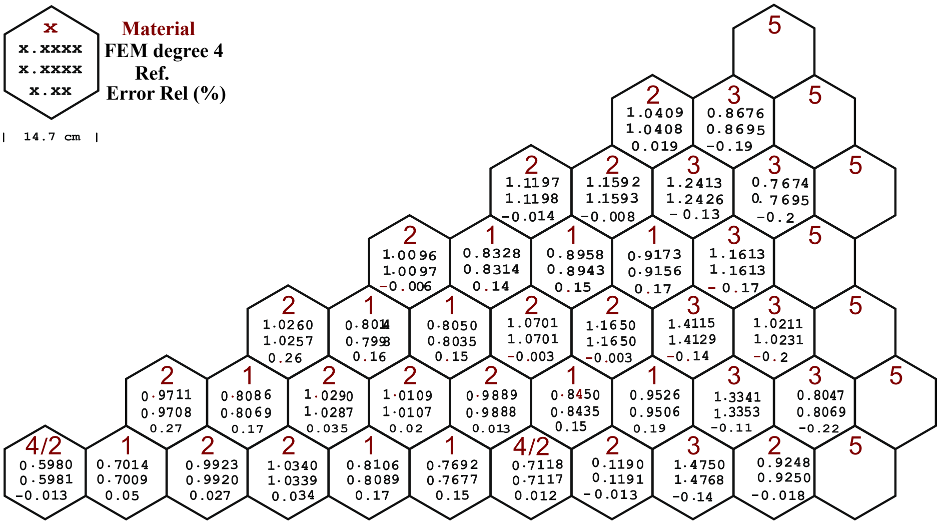

Figure 2.20: Power distribution for an average plane of 3D VVER-440 Reactor with finite element degree $p = 4$.

Table 2.23: First 3 subcritical eigenvalues for the 3D VVER-440 reactor.

Degree of FE	λ_2	λ_3	λ_4
1	1.00586	1.00574	0.990836
2	1.00334	1.00334	0.988095
3	1.00285	1.00285	0.987519
4	1.00278	1.00278	0.987443

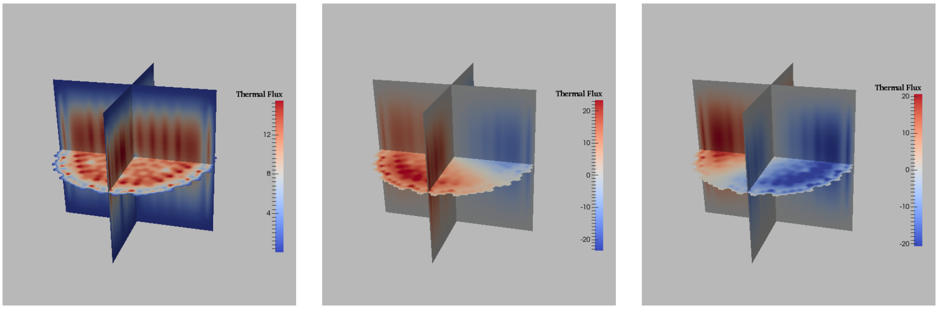

(a) Fundamental Mode **(b)** 1st Subcritcal Mode **(c)** 2nd Subcritcal Mode

Figure 2.21: Thermal Flux for the first 3 modes of the 3D VVER-440 reactor.

Table 2.24: Local power distribution for the 3D VVER-440 reactor.

$\mathbf{k}_{\text{eff}} = 1.011309, \quad P_{max} = 2.453$

	Axial plane									
Hex	**2**	**3**	**4**	**5**	**6**	**7**	**8**	**9**	**10**	**11**
1	0.5214	1.0755	1.4558	1.5852	1.3419	0	0	0	0	0
2	0.4208	0.8694	1.1773	1.2852	1.1427	0.7938	0.5671	0.3985	0.2489	0.1103
3	0.5511	1.1374	1.5414	1.6898	1.5625	1.2507	0.9347	0.6598	0.4125	0.1828
4	0.5642	1.1648	1.5796	1.7350	1.6201	1.3262	1.0023	0.7093	0.4441	0.1969
5	0.4506	0.9319	1.2644	1.3870	1.2789	1.0161	0.7572	0.5356	0.3358	0.1489
6	0.4632	0.9586	1.3015	1.4238	1.2597	0.8571	0.6084	0.4298	0.2702	0.1202
7	0.6151	1.2723	1.7297	1.8933	1.6077	0	0	0	0	0
8	0.6492	1.3442	1.8308	2.0164	1.8155	1.2883	0.9440	0.6784	0.4305	0.1925
9	0.7840	1.6217	2.2125	2.4531	2.3083	1.8938	1.4566	1.0539	0.6700	0.2998
10	0.4761	0.9869	1.3477	1.5002	1.4353	1.2177	0.9536	0.6928	0.4409	0.1969
11	0.5462	1.1270	1.5270	1.6723	1.5357	1.2070	0.8951	0.6310	0.3945	0.1748
12	0.4407	0.9110	1.2352	1.3566	1.2668	1.0369	0.7837	0.5545	0.3470	0.1536
13	0.5616	1.1596	1.5732	1.7287	1.6128	1.3171	0.9949	0.7049	0.4418	0.1960
14	0.5688	1.1753	1.5955	1.7501	1.6023	1.2473	0.9228	0.6536	0.4107	0.1825
15	0.5911	1.2222	1.6609	1.8204	1.6167	1.1082	0.7929	0.5632	0.3552	0.1585
16	0.4935	1.0229	1.3926	1.5319	1.3740	0.9655	0.7032	0.5041	0.3195	0.1426
17	0.5119	1.0619	1.4484	1.6037	1.4976	1.2060	0.9202	0.6649	0.4226	0.1885
18	0.6914	1.4304	1.9532	2.1729	2.0730	1.7491	1.3659	0.9919	0.6313	0.2825
19	0.4103	0.8498	1.1611	1.2949	1.2458	1.0671	0.8410	0.6123	0.3899	0.1744
20	0.5556	1.1472	1.5565	1.7117	1.6044	1.3227	1.0045	0.7124	0.4466	0.1981
21	0.4349	0.8996	1.2215	1.3438	1.2555	1.0269	0.7778	0.5528	0.3473	0.1541
22	0.4416	0.9141	1.2427	1.3679	1.2675	1.0142	0.7626	0.5439	0.3429	0.1525
23	0.5861	1.2127	1.6513	1.8223	1.6881	1.3396	1.0105	0.7256	0.4596	0.2051
24	0.6176	1.2792	1.7451	1.9353	1.8224	1.4968	1.1524	0.8340	0.5301	0.2368
25	0.7269	1.5041	2.0547	2.2888	2.1906	1.8575	1.4562	1.0595	0.6747	0.3020
26	0.5178	1.0724	1.4659	1.6370	1.5793	1.3581	1.0740	0.7835	0.4994	0.2234
27	0.5422	1.1207	1.5239	1.6810	1.5783	1.3010	0.9928	0.7097	0.4476	0.1992
28	0.4394	0.9103	1.2403	1.3735	1.2987	1.0811	0.8339	0.6007	0.3805	0.1695
29	0.4626	0.9596	1.3100	1.4574	1.3917	1.1762	0.9193	0.6673	0.4244	0.1893
30	0.4641	0.9635	1.3174	1.4715	1.4194	1.2193	0.9645	0.7041	0.4488	0.2003
31	0.5820	1.2054	1.6493	1.8466	1.7922	1.5547	1.2383	0.9066	0.5786	0.2590
32	0.5728	1.1864	1.6202	1.8054	1.7346	1.4825	1.1663	0.8481	0.5395	0.2410
33	0.5804	1.2033	1.6464	1.8431	1.7891	1.5526	1.2367	0.9051	0.5774	0.2581
34	0.6151	1.2738	1.7446	1.9582	1.9116	1.6725	1.3410	0.9849	0.6293	0.2820
35	0.3780	0.7836	1.0736	1.2065	1.1808	1.0368	0.8337	0.6132	0.3921	0.1756
36	0.5127	1.0637	1.4574	1.6374	1.6020	1.4061	1.1303	0.8312	0.5313	0.2377
37	0.4247	0.8803	1.2069	1.3583	1.3335	1.1760	0.9491	0.6994	0.4476	0.2005

Table 2.25: Local power distribution CRONOS recommended solution for the 3D VVER-440 reactor.

$\mathbf{k}_{\text{eff}}$=1.011325, $P_{max} = 2.456$

Axial plane										
Hex	**2**	**3**	**4**	**5**	**6**	**7**	**8**	**9**	**10**	**11**
1	0.520	1.075	1.456	1.586	1.344	0	0	0	0	0
2	0.419	0.867	1.175	1.283	1.141	0.793	0.566	0.398	0.248	0.110
3	0.550	1.136	1.541	1.690	1.563	1.251	0.935	0.660	0.412	0.182
4	0.563	1.164	1.579	1.735	1.620	1.326	1.002	0.709	0.444	0.196
5	0.449	0.929	1.262	1.384	1.277	1.014	0.756	0.535	0.335	0.148
6	0.461	0.956	1.299	1.421	1.258	0.856	0.608	0.429	0.270	0.120
7	0.613	1.271	1.729	1.894	1.610	0	0	0	0	0
8	0.647	1.343	1.831	2.017	1.817	1.289	0.945	0.679	0.431	0.192
9	0.782	1.622	2.215	2.456	2.312	1.897	1.459	1.056	0.671	0.299
10	0.475	0.986	1.348	1.501	1.436	1.219	0.954	0.693	0.441	0.197
11	0.545	1.126	1.527	1.672	1.536	1.207	0.895	0.631	0.394	0.174
12	0.439	0.908	1.232	1.354	1.265	1.035	0.782	0.554	0.346	0.153
13	0.560	1.159	1.573	1.728	1.613	1.317	0.995	0.705	0.442	0.196
14	0.567	1.174	1.595	1.750	1.603	1.248	0.923	0.654	0.411	0.182
15	0.589	1.221	1.660	1.820	1.617	1.109	0.793	0.563	0.355	0.158
16	0.491	1.020	1.390	1.529	1.372	0.965	0.702	0.504	0.319	0.142
17	0.509	1.059	1.445	1.601	1.495	1.204	0.919	0.664	0.422	0.188
18	0.689	1.431	1.955	2.175	2.076	1.752	1.368	0.993	0.632	0.282
29	0.410	0.852	1.164	1.299	1.250	1.071	0.844	0.614	0.391	0.174
20	0.554	1.146	1.556	1.712	1.605	1.323	1.005	0.713	0.446	0.198
21	0.433	0.897	1.219	1.341	1.253	1.025	0.777	0.552	0.347	0.154
22	0.440	0.912	1.240	1.366	1.266	1.013	0.762	0.543	0.342	0.152
23	0.584	1.212	1.651	1.823	1.689	1.340	1.011	0.726	0.460	0.205
24	0.616	1.278	1.745	1.936	1.823	1.498	1.153	0.835	0.530	0.236
25	0.725	1.504	2.057	2.292	2.194	1.860	1.459	1.061	0.675	0.302
26	0.517	1.074	1.469	1.641	1.583	1.362	1.077	0.786	0.500	0.223
27	0.541	1.12	1.524	1.682	1.579	1.302	0.993	0.710	0.448	0.199
28	0.438	0.908	1.238	1.371	1.297	1.080	0.833	0.600	0.380	0.169
29	0.461	0.957	1.308	1.455	1.39	1.175	0.918	0.667	0.424	0.189
30	0.462	0.961	1.315	1.469	1.417	1.218	0.963	0.703	0.448	0.200
31	0.581	1.206	1.652	1.850	1.796	1.558	1.241	0.908	0.579	0.259
32	0.571	1.186	1.620	1.806	1.736	1.484	1.167	0.849	0.54	0.241
33	0.579	1.202	1.646	1.844	1.790	1.554	1.238	0.906	0.577	0.258
34	0.614	1.274	1.746	1.961	1.915	1.675	1.343	0.987	0.63	0.282
35	0.378	0.785	1.077	1.210	1.185	1.040	0.837	0.615	0.393	0.176
36	0.511	1.063	1.457	1.637	1.602	1.407	1.131	0.831	0.531	0.237
37	0.424	0.882	1.209	1.362	1.337	1.179	0.952	0.701	0.449	0.200

Table 2.26: Distribution difference (%) of the FEM solution to CRONOS recommended solution for the 3D VVER-440 reactor.

$\Delta\ \mathbf{k}_{\text{eff}} = 0.4\, pcm, \quad \Delta\ P_{max} = 0.003$

	Axial plane									
Hex	**2**	**3**	**4**	**5**	**6**	**7**	**8**	**9**	**10**	**11**
1	-0.14	-0.05	0.02	0.08	0.21	0	0	0	0	0
2	-0.18	-0.24	-0.23	-0.22	-0.17	-0.08	-0.11	-0.05	-0.09	-0.03
3	-0.11	-0.14	-0.04	0.02	0.05	0.03	0.03	0.02	-0.05	-0.08
4	-0.12	-0.08	-0.06	0	-0.01	-0.02	-0.03	-0.03	-0.01	-0.09
5	-0.16	-0.29	-0.24	-0.3	-0.19	-0.21	-0.12	-0.06	-0.08	-0.09
6	-0.22	-0.26	-0.25	-0.28	-0.17	-0.11	-0.04	-0.08	-0.02	-0.02
7	-0.21	-0.14	-0.07	0.07	0.23	0	0	0	0	0
8	-0.22	-0.12	0.02	0.06	0.15	0.07	0.1	0.06	0.05	-0.05
9	-0.20	0.030	0.25	0.29	0.37	0.32	0.24	0.21	0.1	-0.08
10	-0.11	-0.09	0.03	0.08	0.07	0.13	0.04	0.02	0.01	0.01
11	-0.12	-0.11	0	-0.03	0.03	0	-0.01	0	-0.05	-0.08
12	-0.17	-0.3	-0.32	-0.26	-0.18	-0.19	-0.17	-0.05	-0.1	-0.06
13	-0.16	-0.06	-0.02	-0.07	0.02	-0.01	0.01	0.01	0.02	0
14	-0.18	-0.13	-0.05	-0.01	0.07	0.07	0.02	0.04	0.04	-0.05
15	-0.21	-0.12	-0.09	-0.04	0.03	0.08	0.01	-0.02	-0.02	-0.05
16	-0.26	-0.29	-0.26	-0.3	-0.2	-0.05	-0.12	-0.01	-0.05	-0.06
17	-0.29	-0.29	-0.34	-0.27	-0.26	-0.2	-0.12	-0.09	-0.06	-0.05
18	-0.24	0.06	0.18	0.21	0.3	0.29	0.21	0.11	0.07	-0.05
19	-0.03	0.22	0.29	0.41	0.42	0.39	0.3	0.17	0.11	-0.04
20	-0.16	-0.12	-0.05	0.03	0.06	0.03	0.05	0.06	-0.06	-0.01
21	-0.19	-0.26	-0.25	-0.28	-0.25	-0.19	-0.08	-0.08	-0.03	-0.01
22	-0.16	-0.21	-0.27	-0.19	-0.15	-0.12	-0.06	-0.09	-0.1	-0.05
23	-0.21	-0.07	-0.03	0.07	0.09	0.04	0.05	0.04	0.04	-0.01
24	-0.16	-0.12	-0.01	0.07	0.06	0.12	0.06	0.1	-0.01	-0.08
25	-0.19	-0.01	0.23	0.32	0.34	0.25	0.28	0.15	0.03	0
26	-0.08	0.16	0.3	0.4	0.37	0.39	0.3	0.25	0.06	-0.04
27	-0.12	-0.07	0.01	0.1	0.07	0.1	0.02	0.03	0.04	-0.02
28	-0.14	-0.23	-0.23	-0.25	-0.17	-0.11	-0.09	-0.07	-0.05	-0.05
29	-0.16	-0.26	-0.2	-0.24	-0.17	-0.12	-0.13	-0.03	-0.04	-0.03
30	-0.21	-0.25	-0.24	-0.25	-0.24	-0.14	-0.15	-0.11	-0.08	-0.03
31	-0.10	0.06	0.27	0.34	0.38	0.33	0.27	0.14	0.04	0
32	-0.18	-0.04	-0.02	0.06	0.14	0.15	0.07	0.09	0.05	0
33	-0.14	-0.13	-0.04	0.09	0.09	0.14	0.13	0.09	-0.04	-0.01
34	-0.11	0.02	0.14	0.28	0.34	0.25	0.2	0.21	0.07	0
35	0	0.14	0.33	0.35	0.42	0.32	0.33	0.18	0.09	0.04
36	-0.18	-0.07	-0.04	-0.04	0	0.09	0.07	-0.02	-0.03	-0.07
37	-0.07	0.17	0.21	0.37	0.35	0.3	0.3	0.16	0.14	-0.05

Chapter 3

Time Dependent Neutron Diffusion Equation

To simulate the behaviour of a nuclear power reactor it is necessary to be able to integrate the time dependent neutron diffusion equation inside the reactor core. In particular, we will consider here VVER-type reactors which use the neutron diffusion equation discretized on hexagonal meshes. For a given transient, the balance of neutrons inside a nuclear reactor core can be modelled using the time dependent neutron diffusion equation in the two energy groups approximation [94]. This equation as defined before in Chapter 1 (equation 1.36) can be expressed in the following form

$$
\begin{aligned}
[\mathrm{v}^{-1}]\frac{\partial \phi}{\partial t} + \mathcal{L}\phi &= (1-\beta\ )\mathcal{M}\phi + \sum_{k=1}^{K}\lambda_k \chi \mathcal{C}_k \quad , \\
\frac{\partial \mathcal{C}_k}{\partial t} &= \beta_k[\nu\Sigma_{f1}\ \nu\Sigma_{f2}]\phi - \lambda_k \mathcal{C}_k \quad , \quad k=1,\dots,K \quad ,
\end{aligned}
$$

where K is the number of delayed neutron precursors groups considered and the $\mathcal{L}$, $\mathcal{M}$ operators are known as the neutron loss operator and the neutron production operator. β_k is the yield of delayed neutrons in the k-th precursors group, χ is the fission neutron spectrum and λ_k is the corresponding decay constant. Both coefficients are related to the delayed neutron precursor decay.

Different methods have been proposed for the time discretization of the time dependent neutron diffusion equation [95]. Standard methods use backward difference formulas [96]. In these methods the reactor is divided in cells or nodes and a spatial discretization of the equations is applied. These methods for each time step need to solve a system of linear equations, where the matrices involved are large and sparse. Usually, these systems are solved using iterative methods such as the Krylov subspace methods. The converge rate of these methods can largely be improved if a suitable preconditioner is used [97]. Usual preconditioners are based on incomplete factorizations of the system matrix, but this approach is expensive in terms of the computational time and memory for the storage of the matrix. The convergence of the Krylov methods generally depends on the eigenvalues and eigenvectors of the coefficients matrices. When some estimations of eigenvectors and eigenvalues are available, low rank transformations can be applied to improve the convergence rate of the iterative method. This technique is known as spectral preconditioning of linear systems [98]. For a given transient, a number of systems have to be solved whose matrices varies continuously in time, and for successive time steps the coefficients matrices are expected to have similar eigenvalues and eigenvectors. Thus, the information obtained from the Krylov subspace when solving a system can be used to precondition the system corresponding to the next time step. In [99] Different spectral preconditioners based on different Krylov methods such as GMRES-DR [86] were studied using a typical transient in a nuclear power reactor with hexagonal geometry.

Other kind of methods such as modal methods [70] or the quasi-static method [100] have been also studied. An efficient solution method was presented to solve the time dependent multi-group diffusion equations for subcritical systems with external sources using a rigorous weight function in the quasi-static method [101]. However, the method is developed for systems which are close to criticality. In this method, the space and time dependent flux is expressed as the product of the amplitude function which changes quickly with time and the shape function which changes slowly with time. A one-point kinetics equation is derived for the amplitude function by multiplying an appropriate weight function to the time dependent group diffusion equation, and integrating it over the whole phase space. The advantage of this method is that a longer time step can be used to calculate the shape function by using a short time step to calculate the amplitude function which is much easier to solve, and a solution can be obtained by using short time steps.

Some transient calculations in reactor cores are based on dynamic changes in the reactor configuration due to the movement of control rods, which are usual manoeuvres in the reactor operation. The simulation of these transients presents what is known as the *rod-cusping* problem.

3.1 Rod cusping

The rod cusping is a unphysical behaviour of different magnitudes as the power and the k-effective of the reactor that appears in the calculation along the transient. This problem is caused by the use of fixed mesh schemes and when the volume weighted method is used to interpolate the cross sections properties for the partially rodded node (PRN) by means of the portion of the rod inserted on the node as Figure 3.1 represents.

Let us suppose a partially rodded node (P) adjacent to a fully rodded node (R) and to an unrodded node (U). When a control rod is partially inserted in a node, this partially rodded node (P) node is divided into two parts: the upper part of the node or the rodded (PR), where the cross sections are modified due to the effect of the control rod, and the lower part of the node or the unrodded node (PU), which has the cross sections without modifications. Then, the cross sections of the whole node are calculated by means of an interpolation procedure taking into account the position of the control rod tip.

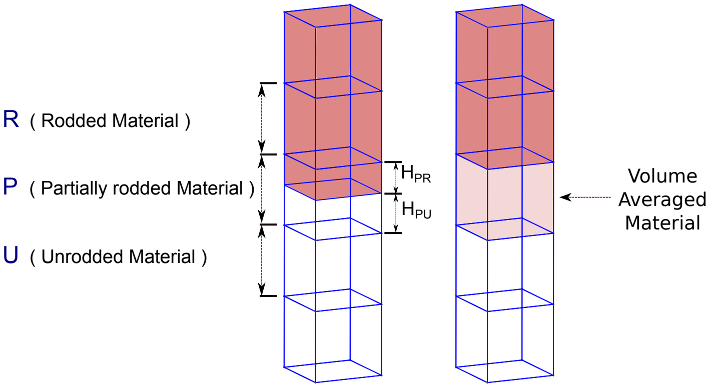

Figure 3.1: Rod-cusping problem in a fixed mesh scheme.

For example, Figure 3.2a shows the evolution of the k_{eff} along a given transient presenting the rod cusping problem while the other Figure (Figure 3.2b) shows the evolution of the k_{eff} in the first 0.07 s. As can be seen in Figure 3.2, for the curve obtained by PARCS code using 12 planes, a discontinuity appears in the first derivative, at each boundary between two nodes. This unphysical behaviour is reduced by increasing the number of planes used in the calculations. The rod cusping effect can cause some problems in evaluating differential rod worth curves for control rods or in analyzing transients involving control rod movements. Also when reactivity is plotted versus assembly insertion distance, the approximation of volume weighted method for the motion of either a control rod or fuel assembly results in a reactivity curve with a series of cusps that fall in between positions

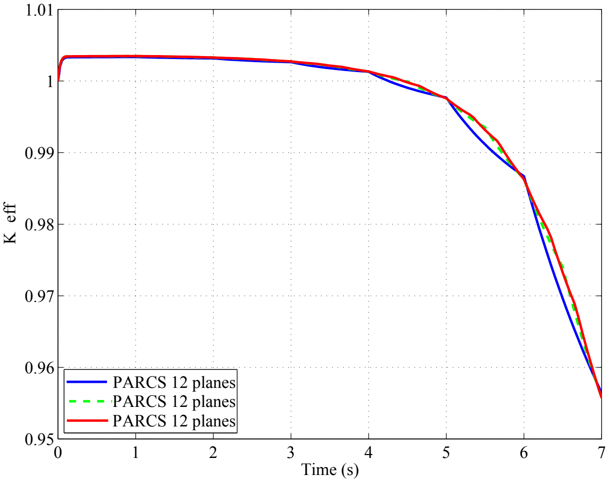

(a) Rod cusping effect along the transient

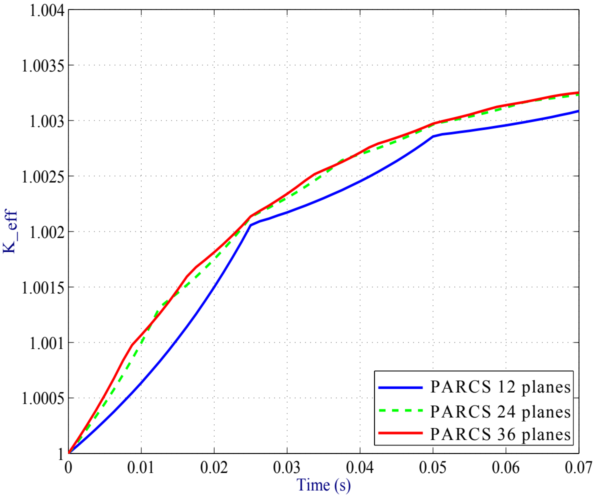

(b) Rod cusping effect in the first 0.07 sec.

Figure 3.2: Rod cusping effect.

where the assembly is aligned with the mesh. This variation of reactivity leads also to large errors in the predicted core power in addition to the errors for the eigenvalue calculation.

One possibility to resolve the rod cusping problem is to use a flux-weighted technique to obtain the cross-sections of a partially rodded node (PRN). It is necessary, first of all, to determine the axial flux profile within a PRN. The flux profile can be used to calculate flux volume weighted homogenized cross sections or axial discontinuity factors. Several sophisticated methods, based on a flux weighting technique, have been introduced. One of the first ones is the work of H. S. Joo in 1984 [1], his approximations were introduced in the determination of the axial flux profile. Interface displacement [102], quadratic flux representation and forward flux adjoint flux bilinear weighting method [103] are the examples of such approximations. Although the consequence of these approximations may not be significant in most practical calculations, they could cause unbearable errors in heavily rodded cases and transient calculations. Then he presented a new rod cusping correction method that uses fine mesh flux solutions obtained from two one-dimensional, three-node problems for each PRN. The heterogeneity within the PRN is explicitly kept and the flux-weighting factor is calculated from the resulting fine-mesh flux profile. The axial discontinuity factors are then generated with the homogenized cross section in the PRN for the subsequent nodal calculations.

Many other techniques exist for the treatment of the rod cusping problem. As, for example, a flux weighting method [104], [105], the bilinear weighting method, the equivalent-node method [104] and moving meshes method [106]. All of these methods provide satisfactory approximations for the motion of assemblies, with the exception of the volume weighting method [107]. Since no flux weighting is taken into account in the simple volume weighting method, extremely large errors are observed. We report them here in order to permit a comparison between the different approaches [106].

3.1.1 Approximate flux weighting method

This method has been proposed by J. C. Gehin [108] in 1992 to avoid discontinuities of the flux versus time behavior in kinetics transients involving control rod movements. He introduced a simple correction model. In absence of an average flux in the unrodded (NR) and rodded (R) fractions of the node he approximated them by the following relations:

$$\phi_{NR,g} = \frac{\Delta z_{k-1}\ \phi_{k-1,g} + (1 - f_{ins})\ \Delta z_k\ \phi_{k,g}}{\Delta z_{k-1} + (1 - f_{ins})\ \Delta z_k}$$

$$\phi_{R,g} = \frac{\Delta z_{k+1}\ \phi_{k+1,g} + f_{ins}\ \Delta z_k\ \phi_{k,g}}{\Delta z_{k+1} + f_{ins}\ \Delta z_k}$$

where $\phi_{k,g}$,g is the neutron flux in node k, Δz_k is the size of the node in the vertical z direction and f_{ins} is the fraction of insertion of the rod in the node. With these definitions, he computed the average cross sections of type X (X = absorption, neutron-production, removal from group 1 to 2) by the relation:

$$\bar{\Sigma}_{X,g} = \frac{(1 - f_{ins})\Sigma_{NR,X,g}\ \phi_{NR,g} + f_{ins}\ (\Sigma_{NR,X,g} + \Delta\Sigma_{X,g})\ \phi_{R,g}}{(1 - f_{ins})\ \phi_{NR,g} + f_{ins}\ \phi_{R,g}}. \tag{3.1}$$

3.1.2 Analytical flux weighting with axial discontinuity factors method

This method has been proposed by K. S. Smith et al. [109] in 1992. In this method, the two-group flux distribution in the vicinity of a control rod tip is computed by solving analytically a one-dimensional two-region problem (like the one shown in 3.3) using the neutron current resulting from the general nodal solution as boundary conditions. The intranodal flux shapes are integrated analytically over the volume of the node to obtain flux-volume-weighted cross sections. Additionally, the axial discontinuity factors for the top and bottom of the partially rodded node are computed by taking the ratios of the heterogeneous to homogeneous boundary fluxes (found by solving the two-group diffusion equations with flux-volume weighted cross sections and fixed current boundary conditions at the top and bottom of the node).

3.1.3 Bilinear weighting method

This method has been proposed by Y. H. Kim and N. Z. Cho [110], [103] in 1990. According to this method, for a partially rodded node, the equivalent homogenized cross sections of type X for group g are calculated by the relation:

$$\bar{\Sigma}_{X,g} = \frac{\int_0^{\Delta z_k} \phi_g \Sigma_{X,g}\ \phi_g^+ dz}{\int_0^{\Delta z_k} \phi_g\ \phi_g^+ dz} \tag{3.2}$$

and the equivalent homogenized diffusion coefficient is calculated by:

$$\bar{D_g} = \frac{\int_0^{\Delta z_k} \phi_g\ \phi_g^+ dz}{\int_0{}^{\Delta} z_k \phi_g \frac{1}{D_g}\ \phi_g^+ dz} \tag{3.3}$$

where the integration is performed over the node k, and ϕ_g and ϕ_g^+ are the heterogeneous forward and adjoint fluxes inside the node.

3.1.4 Equivalent node method

This method is based on the equivalence between two configurations. The former is a two-node configuration where the upper one is fully controlled by the rod tip. The total size of these two nodes is equal to the calculation mesh size Δz in the core model. The second is the calculation node where the tip of the rod is homogenized. A scheme of the node is shown in Figure 3.3

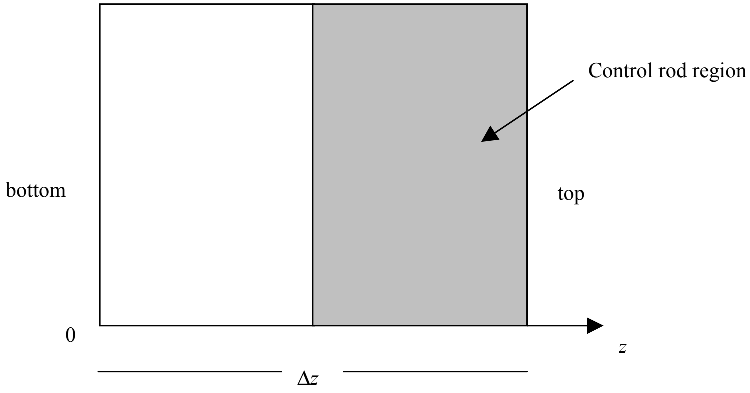

Figure 3.3: A node containing the tip of a control rod.

The purpose of the equivalence is to obtain parameters that will force the nodal flux calculation to give results close to the ones that would be obtained by splitting the rodded nodes into two regions. This is done by imposing that the average two-group neutron balance and its first and second moment, computed in the two configurations, be the same. From the condition of equality of the average two-group neutron balance we obtain the rod cross section weighting factors.

All these methods have to solve a small one-dimensional eigenvalue problem for each one of the partially rodded nodes. Then, different schemes are applied to obtain the new cross sections of the partially rodded node from the old cross sections of the two parts of the node (the rodded and the unrodded) and the heterogeneous flux for the small isolated problem with suitable boundary conditions. These solutions can be improved by means of the use of assembly discontinuity factors for the interface of the node with the ones on a neighbourhood. Also some approaches have been discussed to estimate the flux distribution inside the partially rodded node [107]. Other strategy is based on interpolating the solution on refined meshes near the moving control rod [111].

3.2 Moving mesh strategy

As mentioned before, to solve accurately these PDEs, it is often necessary to adapt the mesh to the specifics of the problem. Adaptive techniques are traditionally sorted into three categories:

- We can adapt the mesh by adding or removing grid points in certain parts of the domain; this is called h-adaptivity.
- Another technique, when using the finite-element method, is to vary the degree of the polynomial approximations; this is called p-adaptivity. Sometimes, h- and p-adaptivity are used together, forming a hybrid category called $h-p$-adaptivity.
- Lastly, the technique we focus on in this chapter consists of moving the initial grid points in order to reposition them in an optimal way; one can adapt based upon the geometry of the surface, or based upon the behaviour of the PDE solution.

Mesh adaptivity begun in the late 1970s [5] and is based on the idea that in order to achieve high accuracy, a uniformly fine mesh is not necessarily required; rather, the computational grid only needs to be fine in regions where the solution is rough and can be coarse in areas where the solution is smooth and, therefore, well resolved even on large cells. The challenge is that, in general, it is not known a priori where the solution will require the mesh to be fine. Consequently, the computation of local error or smoothness indicators from a numerical solution, previously obtained on a coarser mesh, lies at the heart of all adaptive mesh refinement algorithms, and a significant number of successful approaches have been developed for this problem in the last decade [7], [88].

Using these methods, it has been shown for many problems that the computational effort needed to reach a certain accuracy can often be reduced by one or several orders of magnitude compared to uniform meshes, frequently enabling the solution of entire new classes of problems that were previously considered too computationally expensive to solve the required accuracy. The use of adaptative meshes or the study of nuclear reactors has beeen recently proposed [8], [9], begining with the study of different error estimators for the mesh refinement for the computation of the k-effective of the reactor and the stationary power distirbution.

A moving mesh strategy is developed here [112] to reduce the rod-cusping problem. This method is based on the use of different spatial meshes for the different time steps following the movement of the control rod avoiding the necessity of the use of averaged material properties, as it is observed in Figure 3.4. To avoid the hanging nodes problem [113], the spatial mesh is moved in the same way for all the axial plane. The solutions obtained in each time step for the physical quantities are interpolated to a new spatial mesh in each time step.

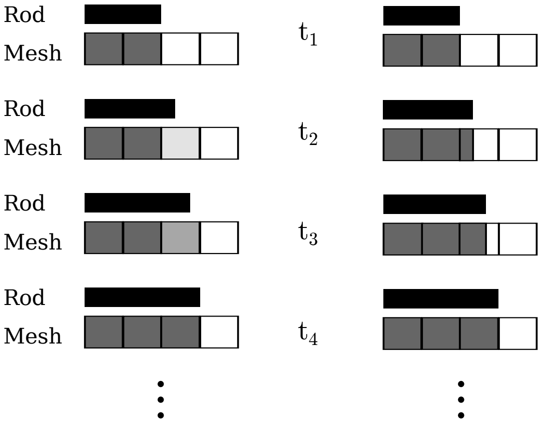

(a) Fixed Mesh (b) Moving mesh

Figure 3.4: 1D representation of fixed and moving mesh schemes.

3.3 Time discretization

Once the spatial discretization has been selected, a discrete version of the time dependent neutron diffusion equation is solved. Since the system of ordinary differential equations resulting from the discretization of the neutron diffusion equations is, in general stiff, implicit methods are necessary. Particularly, a first order backward method is used [96], needing this method to solve a large system of linear equations for each time step. The time discretization of the neutron diffusion equation is obtained as follows. After the spatial discretization is performed, the semi-discrete two energy groups time dependent neutron diffusion equation together with the neutron precursors concentration equations are of the form

$$[\tilde{\mathrm{v}}^{-1}]\frac{d\tilde{\phi}}{dt} + L\tilde{\phi} = (1-\beta\ )M\tilde{\phi} + \sum_{k=1}^{K} \lambda_k X C_k \ , \tag{3.4}$$

$$P\frac{dC_k}{dt} = \beta_k \left(M_{11} M_{21}\right) \tilde{\phi} - \lambda_k P C_k \ , \quad k = 1, \dots, K \ , \tag{3.5}$$

where L and M are the matrices obtained from the spatial discretization of operators $\mathcal{L}$ and $\mathcal{M}$, whose elements are given by equation (2.8) Matrix X and $[\tilde{\mathrm{v}}^{-1}]$ are defined as

$$X = \begin{pmatrix} P \\ 0 \end{pmatrix} , \qquad [\tilde{\mathrm{v}}^{-1}] = \begin{pmatrix} P\,\mathrm{v}_1^{-1} & 0 \\ 0 & P\,\mathrm{v}_2^{-1} \end{pmatrix} ,$$

where matrix P is the mass matrix of the spatial discretization, which appears due to the fact that the polynomial basis used in the spatial discretization is not orthogonal. The matrix elements of P are given by,

$$P_{ij} = \sum_{e=1}^{N_t} \int_{\Omega_e} N_{1i} N_{1j} \mathrm{d}V \ . \tag{3.6}$$

The time discretization of the precursors equations (3.5), is done by using a one-step implicit finite differences scheme. To obtain this scheme, we make use of the change.

$$P C_k = e^{-\lambda_k t} B_k \ , \tag{3.7}$$

obtaining

$$\frac{dB_k}{dt} = e^{\lambda_k t} \beta_k \left(M_{11} M_{12}\right) \tilde{\Phi}(t) \ . \tag{3.8}$$

This equation is integrated between t_n and t,

$$B_k(t) = B_k^n + \int_{t_n}^{t} e^{\lambda_k \tau} \beta_k \left(M_{11} M_{12} \right) \tilde{\Phi}(\tau)\, d\tau. \tag{3.9}$$

Making use of the change (3.7), C_k^{n+1} can be expressed as

$$P C_k^{n+1} = e^{-\lambda_k \Delta t_n} P C_k^n + e^{-\lambda_k t_{n+1}} \int_{t_n}^{t_{n+1}} e^{\lambda_k \tau}\, \beta_k \left(M_{11} M_{12} \right) \tilde{\Phi}(\tau)\, d\tau\ . \tag{3.10}$$

where $\Delta t = t_{n+1} - t_n$. The term $\left(M_{11} M_{12} \right) \tilde{\Phi}(t)$ inside the integral is approximated by its value at the instant t_{n+1} obtaining

$$P C_k^{n+1} = P C_k^n e^{-\lambda_k \Delta t} + \frac{\beta_k}{\lambda_k} \left(1 - e^{\lambda \Delta t} \right) \left(M_{11}^{n+1} M_{12}^{n+1} \right)\ \tilde{\Phi}^{n+1}\ . \tag{3.11}$$

In the same way, Euler's backward method is used in equation (3.4) obtaining,

$$[\tilde{\mathrm{v}}^{-1}] \frac{1}{\Delta t} \left(\tilde{\Phi}^{n+1} - \tilde{\Phi}^n \right) + L^{n+1} \tilde{\Phi}^{n+1} = (1 - \beta\ ) M^{n+1} \tilde{\Phi}^{n+1} + \sum_{k=1}^{K} \lambda_k X C_k^{n+1}\ . \tag{3.12}$$

Taking into account equation (3.11), equation (3.12) is rewritten as the system of linear equations

$$T^{n+1} \tilde{\Phi}^{n+1} = R^n \tilde{\Phi}^n + \sum_{k=1}^{K} \lambda_k e^{-\lambda_k \Delta t} X C_k^n\ , \tag{3.13}$$

where the matrices are defined as,

$$\begin{aligned} T^{n+1} &= \frac{1}{\Delta t} [\mathrm{v}^{-1}] + L^{n+1} - \hat{a} M^{n+1}\ , \\ R^n &= \frac{1}{\Delta t} [\mathrm{v}^{-1}] = \frac{1}{\Delta t} \begin{pmatrix} P\,\mathrm{v}_1^{-1} & 0 \\ 0 & P\,\mathrm{v}_2^{-1} \end{pmatrix}\ , \end{aligned}$$

and the coefficient $\hat{a}$ is

$$\hat{a} = 1 - \beta\ + \sum_{k=1}^{K} \beta_k \left(1 - e^{\lambda_k \Delta t} \right)\ .$$

This system of equations is large and sparse and has to be solved for each time step. As it was done in before in the eigenvalue problem (Equqtion 1.42) , the preconditioned BICGSTAB [114] method has been chosen to solve these systems and the preconditioner used has been the incomplete LU preconditioner.

3.3.1 Mesh interpolation

Traditionally, the time dependent neutron equation is solved using a spatial mesh that is fixed along all the transient. As it has been already mentioned, the simulation of transients where the control rod banks move suffer from the rod-cusping problem because averaged cross sections are used for the partially rodded nodes. Here, we propose the use of a spatial mesh that changes each time step following the control rod in such a way that we do not have partially rodded nodes. This scheme requires the interpolation of the physical solutions of the equations, which are continuous functions, from the old mesh in step n to the next mesh corresponding to step $n+1$.

The mesh interpolation process consists of finding the solution in the new support point values corresponding to the new mesh by polynomial interpolation of the values of the solution in the old mesh. To maintain the accuracy of the solution this interpolation is done using Lagrange polynomials of the same degree as the degree used in the high order finite element method used for the spatial discretization. In other words, the exact finite element solution was projected to the new mesh.

To formalise the interpolation method we use the superscript notation to refer to the time step number and the subscript notation to the mesh number step. Then, Φ_m^n refers to the neutronic flux at time step n in the mesh m. The interpolation process between meshes described above is implemented by means of a function f, and can be written as

$$\Phi_{m+1}^n = f(\Phi_m^n) \ , \tag{3.14}$$

$$C_{k,\, m+1}^n = f(C_{k,\, m}^n) \ . \tag{3.15}$$

Figure 3.5 shows an example of the neutron flux interpolation $\Phi^n(z)$ between two consecutive meshes. This interpolation is similar to the one used in h-refined finite elements codes to interpolate from the coarse mesh to a finer mesh to accelerate the convergence of the solution in the finer mesh [46]. However in the moving mesh method, the support points of the mesh are moved and not only coarse cells are subdivided into finer cells.

In the moving mesh interpolation, only physical quantities, which are continuous functions, can be interpolated adequately. However, from equation (3.11), the obtained quantity for each time step is PC_k^n and the physical magnitude needed for the interpolation is C_k^n, which can be obtained inverting the mass matrix P. But this is a computationally expensive task and, to avoid this calculation, an approximation, $\hat{P}$, for the mass matrix P is considered by means of a mass lumping technique [17].

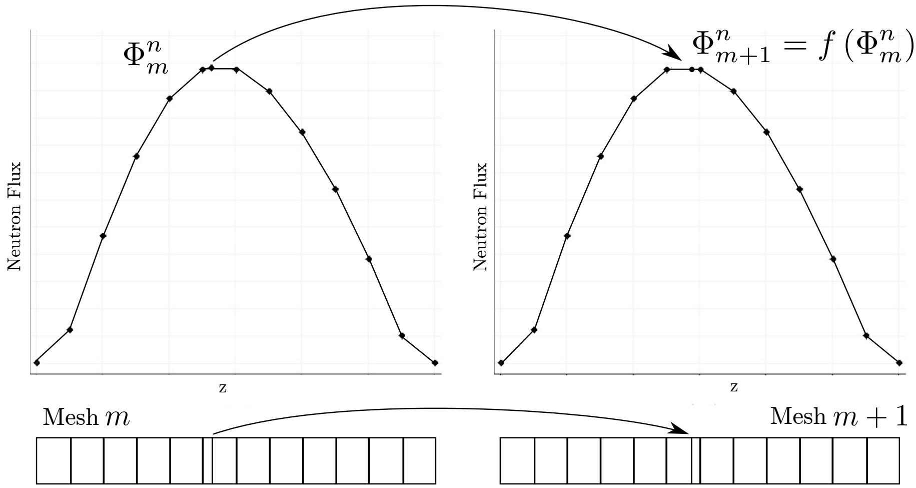

Figure 3.5: 1D Mesh interpolation example.

This procedure mainly consists of considering matrix $\hat{P}$ as a diagonal matrix whose elements are the result of summing all the elements of each row of matrix P. This is equivalent to calculate the integrals involving polynomials up to order s approximately with a quadrature rule up to order $s-1$ in the finite element method [115].

The inverse of the mass lumped matrix $\hat{P}$ is a diagonal matrix calculated as

$$\hat{P}^{-1}_{ii} = \frac{1}{\sum_{e=1}^{N_e}\left(\sum_{j=1}^{N_i}\int_{\Omega_e} N_{1i}N_{1j}\mathrm{d}V\right)} \,. \tag{3.16}$$

In the usual fixed mesh scheme, since there is not any interpolation of physical quantities, it is not necessary to know the value of C^n_k because it is enough to obtain PC^n_k for each time step.

The main steps for the implementation of the moving mesh procedure are summarized in the scheme shown in Figure 3.6.

The computation starts with an eigenvalue computation to obtain the stationary configuration of the reactor core, which is used as initial condition. Then, the dynamic calculation starts. First, the neutron precursors concentration equations are solved in the initial mesh. The control bars and the mesh are moved and the neutronic flux and the precursors distribution are interpolated to the new mesh. Then, the system associated with the numerical scheme is solved obtaining the next flux distribution. This is clearly the most time consuming part of the computation. Finally, the stopping criterion is checked and, if it is not fulfilled, the dynamic computation is repeated for the next time step.

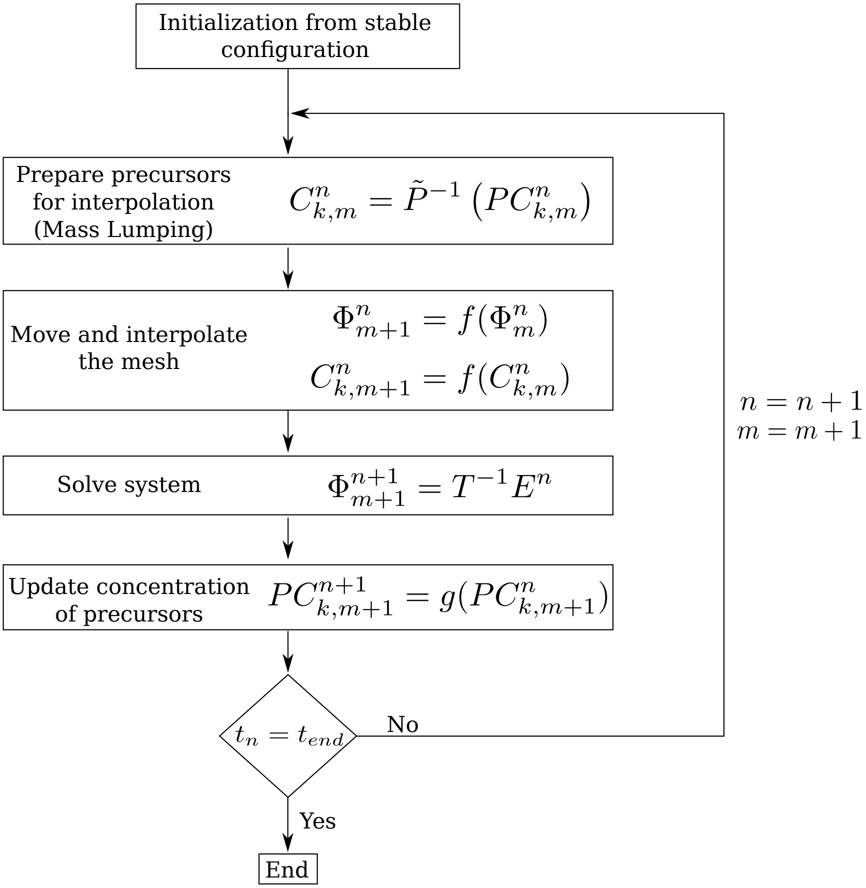

Figure 3.6: Summary of the moving mesh time scheme.

3.4 Numerical results

To study the performance of the moving mesh scheme, three benchmark problems have been analysed. The first benchmark consists of a one dimensional problem where a control rod is ejected to a given velocity and then inserted back. The second benchmark is a small 3D hexagonal reactor where also a rod ejection accident is studied. The first exercise of the AER benchmark, the three-dimensional VVER-440 reactor is the third reactor which has been studied.

Firstly, the spatial discretization is tested solving the critical configuration of the reactor.Then,the time dependent problem is solved using the classical fixed mesh scheme and the proposed moving mesh scheme. To compare the performance of the finite element method used for the spatial discretization, and to set the adequate spatial discretization parameters, different errors have been employed, which are shown in Table 2.1.

3.4.1 One dimensional problem

To validate the code a simple and small one-dimensional reactor is considered, which represents a simplified model for a rod-ejection accident. This reactor consists of 12 cells composed of different materials. The reactor geometry is defined in Figure 3.7 and the cross sections for the materials of each region are given in Table 3.1. Precursor parameters are given in Table 3.2. Zero-current boundary conditions are imposed at the boundaries of the system.

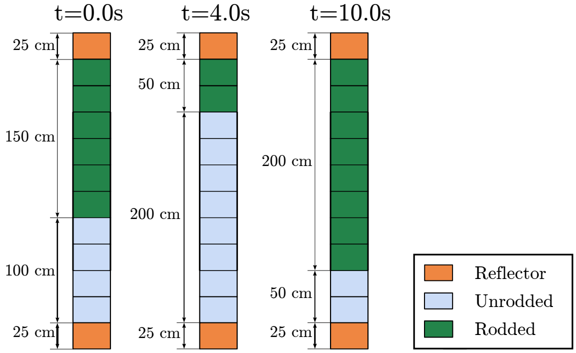

Figure 3.7: Geometry of the 1D reactor problem.

The transient consists of removing the control rod from time 0.0 s to 4.0 s with a constant velocity of 25 cm/s. Then the control rod is inserted again from 4.0 s to 10 s also with a constant velocity of 25 cm/s. All the transient calculations are made using cubic polynomials in the finite element method. Reference results for

Table 3.1: Cross sections of the materials of the 1D reactor.

Fuel	**Group**	$\mathbf{D_g}$ (*cm*)	$\boldsymbol{\Sigma_{ag}}$ (1/ *cm*)	$\boldsymbol{\nu\Sigma_{fg}}$ (1/ *cm*)	$\boldsymbol{\Sigma_{fg}}$ (1/ *cm*)	$\boldsymbol{\Sigma_{12}}$ (1/ *cm*)
Unrodded	1	1.40343	1.17659e-2	5.62285e-3	2.20503e-3	1.60795e-2
Fuel	2	0.32886	1.07186e-1	1.45865e-1	5.90546e-2	
Rodded	1	1.40343	1.17659e-2	5.60285e-3	2.19720e-3	1.60795e-2
Fuel	2	0.32886	1.07186e-1	1.45403e-1	5.88676e-2	
Reflector	1	0.93344	2.81676e-3	0.00000e+0	0.00000e+0	1.08805e-2
	2	0.95793	8.87200e-2	0.00000e+0	0.00000e+0	

Table 3.2: Neutron precursors parameters for the reactor.

	Group 1	Group 2	Group 3	Group 4	Group 5	Group 6
β_i	0.000247	0.0013845	0.001222	0.026455	0.000832	0.000169
λ_i $(1/s)$	0.0127	0.0317	0.115	0.311	1.4	3.87
	$\mathrm{v}_1 = 1.27 \times 10^7 \ cm/s$		$\mathrm{v}_2 = 2.5 \times 10^5 \ cm/s$		$\beta = 0.0065$	

the neutronic flux and the k_{eff} of the problem are computed with the neutronic code PARCS [92], using a fixed mesh with 120 cells where the rod-cusping problem should be eliminated.

The results obtained for the dominant eigenvalue k_{eff} using different polynomial degrees for the finite element method (Degree of FE) are shown in Table 3.3. In this Table, also the number of degrees of freedom (DoF) are shown for the reduced eigenvalue problem (Equqtion 1.42) in order to have an idea of the size of the problem solved. Also the mean relative errors and maximum relative errors per cell for the neutronic flux and power are shown for the initial configuration for the reactor.

Table 3.3: Dominant eigenvalue and power distribution results for the 1D reactor.

Degree of FE	**DoF**	$\mathbf{k_{eff}}$	$\boldsymbol{\Delta}\mathbf{k_{eff}}$ (*pcm*)	**Power** $\bar{\varepsilon}$ (%)	$\varepsilon_{\max}$(%)	**Fast Flux** $\bar{\varepsilon}$ (%)	$\varepsilon_{\max}$(%)	**Thermal Flux** $\bar{\varepsilon}$ (%)	$\varepsilon_{\max}$(%)
1	13	0.978430	38.1	2.98	9.84	7.17	29.2	7.64	31.62
2	25	0.978757	5.4	0.49	1.54	1.02	3.85	0.62	1.55
3	37	0.978801	1.0	0.10	0.38	0.16	0.53	0.10	0.41
PARCS		0.978811							

Figure 3.8 shows a detail of the evolution of the normalized mean power, computed with the expression

$$\bar{P}w(t) = \frac{\int_{\Omega} \left(\Sigma_{f1}\phi_1(t) + \Sigma_{f2}\phi_2(t)\right) \mathrm{d}V}{\int_{\Omega} \left(\Sigma_{f1}\phi_1(0) + \Sigma_{f2}\phi_2(0)\,\right) \mathrm{d}V} \ , \tag{3.17}$$

During the transient computed using a classical fixed mesh scheme with a mesh of 12 nodes, the moving mesh scheme presented in this work and the reference values.

As can be seen in this Figure, the fixed mesh computations present some unphysical jumps in the normalized mean power, mainly when the control rod is in the middle of a cell. However the rod-cusping problem is mitigated with the moving mesh scheme reducing the mean error in the power about three times, from 0.3% to 0.13%. Moreover, the relative errors for the reactor mean power for each one of the time steps obtained with the fixed mesh scheme and the moving mesh scheme are shown in Figure 3.9.

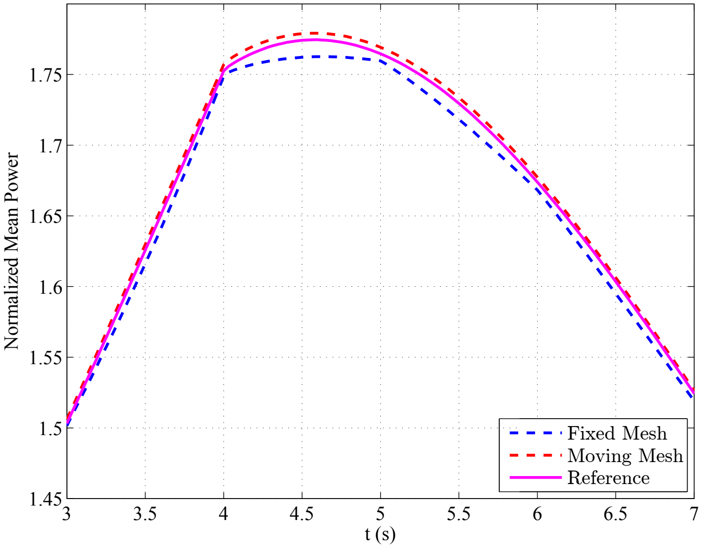

Figure 3.8: Normalized power evolution for the 1D reactor from 3s to 7s.

Figure 3.10 shows the errors in the computation of the dominant eigenvalue (Δk_{eff}) solving an static problem for all the time steps of the transient. As it can be seen in these Figures, the errors for the k_{eff} and the reactor power have very similar behaviours.

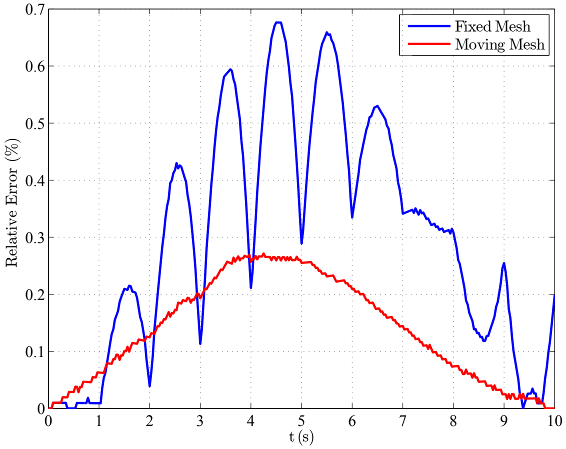

Figure 3.9: Comparative of errors of relative mean power over time in 1D reactor.

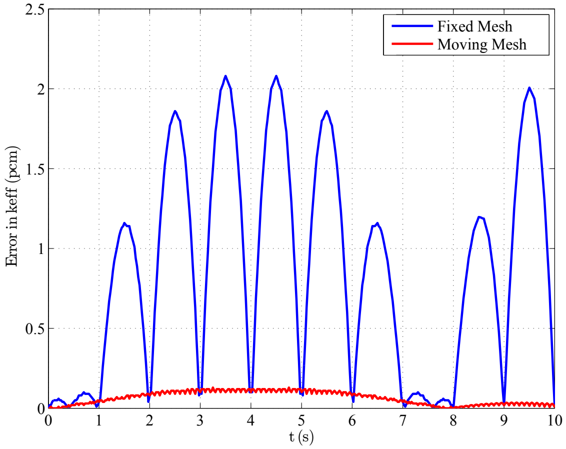

Figure 3.10: Errors in k_{eff} during the transient.

3.4.2 Small hexagonal reactor

To test the performance of the method in 3D reactors, a small reactor that presents a large rod-cusping problem is studied [116]. Figure 3.11 shows the layout map of the small hexagonal reactor [116], for which the hexagonal lattice pitch is 23.6 *cm*. The material cross sections of the different materials composing the reactor are given in Table 3.4. The neutron precursors data used in this problem are given in Table 3.5.

Material 1 represents the fuel assemblies, material 2 represents the absorber assemblies, and material 3 represents the reflector. Material number 22 and 24 represent the positions where, either absorber assemblies (material 2) or their fuel followers (material 1), have to be placed into, due to the axial position of the given absorber assembly. Material number 23 is used for the ejected rod. One layer of axial reflector at the top, another one at the bottom of the reactor, and a radial layer of reflector are used.

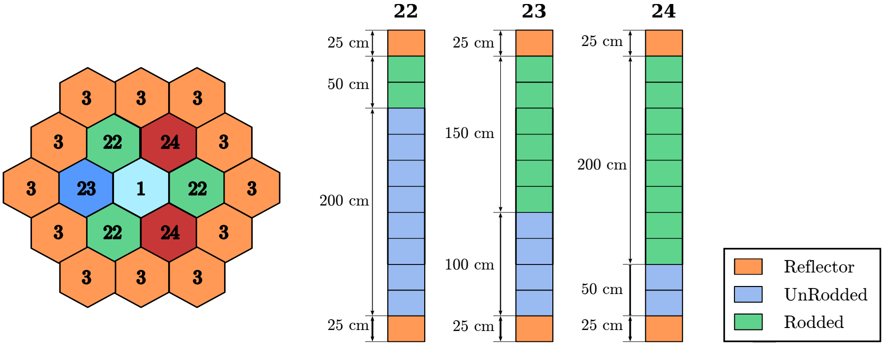

Figure 3.11: Small reactor geometry.

Table 3.4: Cross section definitions for the small reactor.

Fuel	**Group**	$\mathbf{D_g}$ (*cm*)	$\boldsymbol{\Sigma_{ag}}$ (1/ *cm*)	$\boldsymbol{\nu\Sigma_{fg}}$ (1/ *cm*)	$\boldsymbol{\Sigma_{fg}}$ (1/ *cm*)	$\boldsymbol{\Sigma_{12}}$
Unrodded	1	1.40343	1.17659e-2	5.62285e-3	2.20504e-3	1.60795e-2
Fuel	2	0.32886	1.07186e-1	1.45865e-1	6.00267e-2	
Rodded	1	1.36764	1.39118e-2	5.37719e-3	2.10870e-3	1.35108e-2
Fuel	2	0.25108	9.96214e-2	1.15403e-1	4.74909e-2	
Reflector	1	0.93344	2.81676e-3	0.00000e+0	0.00000e+0	1.08805e-2
	2	0.95793	8.87200e-2	0.00000e+0	0.00000e+0	

Albedo boundary conditions are applied on the outer edge of the reflector cells. The extrapolation length is set to $2 \times D_g$. The height of the reactor is 300 *cm* and 12 axial planes are considered, each one of 25 *cm*. The first one and the last one are reflector layers defined by material of type 3. The initial position of control rod group 22 (see Figure 3.11) is at 200 *cm* above the bottom reflector (Follower in 2nd -9th axial nodes, absorber rod in 10th -11th axial nodes), the initial position of control rod group 23 is at 100 *cm* above the bottom reflector, and the initial position of control rod group 24 is at 75 *cm* above the bottom reflector.

The transient simulates a rod ejection accident as follows.

- At time $t = 0.0$s , starting from the initial configuration (see Figure 3.11), the rod 23 begins to be removed until it is completely removed at time $t = 0.15$s remaining only the unrodded fuel.
- From $t = 0.15$s until $t = 1.0s$ nothing happens.
- When the security system acts, a scram is produced inserting absorbers at constant velocity of 25 cm/s in positions 22 from time $t = 1.0$s until the bottom of the reactor is reached at time $t = 9.0$s.

Table 3.5: Neutron precursors parameters for the reactor.

	Group 1	Group 2	Group 3	Group 4	Group 5	Group 6
β_i	0.000247	0.0013845	0.001222	0.026455	0.000832	0.000169
λ_i $(1/s)$	0.0127	0.0317	0.115	0.311	1.4	3.87
	$\mathrm{v}_1 = 1.27 \times 10^7$ cm/s		$\mathrm{v}_2 = 2.5 \times 10^5$ cm/s		$\beta = 0.0065$	

The results obtained for the dominant eigenvalue (k_{eff}) using different polynomial degrees for the finite element method (Degree of FE) are shown in Table 4.4. In this Table, the number of degrees of freedom (DoF) of the reduced eigenvalue problem are also shown together with the mean relative errors and maximum relative errors per cell in the neutronic flux and power for the initial configuration of the reactor.

Table 3.6: Critical eigenvalue and power distribution results for the small 3D reactor.

Degree of FE	**DoF**	**k$_{\text{eff}}$**	**Δk$_{\text{eff}}$**	**Power**		**Fast Flux**		**Thermal Flux**	
			(*pcm*)	$\bar{\varepsilon}$ (%)	$\varepsilon_{\max}$(%)	$\bar{\varepsilon}$ (%)	$\varepsilon_{\max}$(%)	$\bar{\varepsilon}$ (%)	$\varepsilon_{\max}$(%)
1	949	0.801287	1539.0	6.38	17.70	15.49	38.13	16.34	36.45
2	6475	0.815211	146.4	0.97	0.84	1.98	3.40	1.14	3.26
3	20683	0.816024	65.3	0.15	0.35	0.17	0.66	0.23	0.81
PARCS		0.816677							

Figure 3.12 shows the time evolution of the normalized mean power of the reactor in the first $t = 7.0$ secondss. In this Figure, the results obtained with the moving mesh scheme proposed in this work are compared with the results obtained with the classical fixed mesh scheme. The reactor with the fixed mesh scheme is solved using 120 axial planes where the rod-cusping problem is very small and the results of this computation are taken as a reference. All transient calculations are made using cubic polynomials in the finite element method.

The time evolution of the relative errors for the reactor total power obtained with the fixed mesh scheme and the moving mesh scheme are shown in Figure 3.13.

As can be seen in these Figures, when a small number of axial planes are used, the fixed mesh computations present some unphysical jumps in the normalized mean power, mainly when the control bar is in the middle of a cell.

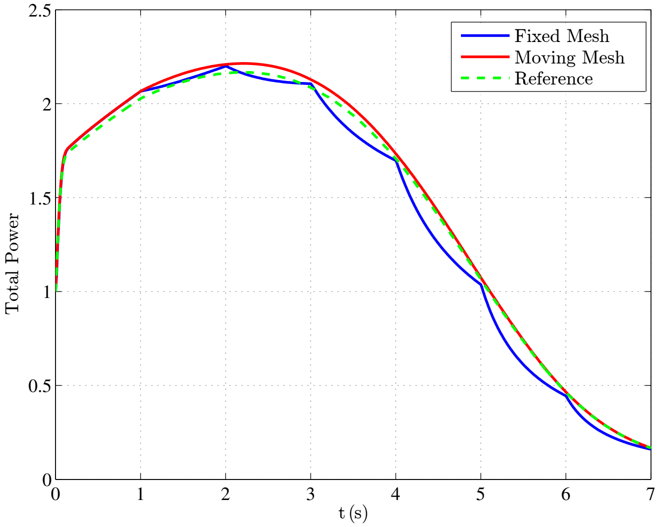

Figure 3.12: Normalized mean power evolution for the small 3D reactor.

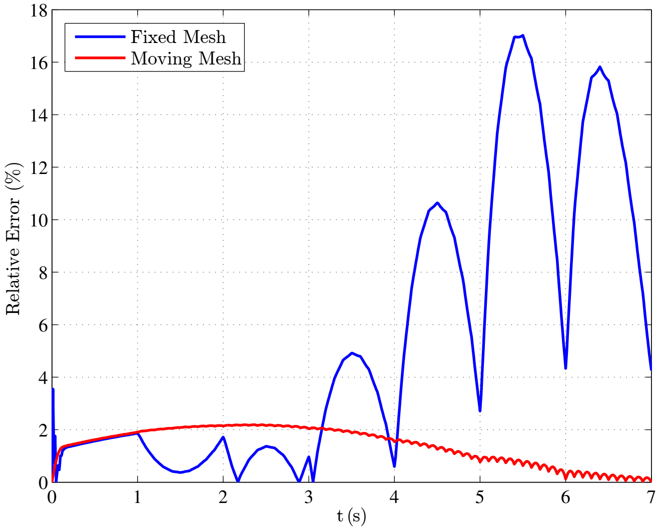

Figure 3.13: Normalized mean power error for the small 3D reactor.

However the rod-cusping problem is mitigated with the moving mesh scheme reducing the mean error in the power more than three times, from 5.50 % to 1.41 %. Thus, the moving mesh scheme produces better results than the fixed mesh scheme when a small number of axial planes are considered for the spatial discretization.

3.4.3 AER benchmark -VVER-440 3D

To test the performance of the proposed method in a realistic reactor the transient benchmark AER-DYN-001 proposed in [117] has been studied. This problem corresponds to an asymmetric control rod ejection accident in a VVER-440 core. A plane of this reactor showing the disposition of materials together with the initial position of control rods are shown in Figure 3.14. The hexagonal lattice pitch is 14.7 *cm*.

The material cross sections of the different materials composing the reactor are summarized before in Chapter 2 in Table 2.21. The kinetic parameters for the six groups of neutron precursors and for the velocities are shown in Table 3.7.

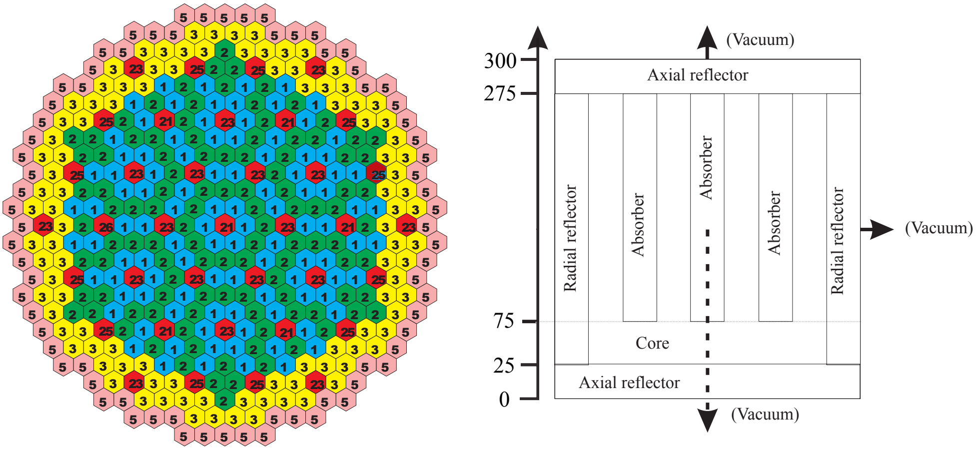

Figure 3.14: Geometry of VVER 440 reactor core.

Type numbers 1, 2, 3 represent fuel assemblies of different enrichment (1.6 % , 2.4 %, 3.6 %). Type numbers (21, 23, 25, 26) represent the positions where either absorber assemblies (type 4) or their fuel followers (1,2,3) have to be placed into, due to the axial position of the given absorber assembly. Type "26" is used for the ejected rod. Type number "5" represents reflector cells.

The albedo boundary condition is applied on the outer edge of the reflector nodes, the extrapolation length is $2.13Dg$ in both groups, where Dg is the diffusion coefficient given for type "5".

Figure 3.14 also shows the axial arrangement of the problem. For the sake of comparable output, the minimum number of axial nodes has to be 12. The 1^{st} node for the bottom reflector, $2^{nd} - 11^{th}$ nodes for the active length of the core (250 cm), the 12^{th} node for the top reflector. In this case, the height of the nodes is $25cm$. The initial position of control rod groups 21 and 26 is at $50cm$ above the bottom reflector. (Follower in $2^{nd} - 3^{rd}$ axial nodes, absorber rod in $4^{th} - 11^{th}$ axial nodes). Control assembly groups type "23 and 25" are out of the core at the beginning of the process.

Table 3.7: Neutron precursors parameters for the reactor.

	Group 1	Group 2	Group 3	Group 4	Group 5	Group 6
β_i	0.000247	0.0013845	0.001222	0.026455	0.000832	0.000169
λ_i $(1/s)$	0.0127	0.0317	0.115	0.311	1.4	3.87
	$v_1 = 1.25 \times 10^7 \ cm/s$		$v_2 = 2.5 \times 10^5 \ cm/s$		$\beta = 0.0065$	

The transient is defined as follows:

- The control rod denoted by number 26 is ejected in the first 0.08 seconds (from 75 cm height in the initial Position to 275 cm height at the final position) with a constant velocity of 2500 cm/s. The worth of the ejected rod is marginally below the prompt critical value. The delayed neutron precursors are moving together with the fuel of the absorber followers.
- Then, Scram is initiated at 1.0 sec by dropping safety rods 23 and 25 at a constant velocity of 5 cm/s. These rods take 11.0 seconds to reach the bottom of the core.
- The drop of control rod group 21 is also started at 1.0 s with the same velocity of 5 cm/s.

In Figure 3.15 the total power evolution is presented for several calculations. First, the power evolution has been computed with the nodal code PARCS [92] using 12 axial planes. These computations present a strong rod cusping problem. In the same way the finite element method with a fixed mesh presents a similar behaviour for the computation with 12 axial planes.

To avoid the rod cusping we have computed the transient using the moving mesh scheme with 12 axial planes. In this case, the power evolution is comparable to the behaviour obtained with the PARCS code using 120 axial planes. To be self-consistent, a reference finite element solution, with fixed mesh and 60 axial planes, is also shown. All the calculation have been performed with a maximum time step of 0.01s because this is the maximum time step that achieves sufficient converged results.

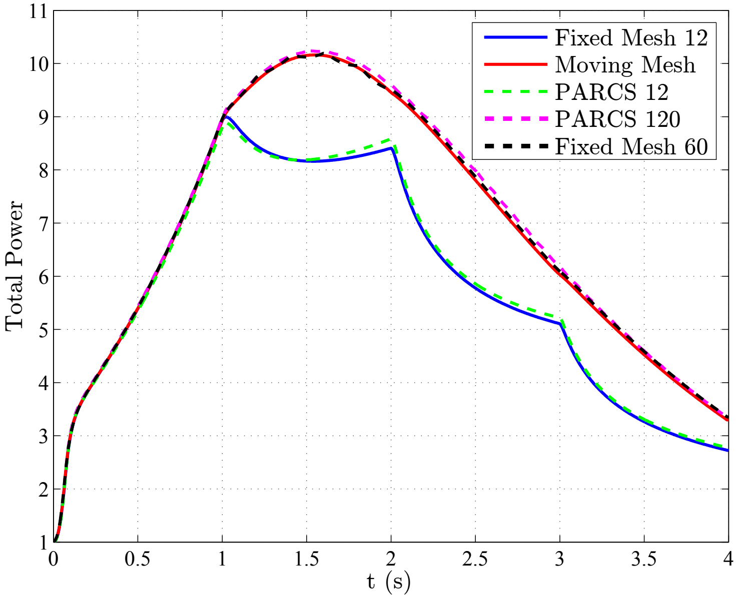

Figure 3.15: Power evolution for the VVER-440 reactor.

In Figure 3.16 and 3.17 the radial power distributions with 12 axial planes are illustrated at the beginning and at the end of the process comparing the results obtained using a polynomial degree p=2 with the the results obtained with PARCS code and DYN3D code. The power distributions are shown along the diameter of the core (middle symmetry line on Figure 3.14), at the 3rd elevation (elevations are numbered from the bottom reflector: 1-12). Node number "426" belongs to the ejected rod.

Figure 3.18 presented the relative error in each node of the radial profile of the code and PARCS codes with 12 axial planes, using the solution obtained with DYN3D code as the reference. It is observed that the maximum error obtained is less than a 4%.

We can note that all the reactors tested show a good agreement in the normalized power radial profile with both the DYN3D and the PARCS codes. Also shows that the moving mesh method has a better performance that the traditional fixed mesh scheme when a small number of axial cells are used. The moving mesh scheme permits to use a coarser discretization and reduces the computational effort.

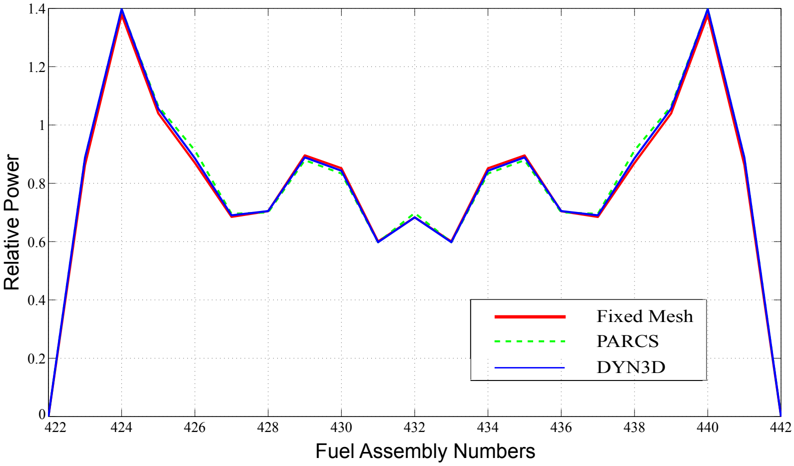

Figure 3.16: Normalized radial Power at $t = 0s$.

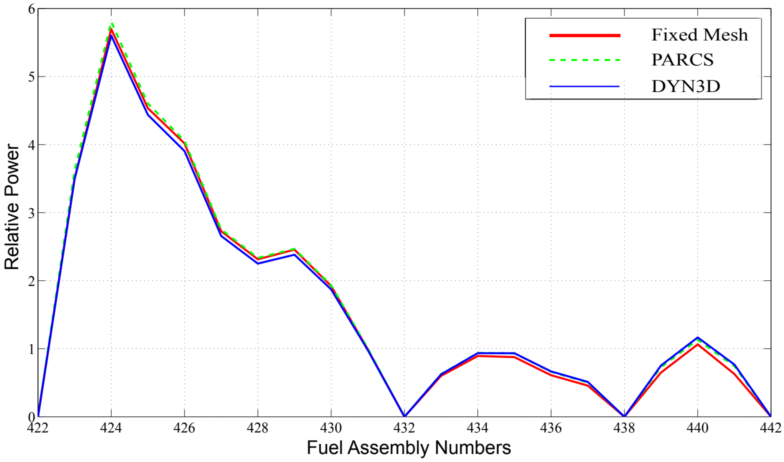

Figure 3.17: Normalized radial Power at $t = 6s$.

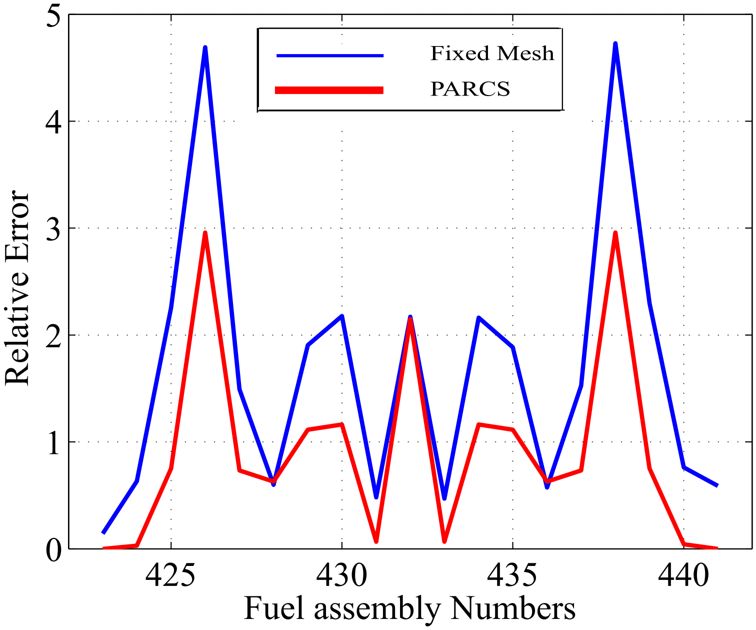

Figure 3.18: Relative error with respect to DYN3D at $t = 0s$.

Chapter 4

High Order Finite Element Method for The Simplified Spherical Harmonics Equations

For reactor calculations, the usual approximation of the neutron transport equation by the multigroup neutron diffusion equation does not provide good results for complex fuel assemblies or other applications as the ones using fine mesh (pin by pin geometries). Diffusion theory is not valid when strong material and/or flux gradients are present, when neutron streaming is significant or when neutron scattering contains a strongly anisotropic component. As such situations have become increasingly more common in commercial nuclear reactor analysis more accurate neutron transport are needed.

To improve the results of nodal diffusion theory for situations such as those that are mentioned above, a computational method that incorporates higher-order approximations for the angular dependence of the neutron flux must be employed. Time-dependent formulations for finite-differenced discrete ordinates (S_N) methods [28, 29], spherical harmonics (P_N) methods and simplified spherical harmonics (SP_N) methods have all been investigated [30–32].

A classical approach to solve the neutron transport equation is to apply the spherical harmonics method obtaining a finite approximation known as the P_N equations. P_N equations are classical approximations to the neutron transport equation admitting a diffusive form. Using this property, for example a nodal collocation method has been developed for the P_N approximations, which is based on the expansion of the angular dependence of flux in terms of orthonormal Legendre polynomials [31]. This method approximates the differential lambda Modes problem by an algebraic eigenvalue problem from which the fundamental and the subcritical modes of the system can be calculated.

The spherical harmonic or P_N approximation has been well established for many decades [33]. It is obtained by expanding the angular dependence of the neutron flux in terms of spherical harmonic functions and retaining only spherical harmonics up to order N. The exact transport solution is recovered as $N \to \infty$. In three-dimensional geometries, the number of P_N equations grows like $(N+1)^2$ but in one-dimensional planar geometry, the number of P_N equations is only $(N+1)$. The P_N equations in one-dimensional planar geometry are relatively simple and can be reformulated in second-order form as $(N+1)/2$ diffusion like equations coupled only through the angular moments. The P_N equations in multidimensional geometries are complicated but can also be formulated as second-order equations. However, there are a larger number of these equations, and the coupling involves not only the angular moments but also mixed spatial derivatives of these moments.

This realization led Gelbard [34–36] to propose a multi-dimensional generalization of the planar geometry P_N equations which avoids the complexities of the full spherical harmonics approximation - the simplified P_N (SP_N) equations in the early 1960s. Gelbard presented a simplification to the full spherical harmonics method that greatly reduced the number of unknowns, and also provided an analysis when the method was equivalent to the full P_N equations, see [34–36]. Gelbard replaced the second derivatives in the one-dimensional planar geometry P_N equations with general three-dimensional Laplacian operators. This substitution yields an ad-hoc multidimensional generalization of the planar geometry P_N equations that avoids the complexities of the full spherical harmonics approximation. Gelbard tested the SP_N approximation in one-dimensional cylindrical [34, 35] and spherical [36] geometries, and the results appeared promising.

Although, unlike P_N , the SP_N solution does not converge to the true transport solution as $N \to \infty$, it is more accurate than the diffusion theory results and still can be obtained within acceptable computing times. The main advantage of the SP_N approximation compared to the Spherical Harmonics is the number of equations involved and their implementation. The number of equations to be solved shows increases by $(N+1)^2$ for spherical harmonics, while it shows increases by $(N+1)$ for SP_N. Moreover, the implementation of the SP_N equations on a computer requires much less effort than spherical harmonics, and the cost of computation for the SP_N method is greatly reduced. In addition, the SP_N approximation does not suffer from the ray effects [118] that can adversely affect discrete ordinates S_N methods for certain types of problems.

4.1 1D P_N equations

Let the eigenvalue problem associated with the following one-group slab geometry transport problem and vacuum boundary conditions be the starting point for the following derivation of the planar-geometry P_N equations [38, 39].

$$\begin{aligned}&\mu\frac{\partial\Psi(x,\mu)}{\partial x}+\Sigma_t(x)\Psi(x,\mu)\\&=\int_{-1}^{+1}\Sigma_s\left(x,\mu_0\right)\Psi\left(x,\mu'\right)d\mu'+\frac{1}{\lambda}\frac{\nu\Sigma_f(x)}{2}\int_{-1}^{+1}\Psi(x,\mu')\,d\mu'\ ,\\&\Psi(0,\mu)=0\ ,\quad 0<\mu\leq 1\ ,\qquad \Psi(x_L,\mu)=0\ ,\quad -1\leq\mu<0\ ,\end{aligned}\tag{4.1}$$

where $x\in[0,x_L]$, θ is the angle between the direction of the incident neutron velocity and the x axis, $\mu = cos(\theta)$, θ_0 is the angle between the incident neutrons and the scattered neutrons, $\mu_0 = cos(\theta_0)$. $\Sigma_t(x)$ is the total cross-section. $\Sigma_s(x,\mu_0)$ is the scattering cross-section, $\Sigma_f(x)$ is the fission cross-section and ν is the average number of neutrons produced in each fission. λ is the eigenvalue of the problem and $\Psi(x,\mu)$ its corresponding eigenvector. The solutions of this eigenvalue problem are known as the Lambda Modes of the transport equation [40]. The dominant eigenvalue, $\lambda = \mathrm{k_{eff}}$, is the k-effective of the system and measures its criticality. The corresponding eigenvector is the directional flux distribution of a stationary configuration of the system obtained dividing Σ_f by $\mathrm{k_{eff}}$.

The angular dependence of the flux and source functions in equation (4.1) can be approximated by a truncated series expansion. Therefore, the Legendre polynomials $P_n(\mu)$ are introduced representing the one-dimensional equivalents of the spherical harmonics, to obtain the expansion functions of the P_N equations. Like the spherical harmonic functions, the Legendre polynomials satisfy the relations

$$\begin{aligned}P_0(\mu)&=1,\\P_1(\mu)&=\mu,\\P_2(\mu)&=\frac{1}{2}(3\mu^2-1),\\P_3(\mu)&=\frac{1}{2}(5\mu^3-3\mu),\\(n+1)\ P_{n+1}(\mu)&=(2n+1)\mu P_n(\mu)-nP_{n-1}(\mu),\end{aligned}\tag{4.2}$$

that form an orthogonal system with the properties,

$$\int_{-1}^{1}P_n(\mu)P_m(\mu)d\mu=\frac{2}{2n+1}\delta_{n,m}\tag{4.3}$$

and

$$\mu P_n(\mu) = \frac{n}{2n+1} P_{n-1}(\mu) + \frac{n+1}{2n+1} P_{n+1}(\mu), \quad n \geq 1 \qquad , \tag{4.4}$$

where $\delta_{n,m}$ denotes the Kronecker delta.

According to this, the angular dependence of both the neutron flux distribution and the scattering cross-section can be expanded in terms of N + 1 Legendre polynomials

$$\begin{aligned} \Psi(x,\mu) &= \sum_{n=0}^{N} \left(\frac{2n+1}{2}\right) \phi_n(x) P_n(\mu) \ , \\ \Sigma_s\left(x,\mu_0\right) &= \sum_{n=0}^{N} \left(\frac{2n+1}{2}\right) \Sigma_{sn}(x) P_n\left(\mu_0\right) \ . \end{aligned} \tag{4.5}$$

where

$$\phi_n(x) = \int_{-1}^{1} d\mu \, P_n(\mu) \Psi(x,\mu) \ , \qquad \Sigma_{s_n}(x) = \int_{-1}^{1} d\mu_0 \, P_n\left(\mu_0\right) \Sigma_s\left(x,\mu_0\right) \ .$$

Inserting the neutron flux distribution and the scattering cross section expansions into equation (4.1) and with the aid of the orthogonality relations for the Legendre polynomials and the addition theorem for the associated Legendre function. We obtain the following P_N approximation [119]

$$\begin{aligned} \frac{d\phi_1\left(x\right)}{dx} + \Sigma_a \phi_0\left(x\right) &= \frac{1}{\lambda} \nu \Sigma_f \phi_0\left(x\right), \\ (n+1)\frac{d\phi_{n+1}\left(x\right)}{dx} + n\frac{d\phi_{n-1}\left(x\right)}{dx} &+ (2n+1)(\Sigma_t - \Sigma_{s_n})\phi_n\left(x\right) = 0, \quad n = 1, \ ...., \ N \end{aligned} \tag{4.6}$$

where $\Sigma_a = (\Sigma_t - \Sigma_{s_0})$ is the absorption cross section.

The P_N equations constitute a set of $N+1$ equations with $N+2$ unknowns. This problem is usually solved ignoring the term $\frac{\mathrm{d}\phi_{N+1}}{\mathrm{d}x}$ in the $n = N$ equation.To approximate the vacuum boundary conditions, we shall consider Marshak's conditions [39].

$$\int_{0}^{1} P_m\left(\mu\right) \Psi(0,\mu) \mathrm{d}\mu = 0, \qquad \int_{-1}^{0} P_m\left(\mu\right) \Psi(x_L,\mu) \mathrm{d}\mu = 0, \tag{4.7}$$

with m odd, $m = 1, 3, \ldots, N$ (*or* $N-1$).

We will consider only the odd-order P_1 , P_2 and P_3 approximations.

4.1.1 Boundary condition

The true boundary condition at the left boundary x_L , are

$$\Psi(x_L, \mu) = \Psi_{in}(x_L, \mu), \quad \mu > 0, \tag{4.8}$$

where $\Psi_{in}(x_L, \mu > 0)$ is a known incident flux ($\Psi_{in}(x_L, \mu > 0) = 0$ is the vacuum boundary condition). This condition cannot be satisfied exactly by the angular flux approximation of equation (4.5), for a finite N. The most obvious way to develop approximate boundary conditions that are consistent with the flux approximation is to substitute equation (4.5) into the exact boundary condition given by equation (4.8), multiply by $P_m(\mu)$, and integrate over $0 \leq \mu \leq 1$ [25]. Since it is the odd Legendre polynomials that represent directionality (i.e., are different for μ and $-\mu$), this procedure is repeated for all the odd Legendre polynomials $m = 1, 3, \ldots, N$(or $N-1$) as weighting functions to obtain, with the use of the orthogonality relation of equation (4.4), the Marshak's boundary conditions

$$\int_0^1 \mathrm{d}\mu\; P_m(\mu) \sum_{n=0}^{N} \left(\frac{2n+1}{2}\right) \phi_n(x_L)\; P_n(\mu) \equiv \phi_m(x_L) = \int_0^1 \mathrm{d}\mu\; P_m(\mu)\, \psi_{in}(x_L, \mu), \tag{4.9}$$

with m odd, $m = 1, 3, \ldots, N$ (*or* $N-1$).

Equations (4.9) constitute a set of $(N+1)/2$ boundary conditions. An additional $(N+1)/2$ boundary conditions are obtained similarly for the right boundary. The Marshak's boundary conditions ensure that the exact inward partial current at the boundary is incorporated into the solution; that is,

$$\begin{aligned} J^+(x_L) &\equiv \int_0^1 \mathrm{d}\mu\; P_1(\mu) \sum_{n=0}^{N} \left(\frac{2n+1}{2}\right) \phi_n(x_L) P_n(\mu) \\ &\equiv \int_0^1 \mathrm{d}\mu\; P_1(\mu)\, \psi_{in}(x_L, \mu) \equiv J^+_{in}(x_L) \end{aligned} \tag{4.10}$$

A less intuitive set of Mark's boundary conditions arises from requiring that the flux expansion of equation (4.5) satisfies the boundary condition

$$\int_0^1 \sum_{n=0}^{N} \left(\frac{2n+1}{2}\right) \phi_n(x_L) P_n(\mu_i) = \psi_{in}(x_L, \mu_i), \quad \mu_i > 0, \tag{4.11}$$

for the $(N+1)/2$ discrete values of μ_i in the inward direction, which are the positive roots of $P_{N+1}(\mu_i) = 0$. Another $(N+1)/2$ approximate boundary conditions are obtained at the other boundary by requiring that the flux expansion satisfy the true boundary condition for the $(N+1)/2$ discrete values of μ_i in the inward direction which are the negative roots of $P_{N+1}(\mu_i) = 0$. These Mark's boundary conditions are justified by the fact that analytical solution of the P_N equations for a source free, purely absorbing problem in a infinite half-space leads to these conditions. However, experience has shown that results obtained with the Mark's boundary conditions are generally less accurate than results obtained with the Marshak's boundary conditions. A symmetry, or reflective, boundary condition $\psi_{in}(x_L, \mu) = \psi_{in}(x_L, -\mu)$ obviously requires that all odd moments of the flux vanish [i.e., $\phi_n(x_L) = 0$ for $n = 1, 3, \ldots$, odd].

4.1.2 P_1 equations

Considering $N = 1$ in equation (4.6), (i.e. we assume that angular flux is at most linearly anisotropic), the P_1 approximation equations are

$$\begin{aligned} \frac{d\phi_1}{dx} + \Sigma_a \phi_0 &= \frac{1}{\lambda} \nu \Sigma_f \phi_0 \ , \\ \frac{d\phi_0}{dx} + 3(\Sigma_t - \Sigma_{s1})\phi_1 &= 0 \ , \end{aligned} \tag{4.12}$$

assuming that the source is isotropic, the second of the P_1 equations yields a Fick's law for neutron diffusion:

$$\phi_1 = \int_{-1}^{1} \mu \Psi(x, \mu) d\mu \ = -D \frac{d\phi_0}{dx}, \tag{4.13}$$

which, when used in the first of the P_1 equations, yields the neutron diffusion equation or the diffusive form of the P_1 equation.

$$-\frac{d}{dx}\left(D \frac{d\phi_0}{dx}\right) + \Sigma_a \phi_0 = \frac{1}{\lambda} \nu \Sigma_f \phi_0, \tag{4.14}$$

where $D = \frac{1}{3(\Sigma_t - \Sigma_{s1}})$ is the diffusion coefficient.

The basic assumptions made in this derivation of diffusion theory are that the angular dependence of the neutron flux is linearly anisotropic:

$$\Psi(x,\mu) \simeq \frac{1}{2}\phi_0(x) + \frac{3}{2}\phi_1(x), \tag{4.15}$$

and that the neutron source is isotropic, or at least has no linearly anisotropic component. Diffusion theory should be a good approximation when these assumptions are valid (i.e., in media for which the distribution is almost isotropic because of the preponderance of randomizing scattering collisions, away from interfaces with dissimilar media, and in the absence of anisotropic sources).

From the vacuum Marshak's ($J_{in}^{+} = 0$) boundary conditions (equation (4.11)),

$$\begin{aligned} J_{in}^{+}(x_L) &= \int_0^1 \mathrm{d}\mu \; P_1\left(\mu\right) \left[\frac{1}{2}\phi_0(x_L) + \frac{3}{2}\phi_1(x_L)\right] \\ &= \frac{1}{4}\phi_0(x_L) - \frac{1}{2}\;D\frac{d\phi_0(x_L)}{dx}, \end{aligned} \tag{4.16}$$

we obtain the equations which, using the Fick's law, can be rewritten as

$$D\left(\Gamma\right)\frac{\mathrm{d}\phi_0}{\mathrm{d}x}\left(\Gamma\right) = n\phi_0\left(\Gamma\right), \qquad n = \left\{ \begin{array}{ll} -1 & \text{if } \Gamma = 0 \\ +1 & \text{if } \Gamma = x_L \end{array} \right., \qquad \Gamma = 0,\ x_L \tag{4.17}$$

where Γ is the boundary of the slab and n is the normal directions of the boundary. Using another coefficients in equation (4.17), other boundary conditions can be included as zero-flux, zero-current and fixed albedo conditions.

When the prescribed incident current, $J_{in}^{+} = 0$, the vacuum boundary condition for diffusion theory can be constructed from a geometrical interpretation of the ratio of the flux gradient to the flux in this equation to obtain the condition that the extrapolated flux vanishes a distance λ_{ex} outside the boundary:

$$\phi(x_L - \lambda_{ex}) = 0, \quad \lambda_{ex} = \frac{2}{3\Sigma_{tr}} = \frac{2}{3}\lambda_{tr} \tag{4.18}$$

4.1.3 P_3 equations

If we set $N = 3$ in Equation (4.6), the P_3 approximation equations are

$$\frac{d\phi_1}{dx} + \Sigma_a\phi_0 = \frac{1}{\lambda}\nu\Sigma_f\phi_0, \tag{4.19a}$$

$$\frac{d\phi_0}{dx} + 2\frac{d\phi_2}{dx} + 3(\Sigma_t - \Sigma_{s1})\phi_1 = 0, \tag{4.19b}$$

$$2\frac{d\phi_1}{dx} + 3\frac{d\phi_3}{dx} + 5(\Sigma_t - \Sigma_{s_2})\phi_2 = 0, \tag{4.19c}$$

$$3\frac{d\phi_2}{dx} + 7(\Sigma_t - \Sigma_{s3})\phi_3 = 0. \tag{4.19d}$$

From equation(4.19b) and (4.19d) we get the flux moments

$$\begin{aligned} \phi_1 &= -\frac{1}{3(\Sigma_t - \Sigma_{s_1})}\frac{d}{dx}\left(\phi_0 + 2\phi_2\right), \\ \phi_3 &= -\frac{3}{7(\Sigma_t - \Sigma_{s_3})}\frac{d\phi_2}{dx}. \end{aligned} \tag{4.20}$$

Considering the change of variables,

$$F_0 = \phi_0 + 2\phi_2, \qquad F_1 = \phi_2, \tag{4.21}$$

the P_3 approximation can be expressed as

$$\phi_1 = -D_0\frac{\mathrm{d}F_0}{\mathrm{d}x}, \qquad \phi_3 = -D_1\frac{\mathrm{d}F_1}{\mathrm{d}x}, \tag{4.22}$$

$$-\frac{\mathrm{d}}{\mathrm{d}x}\left(D_0\frac{\mathrm{d}F_0}{\mathrm{d}x}\right) + \Sigma_a(F_0 - 2F_1) = \frac{1}{\lambda}\nu\Sigma_f(F_0 - 2F_1), \tag{4.23}$$

$$-2\Sigma_a F_0 - 3\frac{\mathrm{d}}{\mathrm{d}x}\left(D_1\frac{\mathrm{d}F_1}{\mathrm{d}x}\right) + \left(4\Sigma_a + 5\left(\Sigma_t - \Sigma_{s_2}\right)\right)F_1 = \frac{1}{\lambda}\nu\Sigma_f(-2F_0 + 4F_1), \tag{4.24}$$

where the diffusion coefficients are defined as

$$D_0 = \frac{1}{3(\Sigma_t - \Sigma_{s1})} \quad , \qquad D_1 = \frac{3}{7(\Sigma_t - \Sigma_{s3})}. \tag{4.25}$$

Equation (4.23) and equation (4.24) are the diffusive form of the SP_3 equations. The vacuum Marshak's boundary conditions of equation (4.7) can be rewritten as

$$\begin{aligned} n\,D_0\left(\Gamma\right)\frac{\mathrm{d}F_0}{\mathrm{d}x}\left(\Gamma\right) &= \frac{1}{2}F_0\left(\Gamma\right)-\frac{3}{8}F_1\left(\Gamma\right), \\ n\,D_1\left(\Gamma\right)\frac{\mathrm{d}F_1}{\mathrm{d}x}\left(\Gamma\right) &= -\frac{1}{8}F_0\left(\Gamma\right)+\frac{7}{8}F_1\left(\Gamma\right). \end{aligned} \tag{4.26}$$

4.1.4 P_5 equations

If we set $N = 5$ in equation (4.6)

$$\frac{d\phi_1}{dx}+\Sigma_a\phi_0=\frac{1}{\lambda}\nu\Sigma_f\phi_0, \tag{4.27a}$$

$$2\frac{d\phi_2}{dx}+\frac{d\phi_0}{dx}+3(\Sigma_t-\Sigma_{s1})\phi_1,=0 \tag{4.27b}$$

$$3\frac{d\phi_3}{dx}+2\frac{d\phi_1}{dx}+5(\Sigma_t-\Sigma_{s_2})\phi_2,=0 \tag{4.27c}$$

$$4\frac{d\phi_4}{dx}+3\frac{d\phi_2}{dx}+7(\Sigma_t-\Sigma_{s_3})\phi_3,=0 \tag{4.27d}$$

$$5\frac{d\phi_5}{dx}+4\frac{d\phi_3}{dx}+9(\Sigma_t-\Sigma_{s_4})\phi_4,=0 \tag{4.27e}$$

$$5\frac{d\phi_4}{dx}+11(\Sigma_t-\Sigma_{s_5})\phi_5=0. \tag{4.27f}$$

Equations(4.27a), (4.27b), (4.27c), (4.27d) and (4.27e) include only flux moments and the equations (4.27b),(4.27d) and (4.27f) yield for the odd flux moments

$$\begin{aligned} \phi_1 &= -\frac{1}{3(\Sigma_t-\Sigma_{s_1})}\frac{d}{dx}\left(\phi_0+2\phi_2\right), \\ \phi_3 &= -\frac{3}{7(\Sigma_t-\Sigma_{s_3})}\frac{d}{dx}\left(\phi_2+\frac{3}{4}\phi_4\right), \\ \phi_5 &= -\frac{5}{(11\Sigma_t-\Sigma_{s_5})}\frac{d\phi_4}{dx}. \end{aligned} \tag{4.28}$$

Considering the redefinitions,

$$F_0=\phi_0+2\phi_2,\qquad F_1=\phi_2+\frac{4}{3}\phi_4,\qquad F_2=\frac{1}{3}\phi_4, \tag{4.29}$$

The P_5 equations can be expressed as

$$\phi_1=-D_0\frac{\mathrm{d}F_0}{\mathrm{d}x}\quad,\quad\phi_3=-D_1\frac{\mathrm{d}F_1}{\mathrm{d}x}\quad,\quad\phi_5=-D_2\frac{\mathrm{d}F_2}{\mathrm{d}x}, \tag{4.30}$$

$$-\frac{\mathrm{d}}{\mathrm{d}x}\left(\frac{\mathrm{d}F_0}{\mathrm{d}x}\right)+\Sigma_a F_0-2\Sigma_a F_1+8\Sigma_a F_2=\frac{1}{\lambda}\nu\Sigma_f(F_0-2F_1+8F_2), \tag{4.31}$$

$$\begin{aligned}-2\Sigma_a F_0-3\frac{\mathrm{d}}{\mathrm{d}x}\left(D_1\frac{\mathrm{d}F_1}{\mathrm{d}x}\right)+(4\Sigma_a+5(\Sigma_t-\Sigma_{s_2}))F_1-(20(\Sigma_t-\Sigma_{s_2})+16\Sigma_a)F_2)\\ =\frac{1}{\lambda}\nu\Sigma_f(-2F_0+4F_1-16F_2),\end{aligned} \tag{4.32}$$

$$\begin{aligned}-8\Sigma_a F_0-(20(\Sigma_t-\Sigma_{s_2})+16\Sigma_a)F_1-15\frac{\mathrm{d}}{\mathrm{d}x}\left(D_2\frac{\mathrm{d}F_2}{\mathrm{d}x}\right)+(81(\Sigma_t-\Sigma_{s4})\\ +80(\Sigma_t-\Sigma_{s_2})+64\Sigma_a)F_2=\frac{1}{\lambda}\nu\Sigma_f(8F_0-16F_1-64F_2),\end{aligned} \tag{4.33}$$

where the diffusion coefficients are

$$D_0=\frac{1}{3\left(\Sigma_t-\Sigma_{s1}\right)},\qquad D_1=\frac{3}{7\left(\Sigma_t-\Sigma_{s3}\right)},\qquad D_2=\frac{15}{11\left(\Sigma_t-\Sigma_{s5}\right)}. \tag{4.34}$$

Equations (4.32) and (4.33) are the diffusive form of the SP_3 equations. The vacuum Marshak's boundary conditions of Equation (4.7) can be rewritten as

$$\begin{aligned}n\,D_0\left(\Gamma\right)\frac{\mathrm{d}F_0}{\mathrm{d}x}\left(\Gamma\right)&=\frac{1}{2}F_0\left(\Gamma\right)-\frac{3}{8}F_1\left(\Gamma\right)+\frac{15}{16}F_2\left(\Gamma\right),\\ n\,D_1\left(\Gamma\right)\frac{\mathrm{d}F_1}{\mathrm{d}x}\left(\Gamma\right)&=-\frac{1}{8}F_0\left(\Gamma\right)+\frac{7}{8}F_1\left(\Gamma\right)-\frac{205}{128}F_2\left(\Gamma\right),\\ n\,D_2\left(\Gamma\right)\frac{\mathrm{d}F_2}{\mathrm{d}x}\left(\Gamma\right)&=\frac{1}{16}F_0\left(\Gamma\right)-\frac{41}{128}F_1\left(\Gamma\right)+\frac{407}{128}F_2\left(\Gamma\right).\end{aligned} \tag{4.35}$$

4.2 Simplified P_N equations

The SP_N equations have been derived in three ways [120] (i) by a formal procedure, in which they are hypothesized as multi-dimensional generalizations of the 1-D P_N equations, (ii) by an asymptotic analysis, in which they are shown to be asymptotic corrections to diffusion theory, and (iii) by a variational analysis. The first (formal) approach was historically the first to be proposed, in the early 1960's [34]. This approach is relatively simple, but is theoretically weak. The second (asymptotic) approach was developed in the 1990's [121]; this is much more theoretically convincing, but it only leads to the basic SP_N equations without boundary conditions (the boundary conditions must be hypothesized). The third (variational) approach was also developed in the 1990's [32, 122]; this yields both the SP_N equations and their boundary conditions. Unfortunately, from the algebraic viewpoint, the variational derivation is exceedingly complicated.

4.2.1 SP_3 equations

Let the one-dimensional P_3 equations in first-order form equations (4.19) be the starting point. Inserting equation (4.20) in equation (4.19a), (4.19c) and taking into account the diffusion coefficients (4.25) and the redefinitions (4.21). The four first-order differential equations can be replaced by the two second-order differential equations for the 0^{th} and 2^{nd} flux moments.

In 1960's Gelbrad [34] proposed the SP_3 equations for general three-dimensional geometry by replacing the second derivatives in the one-group P_3 equations for one-dimensional geometry $\frac{d^2}{dx^2}$ by the Laplace operator $\vec{\nabla}^2$. Applying this approach in equations (4.23), (4.24) and rearranging terms of this equations yield the corresponding SP_3 equations for three-dimensional geometry:

$$\begin{aligned} &-\vec{\nabla}(D_0\vec{\nabla}F_0)+\Sigma_a(F_0-2F_1)=\frac{1}{\lambda}\nu\Sigma_f(F_0-2F_1),\\ &-3\vec{\nabla}(D_1\vec{\nabla}F_1)+(4\Sigma_a+5(\Sigma_t-\Sigma_{s_2}))F_1-2\Sigma_aF_0\\ &=\frac{1}{\lambda}\nu\Sigma_f(-2F_0+4F_1). \end{aligned} \tag{4.36}$$

The SP_3 trial function given by equations (4.36) is a generalization of equations (4.23) and (4.24) in the following sense. If the multidimensional transport solution behaves in a locally one-dimensional manner at each point r in space, then equation (4.36) reduces to equations (4.23) and (4.24) without approximation, where x in equations (4.23, 4.24) is the direction in which the multidimensional solution varies. Thus, equations (4.23) and (4.24) are the P_3 approximation for a one-dimensional transport solution with the variation only in the x-direction; equation (4.36) is the generalization of equations (4.23) and (4.24) for a multidimensional transport solution having one-dimensional variation in an arbitrary direction.

To obtain solutions to the SP_3 and diffusion equations, boundary conditions have to be defined. As these equations are furthermore not defined at interfaces where cross sections are discontinuous, also interface conditions are required. Brantley and Larsen's variational derivation of the SP_3 equations provides in addition to the equations (4.36) the interface and Marshak-like boundary conditions [32]. At the interface r_{ij} between the two volumes i and j the following conditions are obtained

$$F^i_m(r_{ij})=F^j_m(r_{ij}) \qquad \text{and} \qquad n_iJ^i_m(r_{ij})=n_iJ^j_m(r_{ij}) \tag{4.37}$$

where n_i is the unit outer normal vector of material zone i and with

$$J^j_m(r)=-D^i_m\vec{\nabla}F^i_m \qquad \text{for} \qquad m=0,2 \tag{4.38}$$

In the case of an outer boundary, the Marshak-like boundary conditions (4.9) are used to obtain the solution. As we did before, substitute the Legendre Polynomial (4.2), using the the odd-order flux moments (equation (4.20)) and the diffusion coefficient (equation (4.25)), we get the incoming and outgoing "partial currents" at any surface r_{ij} of a volume

$$\begin{aligned} J_0^{\pm}(r_{ij}) &= \frac{1}{4}F_0^i(r_{ij}) \pm \frac{1}{2}J_0^i(r_{ij}) - \frac{3}{16}F_2^i(r_{ij}) \\ J_2^{\pm}(r_{ij}) &= \frac{3}{80}F_0^i(r_{ij}) \pm \frac{1}{2}J_2^i(r_{ij}) - \frac{21}{80}F_2^i(r_{ij}) \end{aligned} \tag{4.39}$$

If there is reflexive at any outer surface r_{out} of the system, the boundary conditions are given by

$$J_m^-(r_{out}) = 0, \qquad m = 0, 2. \tag{4.40}$$

4.2.2 SP_5 equations

If we set $N = 5$ in equation (4.6) a s we did before, let the one-dimensional P_5 equations in first-order form (4.31), (4.32) and (4.33) be the starting point.

In the formal derivation of the three-dimensional SP_N equations, one simply takes the one-dimensional P_N equations and replaces each $1D$ diffusion operator by its $3D$ counterpart. That is, we replace:

$$-\frac{\mathrm{d}}{\mathrm{d}x}\left(\frac{\mathrm{d}F_m}{\mathrm{d}x}\right) = -\vec{\nabla}^2 F_m, \qquad m = 1, 2, 3 \tag{4.41}$$

Thus, equation (4.31), (4.32) and (4.33) become:

$$-\vec{\nabla}(D_0\vec{\nabla}F_0) + \Sigma_a F_0 - 2F_1 + 8\Sigma_a F_2 = \frac{1}{\lambda}\nu\Sigma_f(F_0 - 2F_1 + 8F_2), \tag{4.42}$$

$$\begin{aligned} -3\vec{\nabla}(D_1\vec{\nabla}F_1) - 2\Sigma_a F_0 &+ (4\Sigma_a + 5(\Sigma_t - \Sigma_{s_2}))F_1 \\ &- (20(\Sigma_t - \Sigma_{s_2}) + 16\Sigma_a)F_2 \\ &= \frac{1}{\lambda}\nu\Sigma_f(-2F_0 + 4F_1 - 16F_2), \end{aligned} \tag{4.43}$$

$$\begin{aligned} -8\Sigma_a F_0 - (20(\Sigma_t - \Sigma_{s_2}) &+ 16\Sigma_a)F_1 - 15D_2\vec{\nabla}^2 F_2 \\ &+ (81(\Sigma_t - \Sigma_{s4}) + 80(\Sigma_t - \Sigma_{s_2}) + 64\Sigma_a)F_2 \\ &= \frac{1}{\lambda}\nu\Sigma_f(8F_0 - 16F_1 - 64F_2) \end{aligned} \tag{4.44}$$

A similar approach to the one used for the SP_3 equations gives the boundary conditions for the vaccum and reflective condition.

4.2.3 Finite elemet discretization

As it was reviewed in the last section the SP_N consist of a set of diffusion-like equations for which simultaneous solutions for the unknown fluxes moments are required. Thus FEM discretizations that were developed for the diffusion equation can be applied without major changes. A Galerkin finite element discretization has been applied to equation (4.36) leading to an algebraic generalized eigenvalue problem of the form,

$$\begin{pmatrix} L_{00} & L_{01} \\ -L_{01}^T & L_{11} \end{pmatrix} \begin{pmatrix} \tilde{F}_0 \\ \tilde{F}_1 \end{pmatrix} = \frac{1}{\lambda} \begin{pmatrix} M_{00} & M_{01} \\ M_{01}^T & M_{11} \end{pmatrix} \begin{pmatrix} \tilde{F}_0 \\ \tilde{F}_1 \end{pmatrix} , \tag{4.45}$$

where the matrix elements are given by

$$\begin{aligned} (L_{00})_{ij} = \sum_{e=1}^{N_t} \Bigg(& D_0 \int_{\Omega_e} \vec{\nabla} N_i \vec{\nabla} N_j \, \mathrm{d}V - D_0 \int_{\Gamma_e} N_i \vec{\nabla} N_j \, \mathrm{d}\vec{S} \\ & + (\Sigma_a) \int_{\Omega_e} N_i N_j \, \mathrm{d}V \Bigg) , \end{aligned} \tag{4.46a}$$

$$(L_{01})_{ij} = \sum_{e=1}^{N_t} \left(-2\Sigma_a \int_{\Omega_e} N_i N_j \, \mathrm{d}V \right) , \tag{4.46b}$$

$$\begin{aligned} (L_{11})_{ij} = \sum_{e=1}^{N_t} \Bigg(& -3D_1 \int_{\Omega_e} \vec{\nabla} N_i \vec{\nabla} N_j \, \mathrm{d}V + 3D_1 \int_{\Gamma_e} N_i \vec{\nabla} N_j \, \mathrm{d}\vec{S} \\ & + (4\Sigma_a + 5(\Sigma_t - \Sigma_{s_2}))\Sigma_{a2} \int_{\Omega_e} N_i N_j \, \mathrm{d}V \Bigg) , \end{aligned} \tag{4.46c}$$

$$(M_{00})_{ij} = \sum_{e=1}^{N_t} \left(\nu\Sigma_f \int_{\Omega_e} N_i N_j \, \mathrm{d}V \right) , \tag{4.46d}$$

$$(M_{01})_{ij} = \sum_{e=1}^{N_t} \left(-2\nu\Sigma_f \int_{\Omega_e} N_i N_j \, \mathrm{d}V \right) , \tag{4.46e}$$

$$(M_{11})_{ij} = \sum_{e=1}^{N_t} \left(4\nu\Sigma_f \int_{\Omega_e} N_i N_j \, \mathrm{d}V \right) , \tag{4.46f}$$

where N_i is the prescribed shape function for the $i - th$ node. For simplicity, the shape functions used are part of Lagrange finite elements.Ω_e , k = 1,..., N_t, are the reactor subdomains (cells) in which the reactor domain is divided. In the same way,Γ_e is the set of the corresponding subdomain surfaces which are part of the reactor boundary.

For simplicity all derivation are done assuming one neutron energy group, even though the code implemented and the numerical results presented admit a multi-group formulation.

To solve the algebraic eigenvalue problem a Krylov-Schur method is used from the SLEPc library. Finally, the solution fluxes must be normalized using some arbitrary criteria as all eigenvalue problems. usually it is forced that the average neutronic power is equal to 1.

$$\frac{1}{V}\int P \mathrm{d}V = \frac{1}{V}\int \sum_{g=1}^{G} \Sigma_{fg}\phi_{0g}\ \mathrm{d}V = 1. \tag{4.47}$$

A similar formulation is used for the SP_5 equations.

4.3 Numerical results

The performance of the simplified SP_N $(N = 1, 3, 5)$ approximations has been tested for different problems presented in Chapter2. Firstly, we tested the $1D$ case using two problems in slab geometry, a homogeneous one-group and isotropic scattering eigenvalue problem (section 2.3.1), which can be solved analytically, then a heterogeneous one with anisotropic scattering. Secondly, we treated a more realistic problems, a two dimensional VVER-1000 reactor (section 2.3.5) problem, a small hexagonal reactor (section 3.4.2) and the three dimensional VVER-440 problem (section 2.3.8) have been tested to show the performance in 2D and 3D problems.

We compared the results obtained for the homogeneous one-group problem with the nodal collocation method to results from the discrete-ordinates code ONEDANT [123], which solves the transport problem using a very fine spatial mesh and an angular S_N quadrature set. While for the other problems, we compared the results obtained for the P_1, P_3 and P_5 approximations to each other.

4.3.1 Homogeneous slab

We first consider a homogeneous slab 2 *cm* thick which has been reported before in section 2.3.1 and has the nuclear cross sections : $D = \frac{1}{3}$, $\Sigma_s = 0.9$, and $\nu\Sigma_f = 0.25$. This problem has been selected to show the bad behaviour of the P_1 (diffusion) approximation for systems with a strong spatial variation of the neutronic flux.

Table 4.1 shows the fundamental eigenvalue and those corresponding to the subcritical modes obtained for the P_1, P_3 and P_5 approximations compared to the analytical values of the homogeneous slab. The first eigenvalues $\mathrm{k_{eff}}$ obtained using the P_N approximations are compared with the S_N result from the discrete-ordinates code ONEDANT [123]. The angular quadrature for the ONEDANT runs was S_{96} and the result obtained using number of refinement cycle $=$ 1 and a polynomial degree p= 3 in the finite element expansion. The calculation performed with ONEDANT is a very good approximation to the transport equation using the discrete-ordinates method, but the computational cost of this method is very high to be used in more realistic problems [119].

Figure 4.1 shows the normalized scalar flux from the ONEDANT reference solution, versus P_N solutions with $(N = 1, 3, 5)$ obtained for the P_1, P_3 and P_5 approximations. We can note that for the fundamental mode the P_N calculations follow the reference solution. However, the P_3 and P_5 curves are closer to the reference transport curve than the P_1 one. As it was expected, the P_5 approximation is the most accurate, and we can also conclude that the diffusion approximation is not very adequate to study this problem.

Figure 4.3 shows the eigenvectors obtained for the second, third and fourth subcritical modes using the P_1, P_3 and P_5 approximations.

Table 4.1: P_N compared to the analytical values of the first four eigenvalues for a homogeneous slab 2 *cm* thick.

Eigenvalue	**Analytical Solution**			**Numerical Result**		
	P_1	P_3	P_5	P_1	P_3	P_5
$\mathrm{k_{eff}}$	0.587489	0.652956	0.660523	0.5874890	0.6529562	0.6605229
2nd	0.149135	0.207745	0.223379	0.1491351	0.2077446	0.2233791
3rd	0.058380	0.096091	0.113889	0.0583796	0.0960912	0.0113888
4th	0.029602	0.053122	0.068040	0.0296016	0.0531219	0.0680403
ONEDANT (1st)	0.662951					

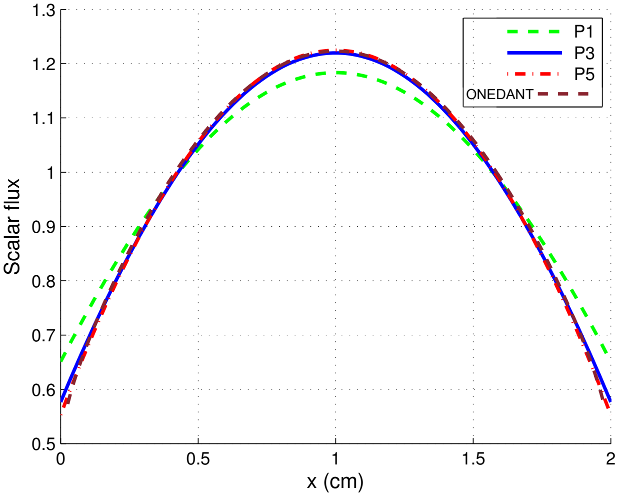

Figure 4.1: Normalized scalar fluxes for the homogeneous $2\,cm$ slab.

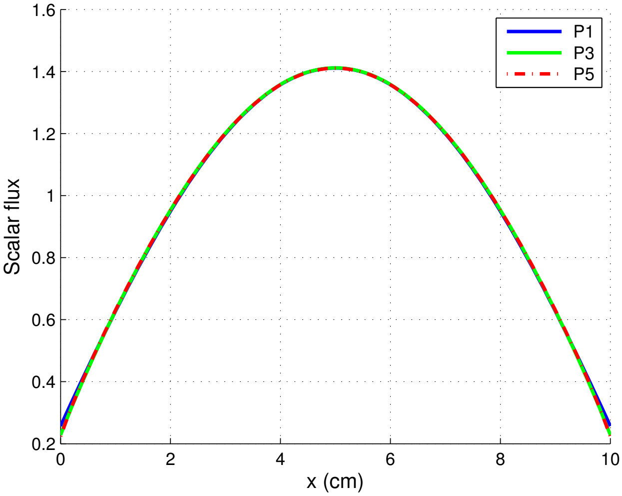

Figure 4.2: Normalized scalar fluxes for the homogeneous $10\,cm$ slab.

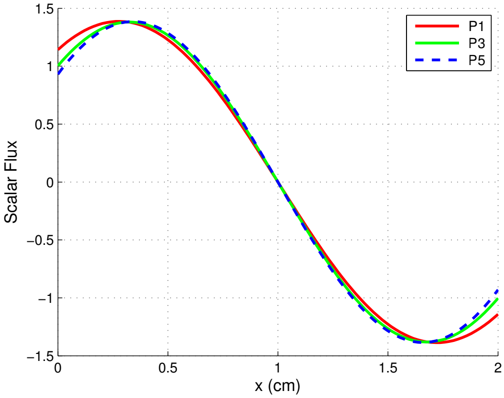

(a) 2nd subcritical Mode

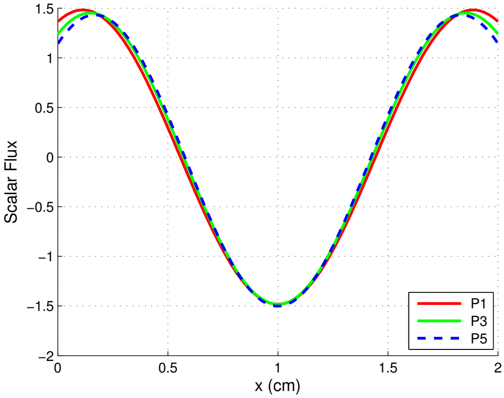

(b) 3rd subcritical Mode

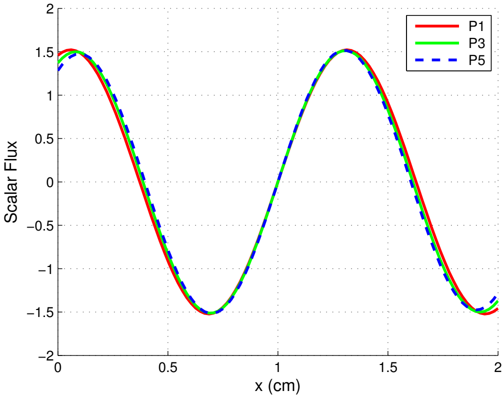

(c) 4th subcritical Mode

Figure 4.3: Eigenvectors for the subcritical modes of the homogeneous slab $2\,cm$ thick.

We conclude also that the P_5 approximation is superior to the P_3 one, and that the P_1 approximation results show a large error. Increasing the length of the slab increases the accuracy of the P_N solutions as shown in Figure 4.2, which has been obtained from a more realistic problem used a seven-region slab with 10 cm length [119]. This result can be expected, since the leakage from the slab also decreases when the slab becomes larger, and the problem becomes more diffusive.

4.3.2 Heterogeneous slab

We consider now a more "realistic" system corresponding to a seven-region slab 18 cm thick, with vacuum boundary conditions for the leftmost and rightmost faces, and discontinuous fission and total cross-sections. This problem is a slight modification of a problem presented in [124]. The system is comprised of a combination of fuel and no fuel regions, as shown in Figure 4.4. The cross-sections for these materials are shown in 4.2.

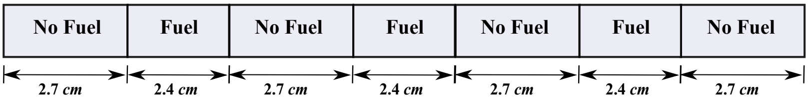

Figure 4.4: Seven-region slab disposition.

Table 4.2: Seven-region cross sections.

Material	$\nu\Sigma_f(\,cm^{-1})$	$\Sigma_s(\,cm^{-1})$	$\Sigma_t(\,cm^{-1})$
Fuel	0.178	0.334	0.416667
No fuel	0.0	0.334	0.370370

Table 4.3 shows the three dominant eigenvalues for the P_N approximations with ($N = 1, 3, 5$). The result obtained using number of refinement cycle = 1 and a polynomial degree = 3 in the finite element expansion. Also we have included the result obtained for k$_{\text{eff}}$calculation from ONEDANT, using an angular quadrature order of S_{96}, with 500 fine mesh cells in each region and a convergence criterion of $epsi = 10^{-6}$.

Table 4.3: Four dominant eigenvalue for the seven-region slab 18 *cm* thick.

Eigenvalue	P_1	P_3	P_5	ONEDANT
k_{eff}	1.113872	1.148744	1.157360	1.16224
2nd	0.6586507	0.7350364	0.7466179	
3rd	0.4239442	0.5276454	0.5419515	
4th	0.1092353	0.1653045	0.1881475	

In Figure 4.5 we plot the normalized scalar flux for this problem computed with the high order finite element method for the P_1, P_3 and P_5 approximations. While Figure 4.6 shows the normalized second, third and fourth eigenvectors obtained. As with the homogeneous problem, the P_3 and P_5 results remain more accurate than the P_1 result.

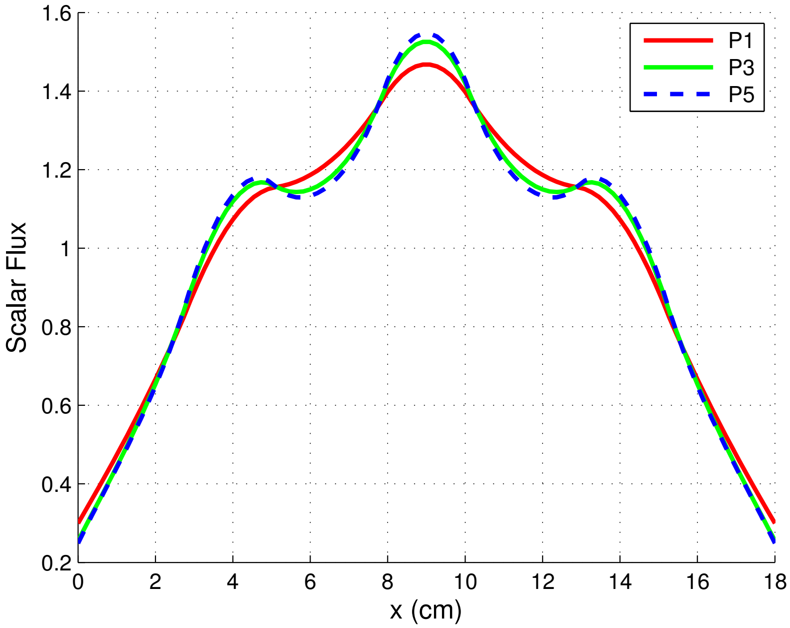

Figure 4.5: Normalized scalar fluxes for the heterogeneous slab.

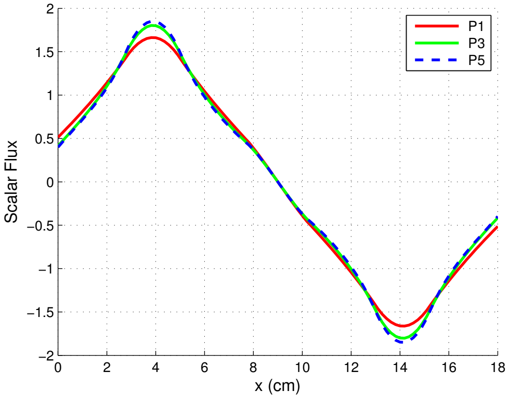

(a) 2nd subcritical Mode

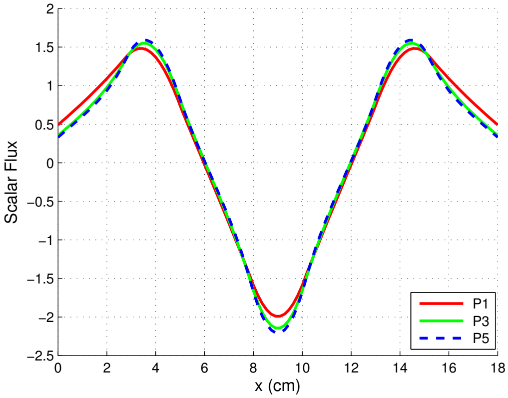

(b) 3rd subcritical Mode

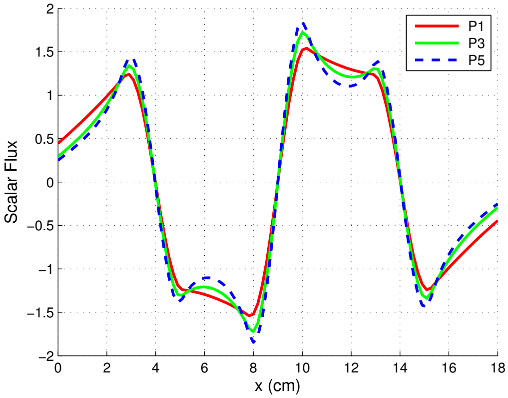

(c) 4th subcritical Mode

Figure 4.6: Eigenvectors for the subcritical modes of the heterogeneous slab.

4.3.3 Small reactor

To study the performance of the SP_N approximation in the three dimensional reactors, a small reactor which has been described before in (section 3.4.2) will be studied using the SP_1, SP_3 and SP_5 approximations.

The obtained results for the dominant eigenvalue $\mathrm{k_{eff}}$ using SP_1, SP_3 and SP_5 approximations are shown in Table 4.4. The result obtained using zero refinement cycle and a polynomial degree $p = 3$ in the finite element expansion. In this Table, also the number of degrees of freedom (DoF) are shown for the reduced eigenvalue problem in order to have an idea of the size of the problem solved. Also the mean relative and maximum relative difference per cell for the neutronic power between both SP_1, SP_3 approximation and SP_5 approximation are shown for the initial configuration for the reactor. Figure 4.7 shows the axial power distribution of the reactor for several calculations. First, the power distribution has been computed for the SP_N approximation ($N = 1, 3, 5$) using 12 axial planes. As SP_5 approximation is the most accurate one, we compared it with SP_1, SP_3 results. The difference in neutronic power distribution between both SP_1, SP_3 approximation and SP_5 approximation are shown also in Figure 4.8. This difference can be expressed as

$$\bar{\delta} = \frac{1}{N_e} \sum_{e=1}^{N_t} \left(\frac{P_{e,SP_N} - P_{e,Ref}}{P_{e,Ref}} \right) \tag{4.48}$$

$$\delta_{max} = \max\,(P_{e,SP_N} - P_{e,Ref}) \tag{4.49}$$

Where P_{SP_N} is the computed power calculated by SP_3 or SP_5 approximation while P_{Ref} is the computed power calculated by SP_5.

Table 4.4: Eigenvalue results and power distribution difference with respect to SP_5 for the Small Reactor reactor.

	DoF	$\mathbf{k_{eff}}$	$\mathbf{\Delta k_{eff}}$ (*pcm*)	**Power** $\bar{\delta}$ (%)	$\delta_{\max}$(%)
SP_1	41366	0.8160415	265.8	2.014	1.861
SP_3	82732	0.8186731	2.65	0.014287	0.1005
SP_5	124098	0.8186996			

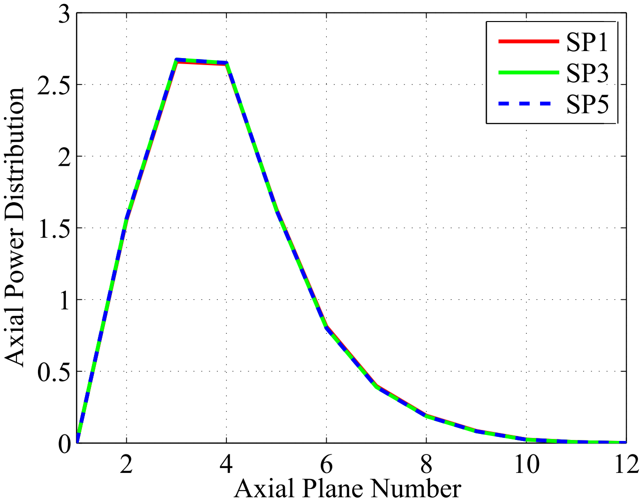

Figure 4.7: Axial power evaluation for the small reactor.

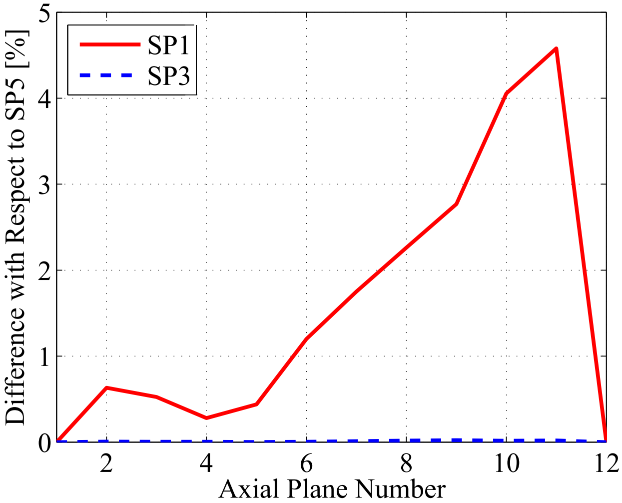

Figure 4.8: SP_1 and SP_3 axial power difference with respect to SP_5 for the small reactor.

We can note that the results demonstrate a near perfect match. The difference in the axial power doesn't exceed 5% in the case of the diffusion and the difference between the SP_3 and the SP_5 is very small which mean that the SP_3 is sufficient. Figure 4.9 shows the power difference for both SP_1 and SP_3 relative to SP_5 on each hexagon. The difference in the case of the diffusion doesn't exceed 0.28% and 0.02% for the SP_3 approximation.

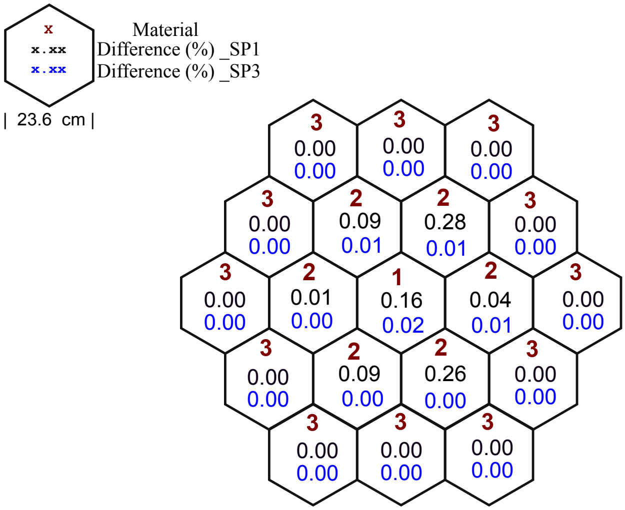

Figure 4.9: Difference in neutronic power distribution for SP_1 and SP_3 with respect to SP_5 in the small reactor.

4.3.4 Two dimensional VVER-1000 reactor

The VVER-100 reactor has been described before in (section 2.3.5). This reactor is a two dimensional reactor composed by 163 assemblies of pitch equal to 23.60 cm.

Table 4.5 shows the results obtained for the dominant eigenvalue $\mathrm{k_{eff}}$ using SP_1, SP_3 and SP_5 approximation and the mean relative and maximum relative difference for the neutronic power between both SP_1, SP_3 approximation and the SP_5 approximation. The result obtained using zero refinement cycle and a polynomial degree $p=3$ in the finite element expansion.

In Table 4.6 the results obtained for the first three subcritical eigenvalues are presented using SP_1, SP_3 and SP_5 approximation. The difference in neutronic power distribution between both SP_1, SP_3 approximation and SP_5 approximation are shown also in Figure 4.10.

Table 4.5: Eigenvalue results and power distribution difference with respect to SP_5 for the VVER-1000 2D reactor.

	DoF	$\mathbf{k_{eff}}$	$\mathbf{\Delta k_{eff}}$ (*pcm*)	**Power** $\bar{\delta}$ (%)	δmax(%)
SP_1	9074	1.00645	61.5	1.2539	2.2248
SP_3	18148	1.00705	1.4	0.04951	0.0663
SP_5	27222	1.00707			

Table 4.6: First 3 subcritical eigenvalues for the VVER-1000 2D reactor.

	λ_2	λ_3	λ_4
SP_1	0.9948101	0.9948101	0.9737631
SP_3	0.9955893	0.9955893	0.9749211
SP_5	0.9956090	0.9956090	0.9749494

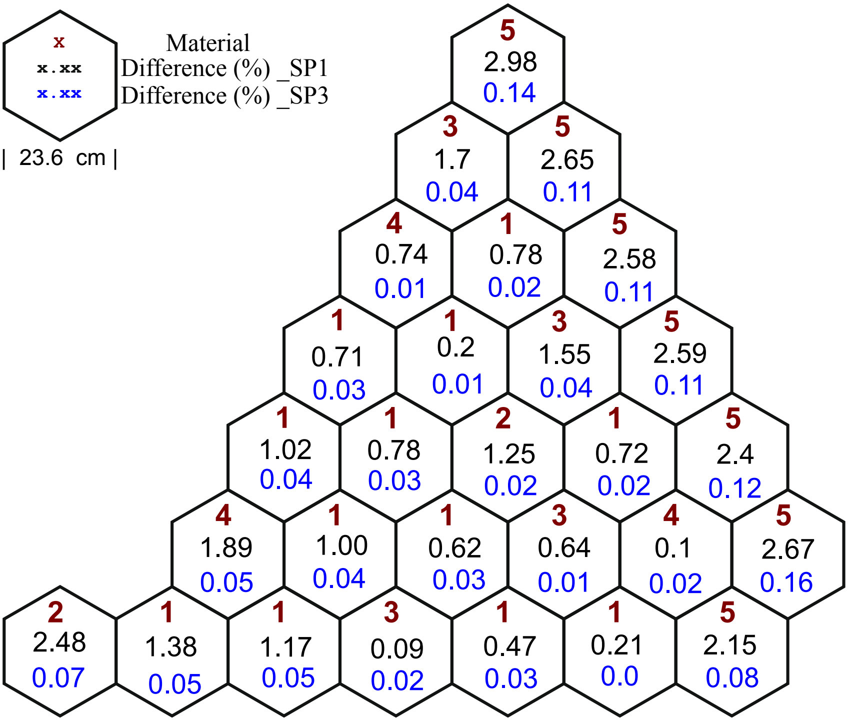

Figure 4.10: Difference in neutronic power distribution for SP_1 and SP_3 with respect to SP_5 in the VVER-1000 2D reactor.

4.3.5 Three dimensional VVER-440 reactor

As we did before for the small reactor problem. The performance of the SP_N approximation for the three dimensional VVER-440 reactor has been studied. This reactor has been described before in (section 2.3.8).

Table 4.7 shows the results obtained for the dominant eigenvalue k_{eff} using SP_1, SP_3 and SP_5 approximations. The result obtained using zero refinement cycle and a polynomial degree $p=3$ in the finite element expansion. The number of degrees of freedom (DoF) are shown and the mean relative and maximum relative difference for the axial power between both SP_1, SP_3 approximation and SP_5 approximation are shown for the reactor configuration.

Figure 4.11 shows the axial power distribution for the SP_N approximation ($N = 1, 3, 5$) in the three dimensional VVER-440 reactor. We can note that the results demonstrate a near perfect match. The difference in neutronic power distribution between both SP_1, SP_3 , approximation and SP_5 approximation are shown also in Figure 4.12. The difference in neutronic power distribution in the the sixth plane between both SP_1, SP_3 approximation and SP_5 approximation are shown also in figure 4.13.

Table 4.7: Eigenvalue results and power distribution difference with respect to SP_5 for the VVER-440-3D reactor.

	DoF	$\mathbf{k_{eff}}$	$\mathbf{\Delta k_{eff}}$	**Power**	
			(*pcm*)	$\bar{\delta}$ (%)	δmax(%)
SP_1	857882	1.01138	127.1	2.1971	0.069568
SP_3	1715764	1.01261	3.8	0.058384	0.001632
SP_5	2573646	1.01265			

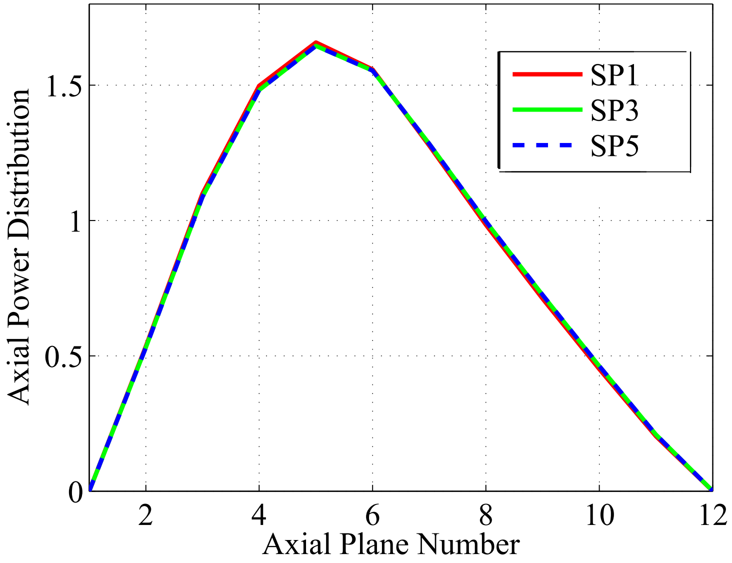

Figure 4.11: Axial power evaluation for the three dimensional VVER-440 reactor.

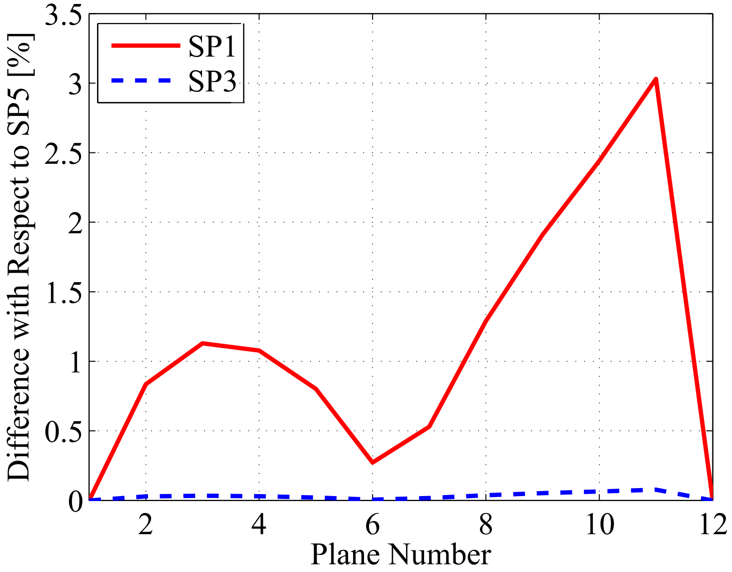

Figure 4.12: SP_1 and SP_3 axial power difference with respect to SP_5.

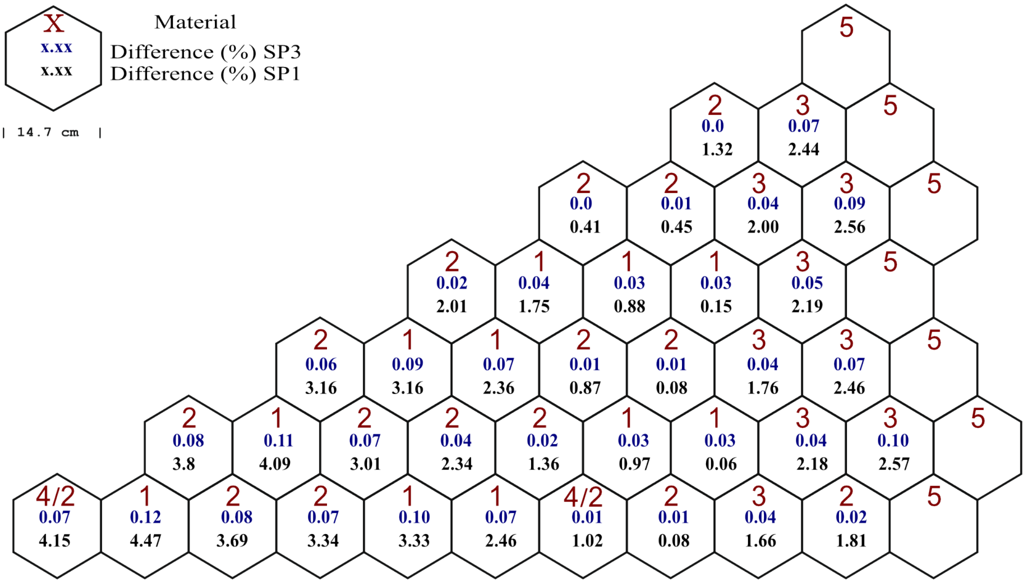

Figure 4.13: Difference in neutronic power distribution for SP_1 and SP_3 with respect to SP_5 in the VVER-1000 2D reactor.

Conclusions

The distribution of neutron population in nuclear reactor is described by using transport equations. One of possible approximations of neutron transport equation is given by the neutron diffusion equation. This work deals with this model for nuclear reactors with hexagonal geometries. First, the stationary neutron diffusion equation is studied. This is a differential eigenvalue problem, called Lambda Modes problem. To solve the Lambda Modes problem, an adaptive *h*-*p* finite element method has been implemented to approximate the solution of Lambda Modes problem of a nuclear reactor with hexagonal geometry. This method allows using high order finite elements with heterogeneous meshes, and leads to different refinements such as *h*-refinement and *p*-refinement. In this way, to increase the accuracy of the solution it is possible both to refine the spatial mesh and to increase the degree of the polynomials in the finite element method. This method is based on splitting each one of the rectangular prisms defied by the geometry into three equilateral rectangular prisms, obtaining a mesh which is kept fixed.

To study the performance of the method to compute the dominant eigenvalues and their corresponding eigenvectors of a nuclear power reactor, different benchmark problems have been analysed, using different meshes and configurations of the computations. An extensive analysis of 1D and 2D benchmark reactor cores has been carried out. In all the studied reactors the *h*-*p* FEM has provided good results for the ($\mathbf{k}_{\text{eff}}$) and the neutron power distribution. Also, the three-dimensional VVER-440 Reactor have been studied. The obtained results for the ($\mathbf{k}_{\text{eff}}$) and the neutronic power distribution have been compared with the reference solution obtained with the DIF3D code. From all the analyses performed is concluded that the method converges if the mesh is refined or the degree of the polynomial expansions is increased, being the last strategy the most convenient one to obtain accurate results with a moderate computational cost.

We propose two different *h*-*p*-refinement methods for the Lambda Modes problem of a nuclear power reactor. The first one is based in the material distribution inside the reactor that allows to define an heterogeneous mesh a priori. And the second one is based on a general error estimator that enables the code to refine the mesh in an automatic way.

The *h-p* finite element method used in this work has been implemented using the open source finite elements library deal.II [46]. With the help of the library, the code proposed is dimension independent and can manage different cell sizes and different types of finite elements [89]. In order to solve the resulting algebraic eigenvalue problem from the spatial discretization of the Lambda problem the SLEPc library [54] is used. As the deal.II library [46] doesn't support the hexahedra cells, the geometry is transformed to quadrilaterals with Gmsh [68] as mentioned before.

Once the solution for the steady state neutron distribution is obtained, it is used as initial condition for the time integration neutron diffusion equation. Many transients in nuclear power reactors involve the movement of the control rod banks, based on moving the control rods of the reactor, simulating an accident where a control rod is ejected and a scram is initialized to control the power evolution. For the simulation of this kind of transients with the classical methods, it is necessary to define equivalent material properties corresponding to partially inserted cells during the movement of the control rods. Volume averaged techniques are used to define this equivalent cross-sections, but this procedure leads to unphysical behaviour of some magnitudes during the simulation when a small number of axial planes are used in the spatial discretization and this problem is known as the rod cusping problem.

To avoid this problem, a new method based on a high-order finite element method is proposed. In this new method, the spatial mesh is moved together with the control rods in such a way that there is no partially inserted cells. The solutions of the physical magnitudes are transferred between different spatial meshes using a polynomial interpolation. To study the performance of the moving mesh scheme, a benchmark problem has been analysed. In these problems, a better performance of the moving mesh scheme than the traditional fixed mesh schemes when a small number of axial cells are used is shown. Thus, the moving mesh scheme permits to use a coarser discretization and reduce the computational effort.

Finally, as the usual approximation of the neutron transport equation by the multigroup neutron diffusion equation does not provide enough accurate results for complex fuel assemblies or fine mesh calculations. An *h-p* Finite Element Method is used to obtain the dominant Lambda mode associated with a configuration of a reactor core using the SP_N approximation. The performance of the SP_N (N= 1, 3, 5) approximations has been tested for different reactor benchmarks to compute the k_{eff} of the reactor and its corresponding stationary neutron flux. The work has been focused on the comparisons between the diffusion equation, SP_1, and the more sophisticated SP_3 and SP_5 equations. Firstly, two one dimensional problems were tested, a homogeneous one-group with isotropic scattering, which can be solved analytically, then a heterogeneous reactor with anisotropic scattering. Secondly, more a realistic problem was treated to show the performance in a three dimensional reactor. Firstly, two one-dimensional problems were tested, a homogeneous one-group and isotropic scattering eigenvalue problem , which can be solved analytically , then a heterogeneous one with anisotropic scattering. Secondly, more a realistic problem was treated to show the performance in 2D and 3D reactor. From these analyses performed is concluded that when diffusion approximation does not give enough accurate results SP_3 is a convenient, computational cheap alternative to improve performance. However, SP_5 approximation does not worth the extra computational effort to solve this approximation.

Bibliography

[1] S. Glasstone and A. Sesonske, “Nuclear reactor engineering”, *USA Chapman and Hall Puplic*, 1994.

[2] S. González-Pintor, D. Ginestar, and G. Verdú, “High order finite element method for the Lambda Modes problem on hexagonal geometry”, *Annals of Nuclear Energy*, vol. 36, no. 9, pp. 1450 –1462, 2009.

[3] S. González-Pintor, D. Ginestar, and G. Verdú, “Updating the Lambda Modes of a nuclear power reactor”, *Mathematical and Computer Modelling*, vol. 54, no. 7-8, pp. 1796–1801, 2011.

[4] S. González-Pintor, D. Ginestar, and G. Verdú, “Time integration of the neutron diffusion equation on hexagonal geometries”, *Mathematical and Computer Modelling*, vol. 52, no. 7, pp. 1203–1210, 2010.

[5] I. Babuska and W. Rheinboldt, “Error estimates for adaptive finite element computations”, *SIAM Numer. Annal.*, vol. 15, pp. 736–754, 1978.

[6] M. Ainsworth and J. Oden, “A posteriori error estimation in finite element analysis”, *Computer Methods in Applied Mechanics and Engineering*, vol. 142, pp. 1 –88, 1997.

[7] W. Bangerth and R. Rannacher, “Adaptive finite element methods for differential equations”, *Birkhäuser Verlag*, 2013.

[8] Y. Wang, M. Bangerth, and J. Ragusa, “Three-dimensional h-adaptivity for the multigroup neutron diffusion equations”, *Progr. Nucl. Energy*, 2009.

[9] P. Solin and L. Korous, “Adaptive higher-order finite element methods for transient PDE problems based on embedded higher-order implicit runge

kutta methods", *Journal of Computational Physics*, vol. 231, no. 4, pp. 1635 –1649, 2012.

[10] K. S. Smith, "Assembly homogenization techniques for light water reactor analysis", *Progress in Nuclear Energy*, vol. 17, no. 3, pp. 303–335, 1986.

[11] Y. Wang, "Hp-mesh adaptation for 1-D multigroup neutron diffusion problems", PhD thesis, Texas A&M University, 2007.

[12] G. Bilodeau, W. Cadwell, J. Dorsey, J. Fairey, and R. Varga, "Pdq–an IBM-704 code to solve the two-dimensional few-group neutron-diffusion equations", Westinghouse Electric Corp. Bettis Plant, Pittsburgh, Tech. Rep., 1957.

[13] D. Ferguson and K. Derstine, "Optimized iteration strategies and data management considerations for fast reactor finite difference diffusion theory codes", *Nuclear Science and Engineering*, vol. 64, no. 2, pp. 593–604, 1977.

[14] R. Lawrence, "Progress in nodal methods for the solution of the neutron diffusion and transport equations", *Progress in Nuclear Energy*, vol. 17, no. 3, pp. 271–301, 1986.

[15] C. Kang and K. Hansen, "Finite element methods for reactor analysis", *Nuclear science and Engineering*, vol. 51, no. 4, pp. 456–495, 1973.

[16] A. Kavenoky and J. Lautard, "The neutron kinetics and thermal-hydraulic transient computational module of the neptune system: CRONOS ", 1982.

[17] O. Zienkiewicz, R. Taylor, and J. Zhu, *The finite element method: its basis and fundamentals.* Butterworth-Heinemann, 2005.

[18] M. L. Adams and W. R. Martin, "Diffusion synthetic acceleration of discontinuous finite element transport iterations", *Nuclear science and engineering*, vol. 111, no. 2, pp. 145–167, 1992.

[19] T. A. Wareing, J. M. McGhee, J. E. Morel, and S. D. Pautz, "Discontinuous finite element SN methods on three-dimensional unstructured grids", *Nuclear science and engineering*, vol. 138, no. 3, pp. 256–268, 2001.

[20] L. Demkowicz, J. T. Oden, W. Rachowicz, and O. Hardy, "Toward a universal hp adaptive finite element strategy, part 1. constrained approximation and data structure", *Computer Methods in Applied Mechanics and Engineering*, vol. 77, no. 1, pp. 79–112, 1989.

[21] J. T. Oden, L. Demkowicz, W. Rachowicz, and T. Westermann, “Toward a universal hp adaptive finite element strategy, part 2. a posteriori error estimation”, *Computer Methods in Applied Mechanics and Engineering*, vol. 77, no. 1, pp. 113–180, 1989.

[22] W. Rachowicz, J. Oden, and L. Demkowicz, “Toward a universal hp adaptive finite element strategy part 3. design of hp meshes”, *Computer Methods in Applied Mechanics and Engineering*, vol. 77, no. 1, pp. 181–212, 1989.

[23] H. Zhang and E. Lewis, “Spatial adaptivity applied to the variational nodal PN equations”, *Nuclear science and engineering*, vol. 142, no. 1, pp. 57–63, 2002.

[24] J. Warsa and A. Prinja, “P-adaptive numerical methods for particle transport”, *Transport theory and statistical physics*, vol. 28, no. 3, pp. 229–270, 1999.

[25] W. Stacey, “Space – time neutron kinetics”, *Nuclear Reactor Physics, Second Edition*, pp. 599–667,

[26] S. González-Pintor, “Approximation of the neutron diffusion equation on hexagonal geometries”, PhD thesis, Universitat Politécnica de Valéncia, 2012.

[27] J. Taylor and A. Baratta, “A time-dependent method of characteristics for 3D nuclear reactor kinetics applications”, 2009.

[28] A. Pautz and A. Birkhofer, “Dort-td: a transient neutron transport code with fully implicit time integration”, *Nuclear science and engineering*, vol. 145, no. 3, pp. 299–319, 2003.

[29] S. Goluoglu and H. Dodds, “A time-dependent, three-dimensional neutron transport methodology”, *Nuclear science and engineering*, vol. 139, no. 3, pp. 248–261, 2001.

[30] M. Capilla, C. Talavera, D. Ginestar, and G. Verdú, “Application of a nodal collocation approximation for the multidimensional PL equations to the 3D takeda benchmark problems”, *Annals of Nuclear Energy*, vol. 40, no. 1, pp. 1 –13, 2012.

[31] M Capilla, C. Talavera, D Ginestar, and G Verdú, “A nodal collocation approximation for the multi-dimensional PL equations– 2D applications”, *Annals of Nuclear Energy*, vol. 35, no. 10, pp. 1820–1830, 2008.

[32] P. S. Brantley and E. W. Larsen, “The simplified P3 approximation”, *Nuclear science and engineering*, vol. 134, no. 1, pp. 1–21, 2000.

[33] B. Davison, *Neutron transport theory*, ser. International series of monographs on physics. Clarendon Press, 1958.

[34] E. Gelbard, “Application of spherical harmonics method to reactor problems”, *Bettis Atomic Power Laboratory, WAPD-BT-20*, 1960.

[35] E. M. Gelbard, *Simplified spherical harmonics equations and their use in shielding problems.* 1961.

[36] E. M. Gelbard, B. A. P. Laboratory, and U. A. E. Commission, *Applications of the simplified spherical harmonics equations in spherical geometry.* 1962.

[37] E. E. Lewis and W. F. Miller, “Computational methods of neutron transport”, John Wiley and Sons, Inc., New York, NY, 1984.

[38] E. M. Gelbard, “Spherical harmonics methods: PL and double PLapproximations”, *Computing methods in reactor physics*, p. 271, 1968.

[39] W. Stacey, *Nuclear Reactor Physics.* Wiley, New York., 2001.

[40] A. Henry, *Nuclear-reactor analysis.* Cambridge, MA, USA: MIT Press, 1975.

[41] V. Hernandez, J. Roman, V. Vidal, G. Verdú, and D. Ginestar, “Resolution of the neutron diffusion equation with SLEPc, the scalable library for eigenvalue problem computations”, *Nuclear Mathematical and Computational Sciences: A Century in Review, A Century Anew, Gatlinburg, TN, ANS*, 2003.

[42] G. Verdú, J. Muñoz-Cobo, C. Pereira, and D. Ginestar, “Lambda modes of the neutron-diffusion equation: application to BWR’s out-of-phase instabilities”, *Annals of Nuclear Energy*, vol. 20, no. 7, pp. 477–501, 1993.

[43] R. Miró, D. Ginestar, G. Verdú, and D. Hennig, “A nodal modal method for the neutron diffusion equation. application to BWR instabilities analysis”, *Annals of Nuclear Energy*, vol. 29, no. 10, pp. 1171–1194, 2002.

[44] Y. G. Dragunov, S. Ryzhov, V. Denisov, and V. Mokhov, “Prospects for development of VVER-type pressurized light-water reactor installations”, *Thermal engineering*, vol. 54, no. 5, pp. 343–347, 2007.

[45] I. Vasil'chenko, S. Kobelev, V. V'yalitsyn, and D. Mal'chevskii, "Succession in choosing structural solutions for a VVER-1500 core", *Atomic Energy*, vol. 99, no. 6, pp. 844–848, 2005.

[46] W. Bangerth, R. Hartmann, and G. Kanschat, "deal.II – a general purpose object oriented finite element library", *ACM Trans. Math. Softw.*, vol. 33, no. 4, pp. 24/1–24/27, 2007.

[47] R. Becker and R. Rannacher, "Weighted a posteriori error control in fe methods", *IWR*, 1982.

[48] G. Kanschat, "Parallel and adaptive galerkin methods for radiative transfer problems", PhD thesis, Heidelberg University, 1996.

[49] F. Suttmeier, "Adaptive finite element approximation of problems in elasto-plasticity theory", PhD thesis, Heidelberg University, 1996.

[50] B. Stroustrup, *The C++ Programming Language.* Addison-Wesley, 1997.

[51] A. Stepanov and M. Lee, *The standard template library.* Hewlett Packard Laboratories 1501 Page Mill Road, Palo Alto, CA 94304, 1995, vol. 1501.

[52] P. Plauger, A. Stepanov, M. Lee, and D. Musser, *The C++ Standard Template Library.* Prentice Hall, 2001.

[53] M. Heroux, R. Bartlett, V. Howle, R. Hoekstra, J. Hu, T. Kolda, R. Lehoucq, K. Long, R. Pawlowski, E. Phipps, A. Salinger, H. Thornquist, R. Tuminaro, J. Willenbring, and A. Williams, "An overview of the trilinos project", *ACM Transactions on Mathematical Software (TOMS)*, vol. 31, no. 3, pp. 397–423, 2005.

[54] V. Hernandez, J. E. Roman, and V. Vidal, "SLEPc: a scalable and flexible toolkit for the solution of eigenvalue problems", *ACM Trans. Math. Software*, vol. 31, no. 3, pp. 351–362, 2005.

[55] G. Karypis and V. Kumar, "A software package for partitioning unstructured graphs, partitioning meshes, and computing fill-reducing orderings of sparse matrices", *University of Minnesota, Department of Computer Science and Engineering, Army HPC Research Center, Minneapolis, MN*, 1998.

[56] G Karypis and V Kumar, "Metis–serial graph partitioning and fill-reducing matrix ordering. university of minnesota", 1998.

[57] *University College Dublin :UCD Library.* [Online]. Available: `http://www.ucd.ie/library/`.

[58] M. Sato, K. Kusano, H. Nakada, S. Sekiguchi, and S. Matsuoka, “Netcfd: a ninf cfd component for global computing, and its java applet gui”, in *High Performance Computing in the Asia-Pacific Region, 2000. Proceedings. The Fourth International Conference/Exhibition on*, IEEE, vol. 1, 2000, pp. 501–506.

[59] T. A. Davis, “Algorithm 832: umfpack v4. 3—an unsymmetric-pattern multifrontal method”, *ACM Transactions on Mathematical Software (TOMS)*, vol. 30, no. 2, pp. 196–199, 2004.

[60] M. Hopper, *Harwell Subroutine Library: A Catalogue of Subroutines (1981).* AERE, Computer Science and Systems Division, 1981.

[61] E. Anderson, Z. Bai, C. Bischof, L. S. Blackford, J. Demmel, J. J. Dongarra, J. Du Croz, S. Hammarling, A. Greenbaum, A. McKenney, and D. Sorensen, *LAPACK Users' Guide (Third Ed.)* Philadelphia, PA, USA: Society for Industrial and Applied Mathematics, 1999.

[62] R. B. Lehoucq, D. C. Sorensen, and C. Yang, *ARPACK users' guide: solution of large-scale eigenvalue problems with implicitly restarted Arnoldi methods.* Siam, 1998, vol. 6.

[63] S. Balay, W. Gropp, L. C. McInnes, and B. F. Smith, “Efficient management of parallelism in object oriented numerical software libraries”, in *Modern Software Tools in Scientific Computing*, E. Arge, A. M. Bruaset, and H. P. Langtangen, Eds., Birkhäuser Press, 1997, pp. 163–202.

[64] W. Schroeder, L. Avila, and W. Hoffman, “Visualizing with vtk: a tutorial”, *Computer Graphics and Applications, IEEE*, vol. 20, no. 5, pp. 20–27, 2000.

[65] W. Bellevue, *Tecplot user's manual*, 2005. [Online]. Available: `http://www.tecplot.com/`.

[66] J.Racine, “Gnuplot 4.0: a portable interactive plotting utility”, *Journal of Applied Econometrics*, vol. 21, no. 1, pp. 133–141, 2006.

[67] J. Abraham and V. Magi, “GMV, general mesh viewer”, *Los Alamos National Laboratory LA-UR-95-2986, Los Alamos*, 1995.

[68] C. Geuzaine and J. Remacle, “Gmsh: a 3-D finite element mesh generator with built-in pre- and post-processing facilities”, *International Journal for Numerical Methods in Engineering*, vol. 79, no. 11, pp. 1309–1331, 2009.

[69] M. Damyanova, S. Sabchevski, and I. Zhelyazkov, “Pre-and post-processing of data for simulation of gyrotrons by the gyreoss software package”, in *Journal of Physics: Conference Series*, IOP Publishing, vol. 207, 2010, p. 012 032.

[70] R. Miró, D. Ginestar, G. Verdú, and D. Hennig, “A nodal modal method for the neutron diffusion equation. application to BWR instabilities analysis”, *Annals of Nuclear Energy*, vol. 29, no. 10, pp. 1171–194, 2002.

[71] J. March-Leuba and J. Rey, “Coupled thermohydraulic-neutronic instabilities in boiling water nuclear reactors: a review of the state of the art”, *Nuclear Engineering and Design*, vol. 145, no. 1-2, pp. 97–111, 1993.

[72] D. Ginestar, R. Miró, G. Verdú, and T. Barrachina, “Modal processing of the local power range monitors signals in BWR NPP”, *Annals of Nuclear Energy*, vol. 38, no. 11, pp. 2441 –2455, 2011.

[73] K. Singh and V. Kumar, “Solution of the multigroup diffusion equation in hex-z geometry by finite fourier transformation”, *Annals of Nuclear Energy*, vol. 20, no. 3, pp. 153–161, 1993.

[74] Y. A. Chao and Y. A. Shatilla, “Conformal mapping and hexagonal nodal methods. 2: Implementation in the ANC-H code”, *Nuclear Science and Engineering*, vol. 121, pp. 210–225, 1995.

[75] J. Y. Cho and C. H. Kim, “Higher order polynomial expansion nodal method for hexagonal core neutronics analysis”, *Annals of Nuclear Energy*, vol. 25, no. 13, pp. 1021–1031, 1998.

[76] A. Hébert, “A Raviart-Thomas-Schneider solution of the diffusion equation in hexagonal geometry”, *Annals of Nuclear Energy*, vol. 35, no. 3, pp. 363 –376, 2008.

[77] K. Derstine, “DIF3D: a code to solve one-, two-, and three-dimensional finite-difference diffusion theory problems.[LMFBR]”, Argonne National Lab., IL (USA), Tech. Rep., 1984.

[78] A. Hebert, “A Raviart–Thomas–Schneider solution of the diffusion equation in hexagonal geometry”, *Annals of Nuclear Energy*, vol. 35, no. 3, pp. 363–376, 2008.

[79] C. Baker, A. Buchan, C. Pain, B. Tollit, M. Goffin, S. Merton, and P. Warner, “Goal based mesh adaptivity for fixed source radiation transport calculations”, *Annals of Nuclear Energy*, vol. 55, no. 0, pp. 169 –183, 2013.

[80] G. Theler, “A consistent multidimensional nodal method for transient calculations”, *Science and Technology of Nuclear Installations*, vol. 2013, no. 641863, 2013.

[81] Y. Wang and J. Ragusa, “Application of hp adaptivity to the multigroup diffusion equations”, *Nuclear Science and Engineering*, vol. 161, no. 1, pp. 22–48, 2009.

[82] P. G. Ciarlet, *The finite element method for elliptic problems*. Elsevier, 1978.

[83] D. Gilbarg and N. S. Trudinger, *Elliptic partial differential equations of second order*. Springer Science & Business Media, 2001, vol. 224.

[84] A. Vidal-Ferrandiz, R. Fayez, D. Ginestar, and G. Verdú, “Solution of the lambda modes problem of a nuclear power reactor using an h-p finite element method”, *Annals of Nuclear Energy*, vol. 72, no. 0, pp. 338 –349, 2014.

[85] G. Stewart, “A Krylov-Schur algorithm for large eigenproblems”, *SIAM Journal on Matrix Analysis and Applications*, vol. 23, no. 3, pp. 601–614, 2002.

[86] R. B. Morgan, “GMRES with deflated restarting”, *SIAM J. Sci. Comput.*, vol. 24, no. 1, pp. 20–37, Jan. 2002.

[87] E. Cuthill and J. McKee, “Reducing the bandwidth of sparse symmetric matrices”, in *Proceedings of the 1969 24th national conference*, ser. ACM ’69, New York, NY, USA: ACM, 1969, pp. 157–172.

[88] D. Gago, D. W. Kelly, O. C. Zienkiewicz, and I. Babuska, “A posteriori error analysis and adaptive processes in the finite element method: part II – adaptive mesh refinement”, *International Journal for Numerical Methods in Engineering*, vol. 19, no. 11, pp. 1621–1656, 1983.

[89] W. Bangerth and O. Kayser-Herold, “Data structures and requirements for hp finite element software”, *ACM Trans. Math. Softw.*, vol. 36, no. 1, pp. 4/1–4/31, 2009.

[90] J. Lamarsh, *Introduction to Nuclear Reactor Theory.* American Nuclear Society, 2002.

[91] S González-Pintor, D. Ginestar, and G Verdú, “Continuous pseudospectral methods for the neutron diffusion equation in 1d geometries”, *Mathematical and Computer Modelling*, vol. 50, no. 5, pp. 783–793, 2009.

[92] D. Barber, H. Joo, and T. Downar, *PARCS: A Multi-dimensional Two-group Reactor Kinetics Code Based on the Nonlinear Analytic Nodal Method*, ser. PU NE: School of Nuclear Engineering. Purdue University, School of Nuclear Engineering, 1998.

[93] N. P. Kolev, C. Fedon-Magnaud, and R. Lenain, *Solutions of Seidel’s 3D Benchmark for VVER-440 by CRONOS*, Proc. 7-th Symp. of AER on VVER Reactor Physics and Safety, Hoernitz, Germany, September 1997.

[94] W. M. Stacey, *Nuclear reactor physics.* John Wiley & Sons, 2007.

[95] G. Verdú, D. Ginestar, V. Vidal, and J. Muñoz-Cobo, “A consistent multidimensional nodal method for transient calculations”, *Annals of Nuclear Energy*, vol. 22, no. 6, pp. 395 –410, 1995.

[96] D. Ginestar, G. Verdú, V. Vidal, R. Bru, J. Marín, and J. Muñoz-Cobo, “High order backward discretization of the neutron diffusion equation”, *Annals of Nuclear Energy*, vol. 25, pp. 47 –64, 1998.

[97] R. Bru, D. Ginestar, J. Marín, G. Verdú, J. Mas, and T. Manteuffel, “Iterative schemes for the neutron diffusion equation”, *Computers & Mathematics with Applications*, vol. 44, no. 10, pp. 1307–1323, 2002.

[98] L. Giraud, S. Gratton, and E Martin, “Incremental spectral preconditioners for sequences of linear systems”, *Applied Numerical Mathematics*, vol. 57, no. 11, pp. 1164–1180, 2007.

[99] S González-Pintor, D. Ginestar, and G Verdú, “Preconditioning the solution of the time-dependent neutron diffusion equation by recycling krylov subspaces”, *International Journal of Computer Mathematics*, vol. 91, no. 1, pp. 42–52, 2014.

[100] S. Dulla, E. H. Mund, and P. Ravetto, “The quasi-static method revisited”, *Progress in Nuclear Energy*, vol. 50, no. 8, pp. 908 –920,

[101] K. Kobayashi, “A rigorous weight function for neutron kinetics equations of the quasi-static method for subcritical systems”, *Annals of Nuclear Energy*, vol. 32, no. 8, pp. 763–776, 2005.

[102] H. S. Joo, “Resolution of the control rod cusping problem for nodal methods”, PhD thesis, Massachusetts Institute of Technology, 1984.

[103] Y. Kim and N. Cho, “A bilinear weighting method for the control rod cusping problem in nodal methods”, *J. Korean Nucl. Soc*, vol. 22, no. 3, pp. 238–1990, 1990.

[104] M. W. F. Bennewitz H. Finnemann, “Higher-order corrections in nodal reactor computations”, *Trans. Am. Nucl. Soc.*, vol. 22, p. 205, 1975.

[105] S. González-Pintor, G. Verdú, and D. Ginestar, “Correction of the rod cusping effect for a high order finite element method”, in *Proceedings of the International Conference on Mathematics and Computational Methods Applied to Nuclear Science and Engineering (M&C 2011). Rio de Janeiro, RJ, Brazil, May 8-12, 2011, on CD-ROM, Latin American Section (LAS) / American Nuclear Society (ANS)*, 2011.

[106] A. Dall’Osso, “Reducing rod cusping effect in nodal expansion method calculations”, in *Proceedings of the International Conference on the New Frontiers of Nuclear Technology: Reactor Physics, Safety and High-Performance Computing (PHYSOR), Seoul, Korea*, 2002.

[107] A. Yamamoto, “A simple and efficient control rod cusping model for three-dimensional pin-by-pin core calculations”, *Nuclear Technology*, vol. 145, pp. 11–17, 2004.

[108] J. C. Gehin, “A quasi-static polynomial nodal method for nuclear reactor analysis”, Oak Ridge Inst. for Science and Education, TN (United States); Massachusetts Inst. of Tech., Cambridge, MA (United States), Tech. Rep., 1992.

[109] K. Smith, K. Rempe, J. Rhodes III, and J. Stevens, “Enhancements of the studsvik core management system (cms)”, 1992.

[110] N. Cho, D. Kim, and K. Lee, “Three-dimensional reactor kinetics calculation in analytic function expansion nodal method”, 2001.

[111] D. Gilbert, J. Roman, W. J. Garland, and W. Poehlman, “Simulating control rod and fuel assembly motion using moving meshes”, *Annals of Nuclear Energy*, vol. 35, no. 2, pp. 291 –303, 2008.

[112] A. Vidal-Ferrandiz, R. Fayez, D. Ginestar, and G. Verdú, “Moving meshes to solve the time-dependent neutron diffusion equation in hexagonal geometry”, *Journal of Computational and Applied Mathematics*, vol. 291, pp. 197 –208, 2016.

[113] P. Šolín, J. Červený, and I. Doležel, “Arbitrary-level hanging nodes and automatic adaptivity in the hp-FEM”, *Mathematics and Computers in Simulation*, vol. 77, no. 1, pp. 117 –132, 2008.

[114] Y. Saad, *Iterative Methods for Sparse Linear Systems*, 2nd. Philadelphia, PA, USA: Society for Industrial and Applied Mathematics, 2003.

[115] G. E. Karniadakis and S. J. Sherwin, *Spectral/hp element methods for computational fluid dynamics*, ser. Numerical mathematics and scientific computation. Oxford, New York, Aukland: Oxford University Press, 2005.

[116] S. González-Pintor and D. Ginestar, “Reducing rod cusping effect in nodal expansion method calculations”, *Joint International Conference Mathematics and Computation*, 2011.

[117] A Keresztúri, M Telbisz, I Vidovszky, U Grundmann, and J Krell, “Results of a three-dimensional hexagonal kinetic benchmark problem”, in *ENs Meeting, Portoroz*, 1993.

[118] E. E. Lewis and J. W. F. Miller, *Computational Methods of Neutron Transport.* John Wiley and Sons, Inc., New York, NY, 1993.

[119] M. Capilla, C. Talavera, D. Ginestar, and G. Verdú, “A nodal collocation method for the calculation of the Lambda Modes of the pl equations”, *Annals of Nuclear Energy*, vol. 32, no. 17, pp. 1825 –1853, 2005.

[120] A. D. Klose and E. W. Larsen, “Light transport in biological tissue based on the simplified spherical harmonics equations”, *Journal of Computational Physics*, vol. 220, no. 1, pp. 441–470, 2006.

[121] E. W. Larsen, J. Morel, and J. M. McGhee, “Asymptotic derivation of the multigroup P1 and simplified PN equations with anisotropic scattering”, *Nuclear science and engineering*, vol. 123, no. 3, pp. 328–342, 1996.

[122] D. I. Tomašević and E. W. Larsen, “The simplified p 2 approximation”, *Nuclear science and engineering*, vol. 122, no. 3, pp. 309–325, 1996.

[123] *DANTSYS: A Diffusion Accelerated Neutral Particle Transport Code System.* Los Alamos National Laboratory, 1995. [Online]. Available: `https://books.google.es/books?id=Kf2zoAEACAAJ`.

[124] D. E. Kornreich and D. K. Parsons, “The green’s function method for effective multiplication benchmark calculations in multi-region slab geometry”, *Annals of Nuclear Energy*, vol. 31, no. 13, pp. 1477–1494, 2004.